2024

# Tuning capillary evaporation in nanoporous membranes: fundamentals and applications

BOSTON UNIVERSITY

COLLEGE OF ENGINEERING

Dissertation

# TUNING CAPILLARY EVAPORATION IN NANOPOROUS MEMBRANES: FUNDAMENTALS AND APPLICATIONS

by

**CHU-YAO CHOU**

BS, National Chiao Tung University, 2012
MS, National Chiao Tung University, 2017

Submitted in partial fulfillment of the

requirements for the degree of

Doctor of Philosophy

2024

Approved by

First Reader

Chuanhua Duan, Ph.D.
Associate Professor of Mechanical Engineering
Associate Professor of Materials Science and Engineering

Second Reader

J. Scott Bunch, Ph.D.
Associate Professor of Mechanical Engineering
Associate Professor of Materials Science and Engineering

Third Reader

Kamil Ekinci, Ph.D.
Professor of Mechanical Engineering
Professor of Materials Science and Engineering

Fourth Reader

Xin Zhang, Ph.D.
Professor of Mechanical Engineering
Professor of Electrical and Computer Engineering
Professor of Biomedical Engineering
Professor of Materials Science and Engineering

**ACKNOWLEDGMENTS**

Most importantly, I would like to thank my advisor Prof. Chuanhua Duan for guiding me through my PhD journey at Boston University. His invaluable advises and decisions are on-point and benefit my career development as an engineer. He was supportive and patient with me when I encounter difficulties. Those decision making process would carry out through my life and I will never forget. I am fortunate to have Prof. Duan as my advisor. I would also like to thank my thesis committee members: Prof. Kamil Ekinci, Prof. Xin Zhang, and Prof. Scott Bunch for supporting me and constantly improving the quality of my work.

I would like to thank my wife, Kristin Yijie Chen, for supporting me through this tough journey. Thank you for being there whenever I needed you. I remember those days when the stress level was so high and you will calm me down by making something warm and delicious to eat. Also, when things get hard and nothing goes the way it was supposed to, you would encourage me to try more before giving up and switching direction. During the research process, thank you for listening to me patiently when I was explaining academic jargon to you. Usually, this would let me come up with some good ideas to debug the experiment and I enjoyed those "AH HA" moments. Last but not least, thank you for sharing your experience and guide me through the job hunting process. I alone cannot withhold the anxiety and desperate feeling of constantly getting rejected/ghosted after 1000+ applications.

Next, I would like to thank Yanpu He and Celestine Hong for treating me like family. I had so many questions regarding how to make research decisions and design experiments. Also, thank you for hosting some of the greatest lobster/bear/hot pot/exotic cuisine nights and during the gatherings we would laugh

about interesting things going on in our lives. Every time, I feel refreshed, recharged, and relaxed and am ready to take on any challenge for the next few months. Those are the shiniest memories during my PhD.

I would also like to thank my family in Philly and back in Taiwan for helping me make critical decisions during the hardest time in my PhD career. Thank you for your support and all the wisdom you gave me to help me navigate through the complex relationship in the lab and help me move on with some intolerable situations. Thank you for reminding me what are the essential things in my life, stop wasting my time on the people who do not deserve it and make peace with myself.

**TUNING CAPILLARY EVAPORATION IN NANOPOROUS MEMBRANES: FUNDAMENTALS AND APPLICATIONS**

**CHU-YAO CHOU**

Boston University, College of Engineering, 2024

Major Professor: Chuanhua Duan, PhD

Associate Professor of Mechanical Engineering

Associate Professor of Materials Science and Engineering

ABSTRACT

Capillary evaporation from nanoporous membranes is defined as an evaporation process where liquid water is drawn passively by capillary force from the membrane inlet to the evaporating meniscus. It has been considered as one of the most effective methods for phase-change heat and mass transfer as both the heat and mass transport resistance are minimized, finding promising applications in electronic cooling, solar-powered desalination, and membrane-based water treatment. This thesis aims to explore novel methods to tune capillary evaporation from nanoporous membranes and new applications that can utilize such effective phase-change heat/mass transfer. First of all, the effect of nanopore surface charge on evaporation area and evaporation flux per pore area is investigated numerically. Our results show that the evaporation flux increases as the nanopore surface charge density increases, being 81.1% higher when the surface charge density reaches -80 mC/m2. Secondly, hybrid nanochannel-nanopore devices with varied hydraulic resistance are fabricated to tune capillary evaporation by changing

the meniscus area during evaporation. We find that the mass flux is actually the highest when the meniscus is flat and attribute it to the change of hydrogen bond network due to meniscus extension-induced negative pressure and/or interfacial surface charge density. Next, a parylene C membrane and a laser-reduced graphite oxide membrane are tested for capillary evaporation based surface heating membrane distillation. For the parylene C membrane, a 1D analysis is conducted to model the vapor transport and temperature distribution within the system. The optimized mass flux and HUE is 152.63% and 28% higher than the state-of-the-art device, respectively. On the other hand, the laser-reduced graphite oxide membrane serves as an attempt for large scale manufacturing. Finally, a suspended thermal island design is proposed to address the challenges that the current hybrid nanochannel-nanopore device encountered.

## CONTENTS

## LIST OF TABLES

## LIST OF FIGURES

## LIST OF SYMBOLS AND ABBREVIATIONS

| | |
|---|---|
| $a$ . | Van der Waals constant |
| $A$ | Heater area |
| $A_c$ | Cross-sectional area |
| $b$ . | Van der Waals constant |
| $\sigma$ . | Surface tension of water |
| $\rho$ . | Density of water |
| $g$ . | Gravitational acceleration |
| $\mu$ . | Viscosity of water |
| $k$ . | Thermal conductivity |
| $\Delta T$ | Temperature difference |
| $L$ | Latent heat of vaporization |
| $T$ | Temperature |
| $C_p$ | Specific heat capacity of water |
| $\dot{m}$ | Mass flow rate |
| $h$ . | Local heat transfer coefficient |
| $P$ | Pressure |
| $q^{''}$ | Heat flux |
| $\phi$ . | Solid-liquid fraction |
| $\theta$ . | Contact angle |
| $v$ . | Specific volume |
| $\infty$ | Far ambient conditions |

# CHAPTER 1

## Introduction

Capillary evaporation is defined as an evaporation process where liquid water is drawn passively by capillary force from the inlet to the evaporating meniscus. This is usually achieved by creating a low pressure regime at the meniscus area within the micro/nano pores since the liquid pressure ($P_l \propto -1/r$), where $r$ is the pore radius. Because the meniscus inside the micro/nanopore and the resulting liquid thin film guarantees low thermal resistance between the solid substrate and the liquid/vapor interface, capillary evaporation has been considered as a very efficient phase-change based heat/mass transfer strategy and holds great potential in various applications related to liquid-vapor phase change, including electronic cooling, solar steam generation, and membrane based water treatment technologies.

Over the past decade, numerous efforts have been made to enhance capillary evaporation in micro/nanoporous structures and improve/expand its applications.

On one hand, researchers have tried to enhance capillary evaporation by identifying and overcoming the transport limiting processes. It is widely accepted that in such systems, there are three mass transport resistances in series, the liquid transport resistance from the inlet through the conduit to the meniscus, the interfacial resistance for water molecules transforming into vapor molecules, and the vapor transport resistance leaving the meniscus as shown in fig.1.1.

Early research efforts tried to reduce the liquid transport resistance by reducing the pore size with a larger capillary pressure Dai et al. (2013); Adera et al. (2016); Wilke et al. (2016); Adera et al. (2013); Narayanan et al. (2013). However,

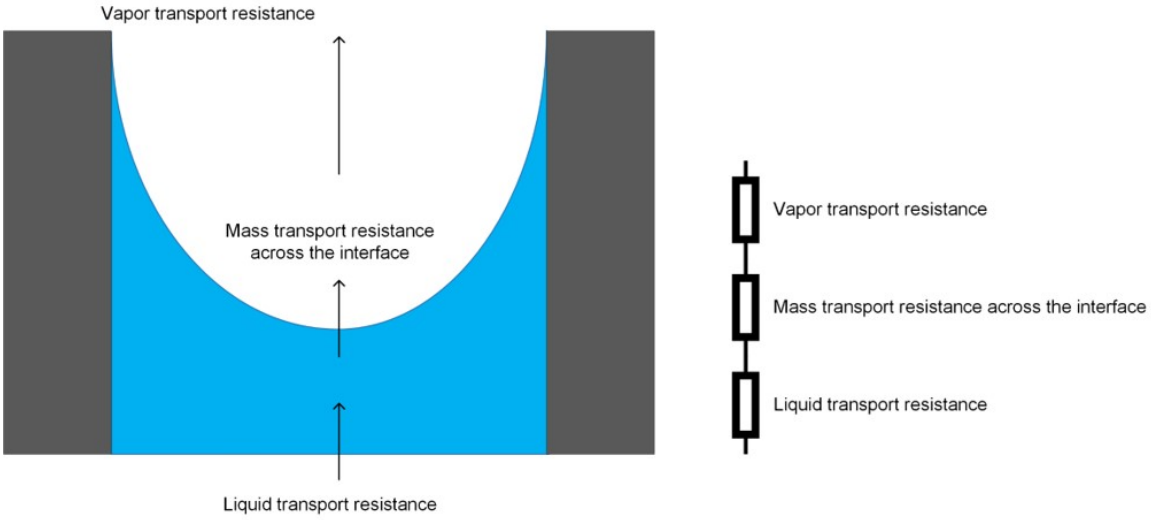


**Figure 1.1:** Transport resistances in the capillary evaporation system.

the viscous pressure loss associated with reducing the conduit size is coupled with the pore diameter and an optimized heat flux on the order of 200 $\mathbf{W/cm^2}$ was achieved. Having noticed this issue, recent researchers focused on methods to decouple the viscous pressure loss with the pore geometry. One of the most successful work demonstrated that by using a 200 nanometer thin SiN nanoporous membrane with microchannels for water supply, the heat flux could reach 500 $\mathbf{W/cm^2}$ in air ambient conditions Lu et al. (2017). A subsequent work from the same group further explored the effect of vapor transport on the heat flux for a device with an active evaporating area of 0.424 $\mathbf{cm^2}$ and realized a heat flux of 550 $\mathbf{W/cm^2}$ in pure vapor condition where the total pressure is less than normal pressure with pentane Hanks et al. (2020). As these studies demonstrated that both the liquid transport resistance and the vapor transport resistance can be tuned effectively such that they are no longer the dominant transport resistance, kinetically limited evaporation, which is the ultimate limit of capillary evaporation, can finally be achieved. Lu *et al.* studied the Kinetically-limited evaporation using ul-

trathin nanoporous membranes at various superheats and demonstrated a unified relationship for kinetically-limitd evaporation flux at low Mach numbers Lu et al. (2019). Meanwhile, Li *et al.* measured the kinetically-limited evaporation from single nanochannel and nanopore using hybrid nanochannel/nanopore devices and found the kinetically-limited evaporation flux shows a strong diameter dependence Li et al. (2019). Using DI water as the working fluid, they reported a heat flux up to 294 $\mathbf{W/cm^2}$ for a nanopore diameter of 30 **nm** at a temperature 20 **degC**. A brief summarize of the selected literature data is shown in fig.1.2. Although these recent works provide us new insights about kinetically-limited capillary evaporation, it still remains illusive how we can further improve the performance of evaporation given a nanopore diameter.

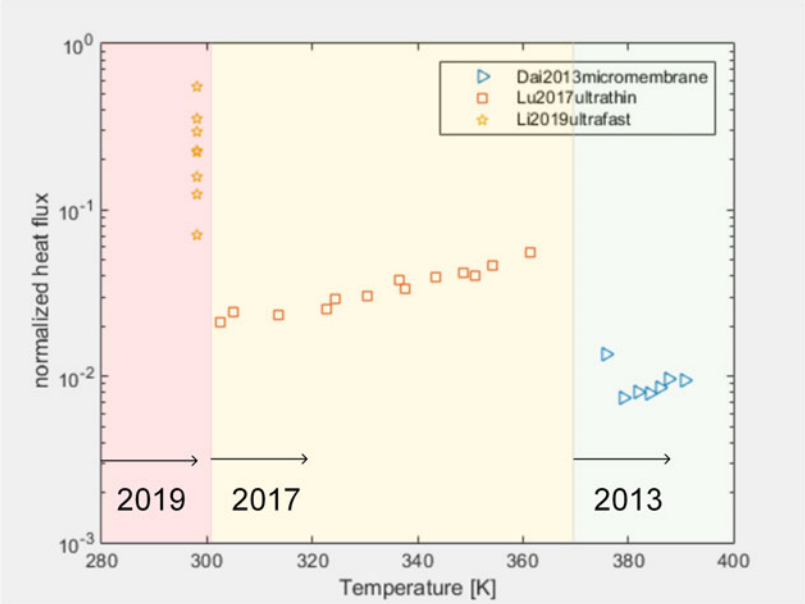


**Figure 1.2:** Selected literature data since 2013. The heat flux obtained from each literature is normalized by the Hertz-Knudsen equation under their working conditions to obtain the normalized heat flux.

On the other hand, a significant amount of work focused on expanding and/or improving the practical applications of capillary evaporation have been published

over the last decade. For example, Somasundaram*et al.* experimentally investigated the performance of capillary evaporation for electronic cooling applications Somasundaram et al. (2018) and optimized a heat flux of 100 $\mathbf{W/cm^2}$. The significant decrease of heat flux from 550 to 100 $\mathbf{W/cm^2}$ is because that the thermal resistance is much higher for actual devices. Capillary evaporation can also be applied to membrane based water treatment technologies such as forward osmosis and membrane desalination. Water treatment technology is a heated field of study as over 1.8 billion people are suffering from the water scarcity issue nowadays Dongare et al. (2017); Deshmukh et al. (2018). Forward osmosis is defined as a method to draw water from a diluted solution to a concentrated counterpart with a semipermeable membrane. When combined with reverse osmosis, it was demonstrated the energy required to produce fresh water had been lowered Wan & Chung (2018). Alternatively, membrane desalination is a method to thermally evaporate water from the high concentration side to the lower counterpart. This could be done either by solar or joule heating. A novel design utilized a hBN coated stainless steel wires (hBN-SSW) to heat the saline water locally and achieved a mass flux of 47.5 $\mathbf{kg/m^2h}$. This local heating strategy is termed as the surface heating membrane desalination. However, issues such as concentration polarization and reverse salt flux prevents further development of forward osmosis while the full potential of surface heating membrane desalination is not unlocked.

In this thesis, the author theoretically explored the effect of surface charge on capillary evaporation and a significant 81.1% increment is discovered by charging the wall to -80 $\mathbf{mC/m^2}$ while maintaining the same pore diameter. The corresponding heat flux is 43.47 $\mathbf{kW/cm^2}$, which is 43.47 folds higher than industrial

requirements. A hybrid nanochannel-nanopore device is designed and fabricated to test the effect of the shape of the meniscus. It is found that a flatter meniscus would lead to a higher evaporation coefficient. Finally, a system level modeling is used to determine the optimized design and length scale for the surface heating membrane desalination. The permeate water flux and heat utilization efficiency could be 152.63% and 28% higher than the hBN-SSW device in the literature, respectively.

# CHAPTER 2

# Numerical simulation of surface charge enhanced kinetically-limited evaporation in nanopores

## 2.1 INTRODUCTION

Evaporation, defined as the process of a material transforming from the liquid state to the vapor state, is a critical mechanism that governs the performance of evaporative cooling for electronic devices Adera et al. (2016); Bulut et al. (2019); Narayanan et al. (2013), steam generation for solar power plants Ghasemi et al. (2014); Tao et al. (2018); Xue et al. (2017), evaporation-based seawater desalination Chen et al. (2019); Aly & El-Figi (2003) and electrokinetic energy harvesting Yaroshchuk (2022). One way to enhance the performance of these systems is to exploit evaporation from nanoporous membranes because of its superior potential to dissipate heat and generate vapor efficiently. It has been reported that the evaporation heat fluxes, defined as the heat rate dissipated per unit area, can be as high as 600 $[\mathbf{W/cm^2}]$ Lu et al. (2017); Hanks et al. (2018). Furthermore, Li *et al.* experimentally demonstrated that the evaporation flux from nanopores depends critically on the pore diameter Li et al. (2019). To explain this interesting observation, they discussed possible mechanisms including change of evaporation area due to surface-liquid interactions as well as change of evaporation coefficient $\sigma_e$ (defined as the fraction of the vapor molecules crossing the liquid-vapor interface due to evaporation) due to the presence of surface charges on nanopore walls. However, no quantitative analysis was proposed to explain this phenomenon. The purpose of this study is to theoretically investigate the first mechanism, i.e., how surface charges affect the kinetically-limited evaporation through the extended meniscus

and the resulting evaporation area. This analysis could fundamentally unravel the complex interaction between solid, liquid and dissolved ions confined in the nanopore, and the result drawn from this study could further guide designs for novel phase-change devices.

It is well known that the length scale of the pore diameter plays the most important role in establishing the physical model to describe the heat and mass transfer process of evaporation from nanopores. Generally speaking, the capillary force attributed to the surface tension and the curvature of the meniscus dominates when the pore diameter is above 1 $\mu$m while the long-range van der Waals force prevails above 10 nm for non-polar liquids Gennes et al. (1985). A large volume of the literature has modeled evaporation from microchannels and cylindrical tubes based on the two forces Wayner Jr et al. (1976); Wayner Jr (1979); Buffone & Sefiane (2004); Buffone et al. (2004); Wang et al. (2008); Wee et al. (2005); DasGupta et al. (1993); Swanson & Herdt (1992). A novel study done by Narayanan *et al.* revealed that in addition to the above forces, electrostatic forces arose in polar liquids in fact increases the evaporation flux from nanopores dramatically Narayanan et al. (2011). The reason is that the electrostatic force acting on the interface tends to expand the area of the liquid meniscus. Therefore, as the area for evaporation increases, the evaporation mass flux normalized by the pore area increases. Inspired by this work, Pati *et al.* include the effect of slip velocity Pati et al. (2013) while Lu *et al.* extend Narayanan's work to study the nonequilibrium and nonlocal effects of evaporation from nanopores Lu et al. (2015). Later, Lu *et al.* compares the experimentally measured kinetically-limited evaporation mass flux with the result of DSMC, the H-K equation and the Schrage equation Lu et al. (2019). The results show that given a constant accommodation factor, the Schrage equation coincides

with the experimental results and the DSMC better than the the H-K equation. Therefore, the Schrage equation is used in the subsequent analysis to model the vapor transport to account for the nonequilibrium effect of intensive evaporation. However, these studies omitted the existence of a trace amount of protons and hydroxyl radicals in water as well as charged functional group on common surfaces. As a result, a modified electrostatic model to account for the complex solid-liquid-ion interaction is derived based on thermodynamic considerations in this study. This modified model is then incorporated with the systems of equations for fluid flow, heat transfer, and stress balance at the liquid-vapor interface in the continuum limit which are solved numerically to discover the effect of intermolecular forces between solid, liquid, and ions on the kinetically-limited evaporation.

## 2.2 THEORETICAL FORMULATION

The system of interest is shown in fig.2.1(a), where the top and bottom boundaries of the figure are the walls of the nanopore. Liquid water comes into the control volume from the left boundary and water vapor exits from the right boundary. The vapor is exposed to a vacuum chamber at 150 Pa with a mixture of air-vapor at a temperature $T_v$. At steady-state, the evaporating meniscus inside a pore is generally divided into three regimes: (1) the absorbed thin film regime where the liquid is in equilibrium with the gas and no evaporation happens; (2) the thin-film regime where the disjoining pressure dominates over the capillary pressure; (3) the meniscus regime where capillary pressure is prevailing. Beyond the meniscus regime, the liquid is modeled as fully-developed, laminar flow, which is described by the Hagen-Poiseuille equation.

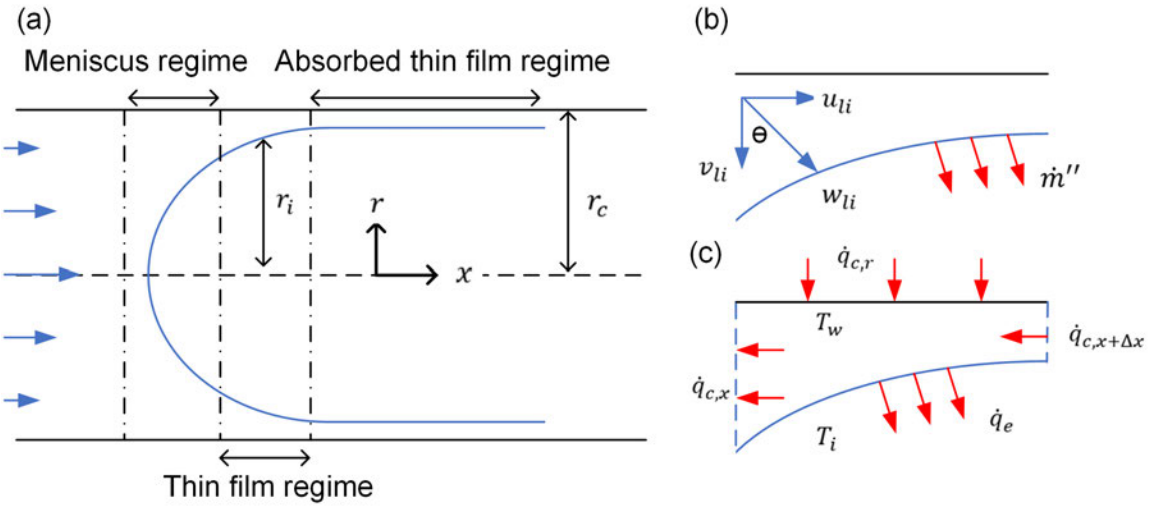


**Figure 2.1:** (a) Cartoon of the water meniscus confined in a nanopore. (b) Velocity component of fluid velocity. (c) Control volume analysis of heat transfer

### 2.2.1 Conservation of mass at the evaporating interface

The mass transfer to the interface can be found as follow:

Assuming a steady, axisymmetric, incompressible flow, and neglecting the radial pressure gradient compared to the dominating capillary pressure, the axial component of the momentum balance for the liquid flow is given by

$$-\frac{dP_{li}}{dx}+\frac{\mu_l}{r}\frac{\partial}{\partial r}(r\frac{\partial u_l}{\partial r})=0, \tag{2.1}$$

where $p_{li}$ is the liquid pressure, $\mu_l$ is the liquid viscosity and $u_l$ is the liquid velocity in the $x$-direction. The boundary conditions for fluid flow are the no-slip at the walls, $u=0$ at $r=r_c$, where $r_c$ is the pore radius and the thermocapillary stress balance at the interface, $-\mu_l(\partial u)/(\partial r)=(\partial\sigma)/(\partial x)$ at $r=r_i$, where $\sigma$ is the surface tension of water, $r_i$ is the radial location of the meniscus. This boundary condition means that, the shear stress along the tangential direction of the liquid-

vapor interface will be balanced by the tangential surface tension gradient due to possible temperature difference along the interface, which is the cause of thermal Marangoni flow and has been widely used in previous studies Swanson & Herdt (1992); Narayanan et al. (2011); Pati et al. (2013).

Using these boundary conditions, the solution of eq.2.1 is

$$u_l = (-\frac{1}{4\mu_l}\frac{dp_{li}}{dx})(r_c^2 - r^2 + 2r_i^2 \ln\frac{r}{r_c}) - \frac{r_i}{\mu_l}\frac{\partial\sigma}{\partial x}\ln\frac{r}{r_c}, \tag{2.2}$$

To relate the evaporating mass flux at the interface with the water supply, we start with the mass conservation equation $\partial u_l/\partial x + (1/r)\partial(rv_l)/\partial r = 0$ and integrate it between $r = r_i$ and $r = r_c$ to obtain the water supplied to the interface:

$$r_i v_{li} = \frac{d}{dx}\int_{r_i}^{r_c} r u_l dr + r_i u_{li}\frac{dr_i}{dx} \tag{2.3}$$

with the assumption that $v_l = 0$ at $r = r_c$, where $v_l$ is the liquid velocity in the $r$-direction and the subscript $i$ denotes the interfacial property. Since the mass flow rate $\dot{m} = \int \rho_l u_l (2\pi r) dr = 2\pi\rho_l \int u_l r dr$, where $\rho_l$ is the density of the liquid, substituting $\int u_l r dr$ in eq.2.3 in terms of $\dot{m}$ gives

$$v_{li} = \frac{1}{2\pi\rho_l r_i}\frac{d\dot{m}}{dx} + u_{li}\frac{dr_i}{dx}. \tag{2.4}$$

From fig.2.1(b), the velocity normal to the interface $w_{li}$ is given by

$$w_{li} = u_{li}\sin\theta - v_{li}\cos\theta, \tag{2.5}$$

where $\theta$ is the angle between the normal vector to the wall and the normal vector to the liquid-vapor interface as shown in fig.2.1(b). The supplying mass flux to the

interface is therefore $\dot{m}'' = \rho_l w_{li} = \rho_l(u_{li}\sin\theta - v_{li}\cos\theta)$. Replacing $v_{li}$ by eq.2.4, we get

$$\dot{m}'' = -\frac{1}{2\pi r_i}\frac{d\dot{m}}{dx}\cos\theta \tag{2.6}$$

as $dr_i/dx = \tan\theta$.

The mass flux leaving the interface at any point is described by the Schrage equation Schrage (1953):

$$\dot{m}'' = \frac{2\hat{\sigma}}{2-\hat{\sigma}}(\frac{M}{2\pi R})^{1/2}(\frac{p_{vi}}{T_{li}^{1/2}} - \frac{p_v}{T_v^{1/2}}) \tag{2.7}$$

where $\hat{\sigma}$ is the accommodation coefficient and is assumed to be 0.3 in this work Lu et al. (2019), $M = 0.018$ **[kg/mol]** is the molar weight of water molecules, $R = 8.314$ **[J/mol/K]** is the universal gas constant, $p_{vi}$ is the equilibrium vapor pressure at the interface at a temperature of $T_{li}$, and $p_v$ is the partial pressure of vapor in the gas phase at a temperature of $T_v$.

Equating $\dot{m}''$ with eq.2.7 and eq.2.6 and assuming the temperature discontinuity at the interface ($T_{li} = T_v$) is insignificant Swanson & Herdt (1992), we arrive at

$$-\frac{\cos\theta}{2\pi r_i}\frac{d\dot{m}}{dx} = \frac{2\hat{\sigma}}{2-\hat{\sigma}}(\frac{M}{2\pi R T_{li}})^{1/2}(p_{vi} - p_v), \tag{2.8}$$

where $\cos\theta = 1/\sqrt{1+(dr_i/dx)^2}$. Substituting $\dot{m} = \int \rho_l u_l (2\pi r) dr$ and eq.2.2 in eq.2.8 and integrating the resulting equation between $r = r_i$ and $r = r_c$, we finally got an equation for $\dot{m}$ as

$$\dot{m} = \frac{\pi\rho_l}{8\mu_l}(-\frac{-dp_{li}}{dx})[(r_c^2-r_i^2)(r_c^2-3r_i^2) - 4r_i^4\ln\frac{r_i}{r_c}] + \frac{\pi\rho_l}{8\mu_l}(\frac{d\sigma}{dT})(\frac{dT_{li}}{dx})[4r_i(r_c^2-r_i^2) + 8r_i^3\ln\frac{r_i}{r_c}] \tag{2.9}$$

Two unknowns ($p_{li}$ and $T_{li}$) are present in eq.2.9 and more equations are needed to solve them.

### 2.2.2 Solve for the interface temperature $T_{li}$

Omitting the advective heat transfer Pati et al. (2013); Narayanan et al. (2011), the energy conservation in the control volume shown in fig.2.1(c) is given by

$$q_{c,r} - q_{c,x} + q_{c,x+\delta x} = q_e, \tag{2.10}$$

where $q_e$ is the rate of heat transfer from evaporation:

$$q_e = -h_{fg}\frac{d\dot{m}}{dx}\Delta x \tag{2.11}$$

Heat conduction from the pore wall reads

$$q_{c,r} = -k_l(2\pi r_c \Delta x)(\frac{\partial T_l}{\partial r})_w \tag{2.12}$$

The total heat transfer in the $x$-direction reads

$$q_{c,x+\Delta x} - q_{c,x} \sim \Delta x(\frac{\partial q_{c,x}}{\partial x}), \tag{2.13}$$

where $\partial q_{c,x}/\partial x$ can be evaluated by the Leibniz integral rule as

$$\begin{aligned} \frac{\partial q_{c,x}}{\partial x} &= \frac{\partial}{\partial x}\int_{r_i}^{r_c} -k_l(2\pi r)\frac{\partial T_l}{\partial x}dr \\ &= (-2\pi k_l)\int_{r_i}^{r_c} r\frac{\partial^2 T_l}{\partial x^2}dr + (2\pi k_l r_i)(\frac{\partial T_l}{\partial x})_i\frac{dr_i}{dx} \end{aligned} \tag{2.14}$$

A linear temperature profile is assumed for the temperature variation in the radial direction Swanson & Herdt (1992):

$$\frac{T_l - T_w}{T_{li} - T_w} = \frac{r - r_c}{r_i - r_c}. \tag{2.15}$$

Substituting eq.2.11,2.12,2.13, and 2.14 back to eq.2.10 with eq.2.15, the governing equation for the temperature distribution is obtained:

$$\begin{gathered}\frac{\pi k_l}{3}(r_c + 2r_i)(r_c - r_i)(\frac{\partial^2 T_{li}}{\partial x^2}) + \frac{2\pi k_l}{3}(r_c - r_i)\frac{\partial r_i}{\partial x}\frac{\partial T_{li}}{\partial x} + \frac{2\pi k_l}{3}(T_{li} - T_w)(\frac{\partial r_i}{\partial x})^2 - \\ \frac{\pi k_l}{3}(r_c + 2r_i)(T_w - T_{li})\frac{\partial^2 r_i}{\partial x^2} + 2\pi k_l r_c \frac{t_w - T_{li}}{r_c - r_i} = -h_{fg}\frac{d\dot{m}}{dx}\end{gathered} \tag{2.16}$$

where the detailed derivation can be referred to Narayanan et al. (2011).

### 2.2.3 Solve for the liquid pressure $p_{li}$

To find the liquid pressure $p_{li}$, we look at the pressure balance at the interface:

$$p_{atm} - p_{li} = 2\sigma\kappa + \Pi_d, \tag{2.17}$$

where $p_{atm}$ is the ambient pressure, $p_{li}$ is the liquid pressure at the interface, $\kappa$ is the local mean curvature Philip (1977) and $\Pi_d$ is the disjoining pressure Derjaguin & Churaev (1974); Langmuir (1938).

$$\kappa = \frac{1}{2}(\frac{1}{r_i[1 + (dr_i/dx)^2]^{1/2}} + \frac{d^2 r_i/dx^2}{[1 + (dr_i/dx)^2]^{3/2}}) \tag{2.18}$$

$$\Pi_d = P_{vdw} + P_{ele}, \tag{2.19}$$

where $P_{vdw}$ is the pressure inside the liquid due to the van der Waals dispersion force between the liquid molecules and the solid wall and $P_{ele}$ is the pressure inside

the liquid attributed to the electrostatic force acting between the dissolved ions and the solid wall. Assuming a Lennard-Jones interaction potential between the solid and the liquid molecules, we find $P_{vdw} = -A/6\pi(r_c - r_i)^3$, where $A = -3.148e^{-20}[\mathbf{J}]$ is the modified Hamaker constant Carey (2020).

It is note worthy of the sign convention used here - a positive value of $P_{vdw}$ indicates the liquid molecules are attracted to the wall molecules. Therefore, a negative value of $A$ means that the wall material is hydrophilic in nature.

Two distinct solutions may be derived for $P_{ele}$ depending on the screening effect of the liquid film Israelachvili (2011). As the thickness of the film becomes thick enough, the thick water film screens the electrostatic force originating from the charged functional groups on the surface and $P_{ele}$ would be independent of the surface charge density. On the other hand, $P_{ele}$ would be dependent on the surface charge density as the water film is not thick enough to screen the electrostatic force. In the below paragraphs, we would discuss which solution is suitable for this study.

The system of interest is shown in fig.2.2, where the liquid solution is bounded by two surfaces - the solid-liquid interface and the liquid-vapor interface. To find $P_{ele}$ we start with the chemical potential of different types of ions $i$ in the solution Israelachvili (2011), $\mu_i = z_i e\psi + kT \log \rho_{xi}$, where $z_i$ is the charge number, $e$ is the charge of one electron, $\psi$ is the electrical potential, $k$ is the Boltzmann constant, $T$ is the absolute temperature, and $\rho_{xi}$ is the number density of ions at an arbitrary location $x$. This equation is valid for all types of ions in the solution. The solid-liquid interface and the liquid-vapor interface has a surface charge density of $\sigma_{sl}$ and $\sigma_{lv}$, respectively, and the corresponding electrical potential is $\psi_{sl}$ and $\psi_{lv}$, respectively. The liquid-vapor interface is considered to be negatively charged with

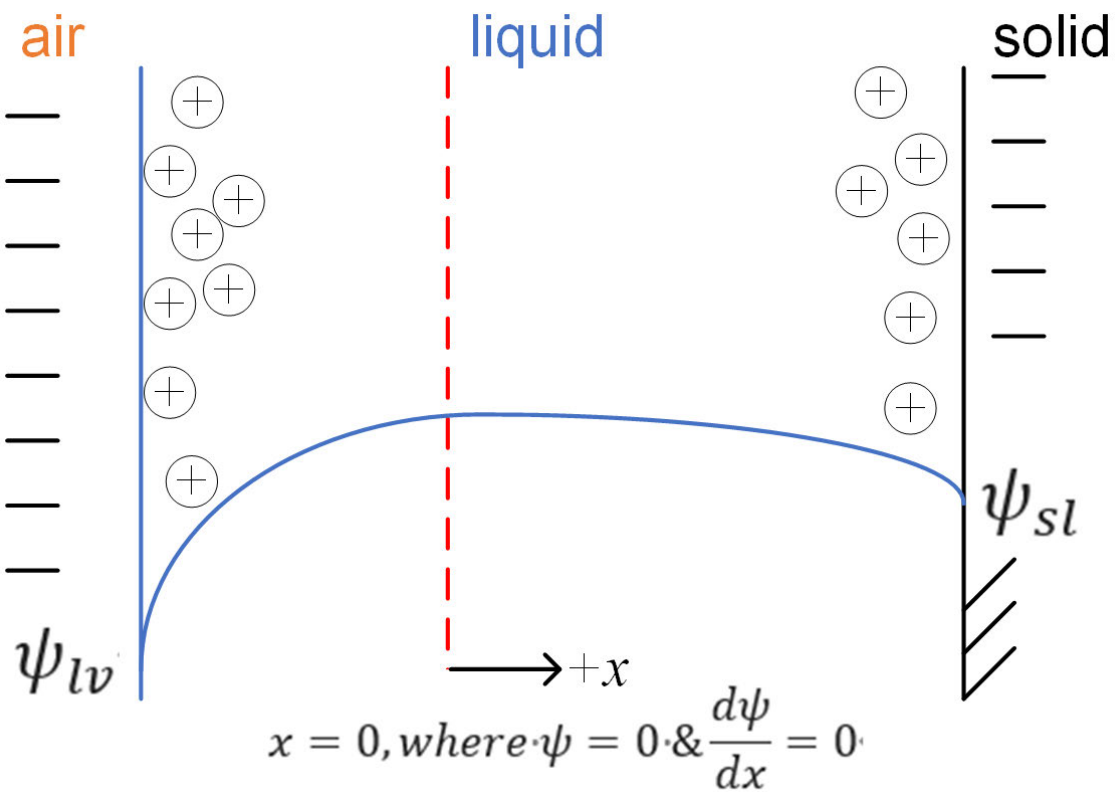


**Figure 2.2:** The system of interest to derive $P_{ele}$. The blue solid line represents the electrical potential distribution between the two surfaces (not to scale). Note that both surfaces are negatively charged.

$\sigma_{lv} = -2.4$ $[\mathbf{mC/m^2}]$ Poli et al. (2020). On the other hand, a typical solid surface is also considered to be negatively charged with $\sigma_{sv}$ ranging from 0 to -50 $[\mathbf{mC/m^2}]$ for silica, carboxyl, and sulfate surfaces Behrens & Grier (2001). Since both surfaces are considered to be negatively charged, there would be a point between the two surfaces where the electrical potential is the maximum, *i.e.* $d\psi/dx = 0$. We set the plane where $d\psi/dx = 0$ to $x = 0$ and also set $\psi = 0$ at this plane. Assuming the system is in equilibrium and the surface charge densities $\sigma_{sl}$ and $\sigma_{lv}$ are constants, we have the Boltzmann distribution for

$$\rho_{xi} = \rho_{0i} \exp\left(-z_i e\psi/kT_l\right), \tag{2.20}$$

where $\rho_{0i}$ is the number density of ion $i$ at $x = 0$. The well-known Poisson equation for the net excess charge density at $x$ reads

$$-\epsilon\nabla^2\psi = \Sigma_i z_i e \rho_{xi}, \tag{2.21}$$

where $\epsilon$ is the absolute permittivity of the solution, which when combined with the Boltzmann distribution, gives the Poisson-Boltzmann (PB) equation

$$\nabla^2\psi = -\frac{\Sigma_i z_i e \rho_{xi}}{\epsilon} \tag{2.22}$$

Differentiating eq.2.20 with $x$ and sum over all the species of ions in the solution, we have

$$\frac{d\Sigma_i \rho_{xi}}{dx} = \frac{\epsilon}{2kT_l}\frac{d}{dx}(\frac{d\psi}{dx})^2. \tag{2.23}$$

Integrating the above expression from $x = 0$ to $x = x$,

$$\Sigma_i \rho_{xi} - \Sigma_i \rho_{0i} = \frac{\epsilon}{2kT_l}(\frac{d\psi}{dx})_x^2. \tag{2.24}$$

The Gibbs-Duhem equation states that $d\mu_i = -sdT_l + v_i dP$, where $v_i$ is the specific number density $[\mathbf{m^3/(number\ of\ ions)}]$, $s$ is the entropy of the system. Under isothermal assumptions and at a fixed point $x$ in the solution, $(d\mu_i/dP)_{x,T} = (1/\rho_{xi})_{x,T}$. Differentiating both sides with $x'$, the distance between the solid-liquid interface and the liquid-vapor interface, we have $(dP/dx')_{x,T} = (\rho_{xi} d\mu_i/dx')_{x,T}$. We could use this equation to find the pressure of the counterions. The change in pressure at $x$ on bringing two surfaces together from infinity ($x' = \infty$ and $P = 0$)

to a distance of $x' = D$ is obtained as

$$\int_{x'=\infty}^{x'=D} dP = \Sigma_i \int_{x'=\infty}^{x'=D} \rho_{xi} \frac{d\mu_i}{dx'} dx' \tag{2.25}$$

$$P_x(D) = -\Sigma_i \int_{x'=D}^{x'=\infty} [z_i e \rho_i (d\psi/dx')_x dx' + kT_l d\rho_{xi}] \tag{2.26}$$

Using eq.2.22 with some manipulation, eq.2.26 becomes

$$P_x(D) = [-\frac{1}{2}\epsilon(\frac{d\psi}{dx})^2_{x(D)} + kT_l \Sigma_i \rho_{xi}(D)] - [-\frac{1}{2}\epsilon(\frac{d\psi}{dx})^2_{x(\infty)} + kT_l \Sigma_i \rho_{xi}(\infty)]. \tag{2.27}$$

Using eq.2.24 to substitute for $\Sigma_i \rho_{xi}(D)$, we find

$$P_{x(D)} = kT_l \Sigma_i \rho_{0i}(D) \tag{2.28}$$

since in the bulk solution when the two surfaces are separately infinitely far away, the ion concentration tends to zero, $\Sigma_i \rho_{xi}(\infty) = 0$. Therefore, the problem of finding the pressure between the two surfaces reduces to finding the total number density of the ions at a separation distance of $D$.

As the Debye length of pure water (pH=7) is on the order of 1 $[\mu\mathbf{m}]$, the electrical double layer would cover the whole nanopore regime (pore radius ranging from 10 to 300 $[\mathbf{nm}]$) and expel the co-ions out of the pore regime. Thus, applying charge conservation inside the thin film regime and neglecting the concentration of the co-ions,

$$ze\rho_{counterion}(D)(\pi r_c^2 - \pi r_i^2)l + \sigma_{sl}(2\pi r_c)l + \sigma_{lv}(2\pi r_i)l = 0. \tag{2.29}$$

we have

$$\rho_{counterion}(D) = \frac{-2(\sigma_{sl}r_c + \sigma_{lv}r_i)}{ze(r_c^2 - r_i^2)} = \Sigma_i \rho_{0i}(D). \tag{2.30}$$

Substituting eq.2.30 back to eq.2.28, we find

$$P_{ele} = \frac{-2kT_l(\sigma_{sl}r_c + \sigma_{lv}r_i)}{ze(r_c^2 - r_i^2)}. \tag{2.31}$$

Note that since $(\sigma_{sl}r_c + \sigma_{lv}r_i)/z$ is always negative, $P_{ele}$ is always positive. The physical meaning of this is that by adding ions into the solution, the liquid becomes more attracted to the solid wall since the wall and counterions attract each other by the electrostatic force. This is also termed as the *Osmotic limit* as the liquid film approaches zero thickness Israelachvili (2011). Therefore, the disjoining pressure could be expressed as

$$\Pi_d = \frac{-A}{6\pi(r_c - r_i)^3} + \frac{-2kT_l(\sigma_{sl}r_c + \sigma_{lv}r_i)}{ze(r_c^2 - r_i^2)}. \tag{2.32}$$

The other extreme case for thick wetting films leads to the conventional terms of $P_{ele} = (\epsilon/2(r_c - r_i)^2)(\pi kT_l/ze)^2$ used extensively in the literature and the derivation is as follows Narayanan et al. (2011); Lu et al. (2015); Pati et al. (2013):

Setting the coordinate system to $x = 0$ at the mid-plane and $x = \pm D/2$ at the two surfaces, we proceed by solving the PB equation (eq.2.22) with two additional critical assumptions that only counterions are present in the solution ($i = 1$) and both the surfaces have identical surface potential. The solution is given in Israelachvili (2011):

$$\psi = \frac{kT_l}{ze} \log\left(\cos^2(Kx)\right), \tag{2.33}$$

where $K$ is a given by

$$K^2 = \frac{(ze)^2 \rho_0}{2\epsilon k T_l}. \tag{2.34}$$

Since $i = 1$, eq.2.28 simply reduces to $P_{ele} = kT_l\rho_0 = 2\epsilon(kT_l/ze)^2K^2$. To find the limiting value of $K$, we differentiate eq.2.33 at $x = \pm D/2$, we find:

$$(\frac{d\psi}{dx})_{surface} = \frac{2kT_lK}{ze} \tan(KD/2). \tag{2.35}$$

As $D \to \infty$ for thick liquid films, $K$ should approach $\pi/D$ to keep $\tan(KD/2)$ finite in eq.2.35. Thus,

$$P_{ele,\ thick\ film} = \frac{\epsilon}{2(r_c - r_i)^2}(\frac{\pi kT_l}{ze})^2. \tag{2.36}$$

This equation is known as the *Langmuir equation*. The major difference between the *Langmuir equation* and the *Osmotic limit* is that for the *Langmuir equation*, the $P_{ele}$ is independent on the surface charge as the liquid film is thick enough to screen the effect of the electrostatic forces originating from the surface charges on the wall. Therefore, the *Langmuir equation* should only be applied to a thin film thickness ($\delta$) where $\delta$ is much larger than the Debye length of the solution and only counterions are allowed to enter the liquid film. Hence the *Langmuir equation* is not suitable for this study and the *Osmotic limit* is a more appropriate expression.

### 2.2.4 Solving the system of equations

The governing eqs.2.8, 2.9, 2.16 and 2.17 form a set of complete equations that we can use to solve the meniscus profile, interface temperature $T_i$, liquid pressure $p_{li}$, as well as the total evaporation rate $\dot{m}$. It is clear from this set of equations that the heat and mass transfer are coupled in three different ways. First, from

eq.2.9, the temperature gradient along the $x$-direction would change the mass flow rate by affecting the surface tension. Secondly, from eq.2.17, the local temperature would also affect the electrostatic disjoining pressure, which is part of the driving force for mass flow. Thirdly, from eq.2.16, the temperature profile of the pore wall is directly correlated to the evaporative heat dissipation.To solve these equations, eqs.2.8, 2.9, 2.16 and 2.17 are first nondimensionalized by $\bar{x} = x/r_c$, $\bar{r} = r_i/r_c$, $\bar{p} = p_{li}/p_v$, $\bar{\dot{m}} = \dot{m}/\dot{m}_0$, and $\bar{T}_{li} = 2\pi r_c k_l (T_{li} - T_w)/\dot{m}_0 h_{fg}$, where $\dot{m}_0$ equals to

$$\dot{m}_0 = \frac{2\hat{\sigma}}{2-\hat{\sigma}} \left(\frac{M}{2\pi R T_w}\right)^{1/2} [p_{vi}(T_w) - p_v](2\pi r_c^2). \tag{2.37}$$

The four governing equations in their nondimensional forms are (we drop the bar for simplicity):

$$\dot{m}\frac{dx}{dr} = \Pi_1(-\frac{dP}{dr})[(1-r^2)(1-3r^3) - 4r^{-4}\ln(r)] + \Pi_2(\frac{dT_{li}}{dr})[4r(1-r^2) + 8r^3 \ln r] \tag{2.38}$$

$$(1 + \Pi_3\Pi_4 T_{li})(1 + \Pi_4 T_{li})^{-1/2} = -\frac{1}{r\sqrt{1 + (dx/dr)^2}}\frac{d\dot{m}}{dr} \tag{2.39}$$

$$\begin{aligned} \Pi_5 - P = \quad & \Pi_6(\tfrac{dx/dr}{r\sqrt{1+(dr/dx)^2}} + \tfrac{d^2x/dr^2}{(1+(dx/dr)^2)^{3/2}}) + \\ & \tfrac{\Pi_7}{(1-r)^3} + \Pi_8(\tfrac{(1+\Pi_9 r)(1+\Pi_4 T_{li})}{1-r^2}) \end{aligned} \tag{2.40}$$

$$\begin{aligned} -\tfrac{d\dot{m}}{dr}(\tfrac{dx}{dr})^2 = \quad & -\tfrac{T_{li}}{1-r}(\tfrac{dx}{dr})^3 + \tfrac{1}{3}T_{li}(\tfrac{dx}{dr}) + \tfrac{1}{3}(1-r)\tfrac{dx}{dr}\tfrac{dT_{li}}{dr} - \\ & \tfrac{1}{6}(1+2r)T_{li}\tfrac{\partial^2 x}{\partial r^2} + \tfrac{1}{6}(1+2r)(1-r)[(\tfrac{dx}{dr})(\tfrac{d^2T_{li}}{dr^2}) - \tfrac{d^2x}{dr^2}\tfrac{dT_{li}}{dr}]. \end{aligned} \tag{2.41}$$

The nondimensional groups are:

$$\Pi_1 = \frac{\pi \rho_l r_c^3 p_v}{8\mu_l \dot{m}_0} \tag{2.42}$$

$$\Pi_2 = \frac{\rho_l r_c h_{fg}}{16\mu_l k_l}(\frac{d\sigma}{dT_{li}}) \tag{2.43}$$

$$\Pi_3 = \frac{\rho_v h_{fg}}{p_{v,eq} - p_v} \tag{2.44}$$

$$\Pi_4 = \frac{\dot{m}_0 h_{fg} r_c}{k_l T_w} \tag{2.45}$$

$$\Pi_5 = \frac{p_{atm}}{p_v} \tag{2.46}$$

$$\Pi_6 = \frac{\sigma}{r_c p_v} \tag{2.47}$$

$$\Pi_7 = \frac{-A}{6\pi r_c^3 p_v} \tag{2.48}$$

$$\Pi_8 = \frac{-2kT_w\sigma_{sl}}{zer_c p_v} \tag{2.49}$$

$$\Pi_9 = \frac{\sigma_{lv}}{\sigma_{sl}} \tag{2.50}$$

The systems of ODEs are solved by ode45 in MATLAB and the boundary conditions at $x = 0$ for the problem is

1. $r = r_0 = r_c - t_0$, where $t_0$ is the absorbed thin film thickness.

2. $dr/dx = 0$ as the slop is assumed to be flat.

3. $\dot{m} = 0$ since no evaporation happens in the absorbed thin film regime.

4. $p = \Pi_5 - \Pi_6/r_0 - \Pi_7/(1 - r_0)^3 - \Pi_8(1 + \Pi_9 r_0)/(1 - r_0^2)$.

5. $T = 0$, assuming $T_{li} = T_w$

6. $dT/dx = 0$

The absorbed thin film thickness $t_0$ is obtained by the same method as in Narayanan et al. (2011) and is omitted here for brevity.

## 2.3 RESULTS AND DISCUSSIONS

### 2.3.1 Effect of the solid-liquid surface charge density

The effect of the surface charge on the meniscus shape of the kinetically-limited evaporation is shown in fig.2.3, corresponding to $r_c = 50$ [**nm**], $T_w = 90$ °C, and $RH$ = 0.3.

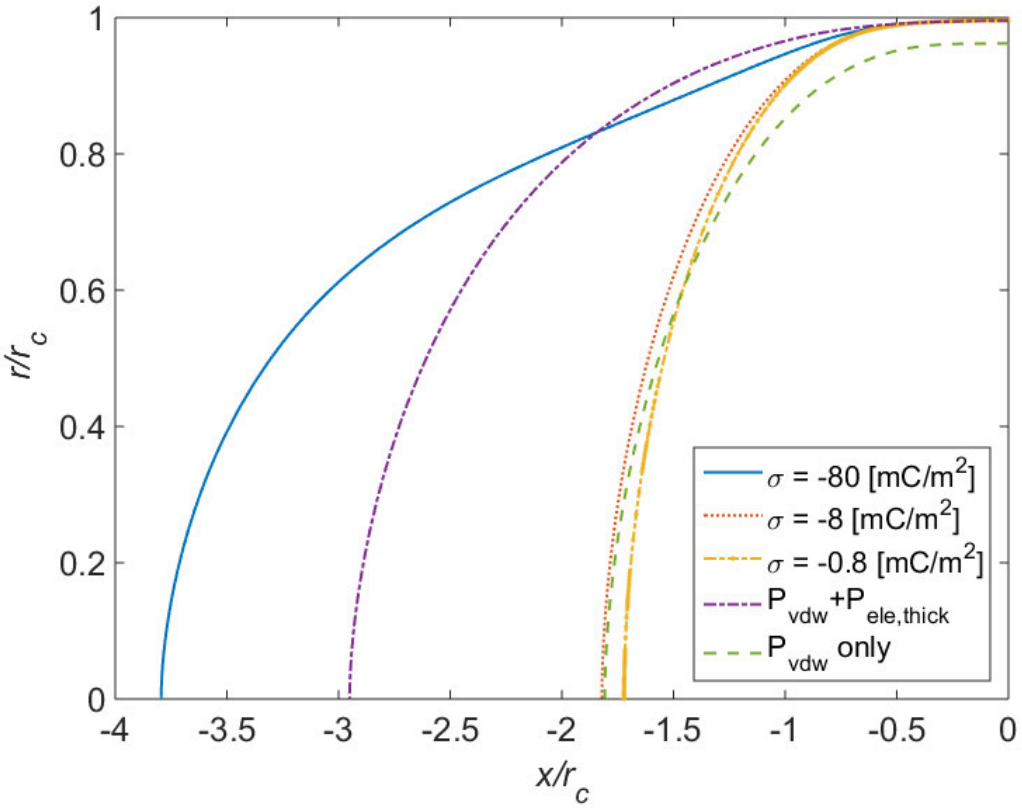


**Figure 2.3:** Effect of the surface charge density on the shape of the water meniscus for $r_c = 50$ [**nm**], $T_w = 90$ °C, and $RH$ = 0.3.

A typical surface charge density value is in the range from 0 to -50 [$\mathbf{mC/m^2}$] for silica, carboxyl, and sulfate surfaces Behrens & Grier (2001). Thus, the surface charge density value for $\sigma_{sl}$ in this work is selected as -80, -8, and -0.8 [$\mathbf{mC/m^2}$] to demonstrate the effect of charges on the evaporation kinetics. Meanwhile, the

surface charge density for the liquid-vapor interface is kept at a constant of -2.4 $[\mathbf{mC/m^2}]$ unless stated otherwise. It is shown that as the magnitude of the charge density increases, the total interface area of the meniscus inside the nanopore increases. This is because the unique shape of the evaporating interface is the result of balancing the forces acting on the meniscus with the viscous pressure loss to supply enough water for evaporation. In addition, the meniscus shape with the Langmuir equation and with only the $P_{vdw}$ term are also shown in the figure as the dash-dot purple line and the dash green line, respectively. An interesting observation is that the meniscus would be extended further than the Langmuir equation only with a surface charge density of -80 $[\mathbf{mC/m^2}]$ while it barely extends with a surface charge density of -8 and -0.8 $[\mathbf{mC/m^2}]$. Near the center of the meniscus where the disjoining pressure decreases rapidly in magnitude as shown in fig.2.4, the meniscus must be highly curved to increase the capillary pressure gradient to sustain the required mass flux.

On the other hand, as the meniscus approaches the pore wall ($x/r_c \rightarrow 0$), the liquid film becomes thinner and the disjoining pressure significantly increases in magnitude. Therefore, the disjoining pressure gradient is large enough to drag sufficient water for evaporation and the meniscus becomes less curved. As a result, as long as we actively tune the disjoining pressure to a larger value, the meniscus would be further extended. In fact, we had demonstrated this via introducing a larger surface charge density on the wall as the wall attracts the ions with a stronger electrostatic force and increases the disjoining pressure. This could be justified by studying the magnitudes of the components of the disjoining pressure inside the liquid as shown in fig.2.4. As the surface is slightly charged ($\sigma_{sl} = -0.8$ $[\mathbf{mC/m^2}]$), $P_{vdw}$ dominates $P_{ele}$ as $x/r_c$ is less than -1. However, as

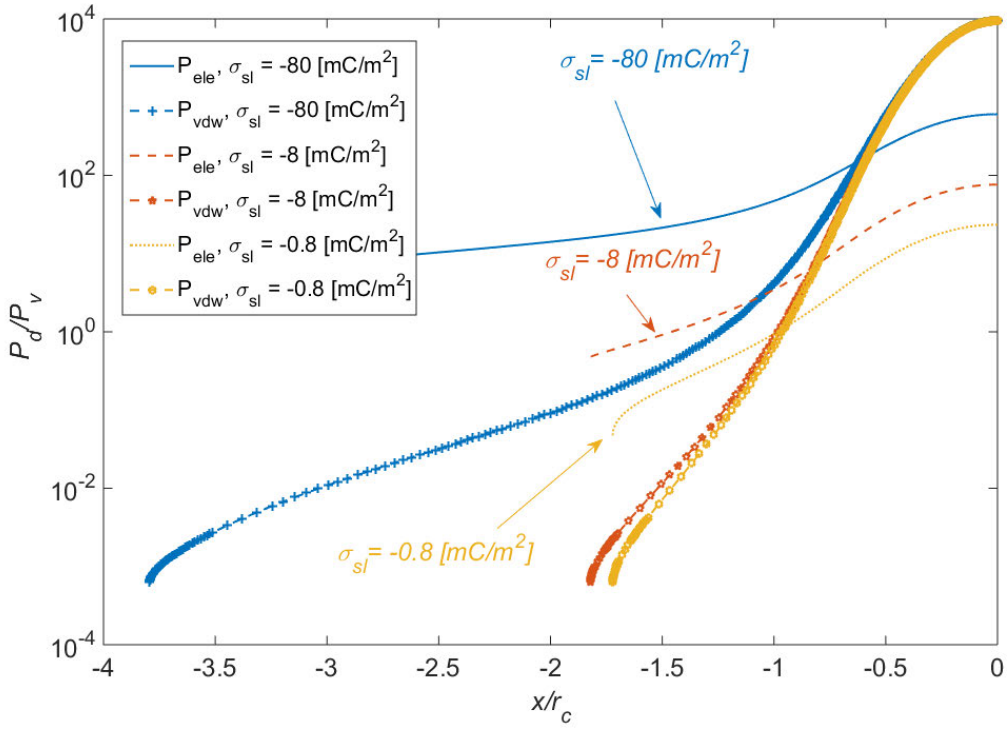


**Figure 2.4:** Axial variation of the normalized disjoining pressure for different surface charges from -80 to -8, and -0.8 $[\mathbf{mC/m^2}]$ with $r_c = 50$ $[\mathbf{nm}]$, $T_w = 90$ ° C, and $RH$ = 0.3. Same color represents the same surface charge. Lines with markers represent $P_{vdw}$ while lines without markers represent $P_{ele}$.

the charge density increases to -80 $[\mathbf{mC/m^2}]$, the regime where $P_{ele}$ prevails over $P_{vdw}$ prolonged to $x/r_c \sim -0.5$ and drastically extends the meniscus area from $x/r_c \sim -1.8$ to $x/r_c \sim -3.8$. Zou et al. (2021).

The corresponding mass flux evaporated from a charged nanopore is shown in fig.2.5. First, by considering the slightest extension of the meniscus due to $P_{vdw}$ only, the mass flux has been increased from 24.12 to 103.85. This shows that the mass flux would be significantly underestimated with the Schrage equation alone, which represents the traditional limit of evaporation from nanopores. Secondly, it is observed that the mass flux increases from 107 to 237.4 $[\mathbf{kg/m^2s}]$ monotonically

as the magnitude of the surface charge increases from 0 to -100 $[\mathbf{mC/m^2}]$. This result is outstanding since we achieved a 121% increase in mass flux by simply charging the wall. The corresponding heat flux is 53.7 $[\mathbf{kW/cm^2}]$, which greatly exceeds the required heat flux of 1 $[\mathbf{kW/cm^2}]$ to dissipate heat from GaN-based electronics Bagnall (2013).

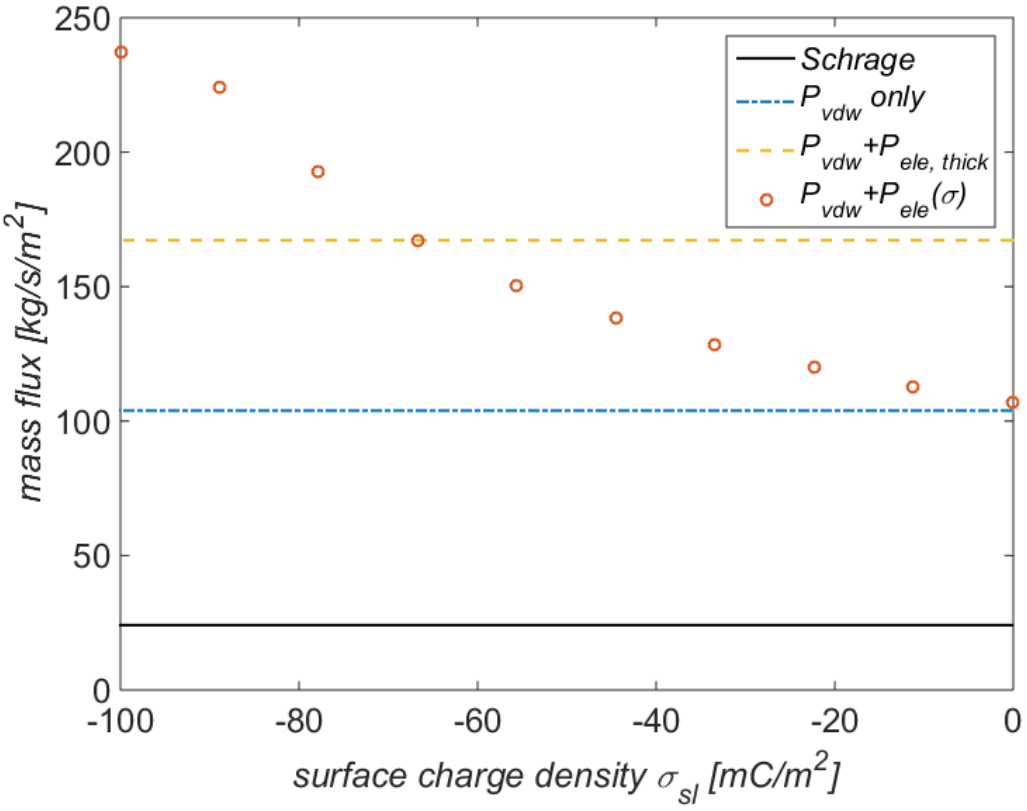


**Figure 2.5:** The effect of surface charge on the evaporation mass flux from a nanopore (orange dots) for $r_c = 50$ $[\mathbf{nm}]$, $T_w = 90$ °C, and $RH$ = 0.3. The mass flux increases monotonically as the magnitude of the surface charge increases. The blue line represents the mass flux from a nanopore without considering $P_{ele}$.

### 2.3.2 Effect of the liquid-vapor surface charge density

So far, we have only considered a constant surface charge density of -2.4 $[\mathbf{mC/m^2}]$ on the liquid-vapor interface. However, this value is actually scattering from -2.4 to -70 $[\mathbf{mC/m^2}]$ on the literature Himanshu (2013); Poli et al. (2020). Therefore, we select $\sigma_{lv} = -2.4$, $-36$, and $-70$ to demonstrate the effect of the liquid-vapor surface charge density on the meniscus shape. The results are plotted in fig.2.6 with $r = 50$ **nm**, $\sigma_{sl} = -0.8$, $\hat{\sigma} = 0.3$ and $RH$ = 0.3.

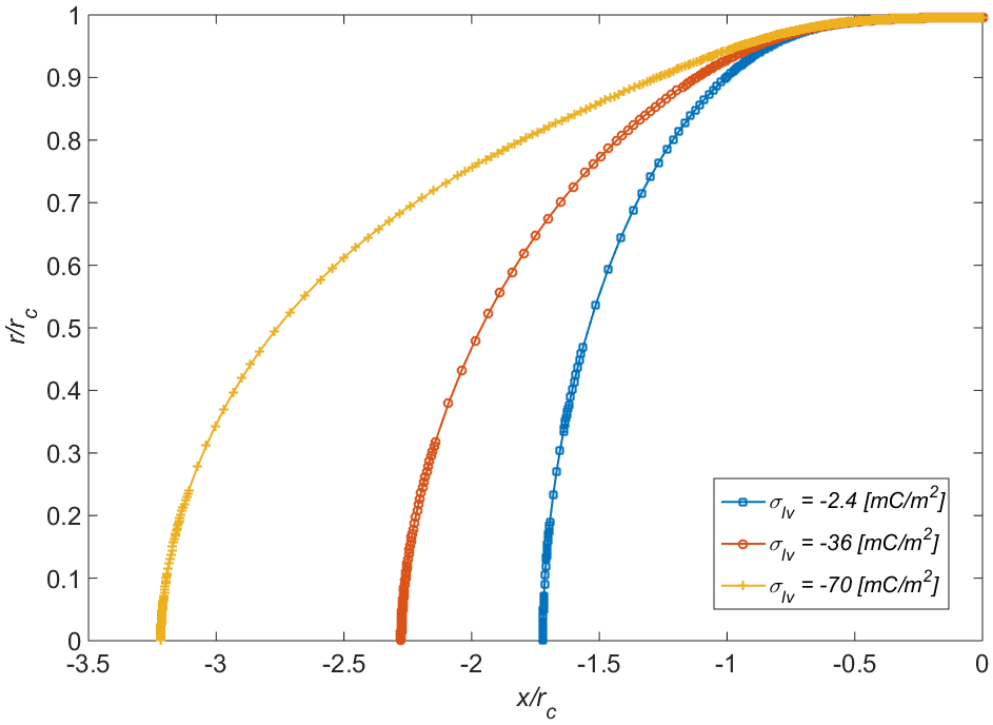


**Figure 2.6:** The effect of the liquid-vapor surface charge density on the meniscus shape corresponding to $r = 50$ **nm**, $\sigma_{sl} = -0.8$, $\hat{\sigma} = 0.3$, and $RH$ = 0.3. The inset compares the average mass flux $[\mathbf{kg/m^2s}]$ at different $\sigma_{lv}$.

It is shown that increasing the surface charge density on the liquid surface has the exact same effect of increasing the surface charge density on the solid surface

- the meniscus becomes further extended and the mass flux increases. We further plot the effect of the surface charge density on the liquid-vapor interface versus the mass flux in fig.2.7 at various $\sigma_{sl}$.

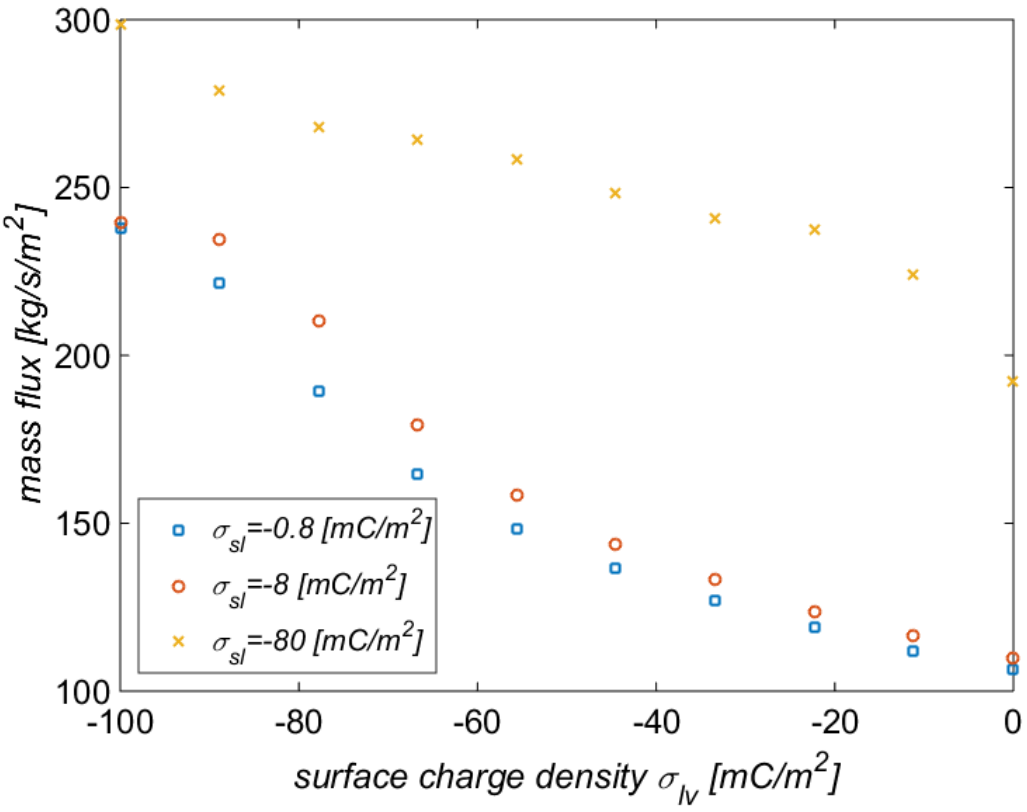


**Figure 2.7:** The effect of surface charge density on the liquid-vapor interface $\sigma_{sl}$ on the evaporation mass flux from a nanopore for $r_c = 50$ [**nm**], $T_w = 90$ °C, and $RH$ = 0.3. The mass flux increases monotonically as the magnitude of $\sigma_{sl}$ increases.

It can be shown that for all $\sigma_{sl}$, the mass flux increases as $\sigma_{lv}$ increases. In addition, the maximum mass flux could reach up to 300 [$\mathbf{kg/m^2s}$] if the surface charge density of the liquid-vapor interface is -100 [$\mathbf{mC/m^2}$]. However, it remains illusive of what the exact value of the surface charge density on the liquid-vapor interface is in a nanopore. Further experimental study on this topic is encouraged

in order to provide better quantitative predictions for realistic conditions.

### 2.3.3 Pore radius effect

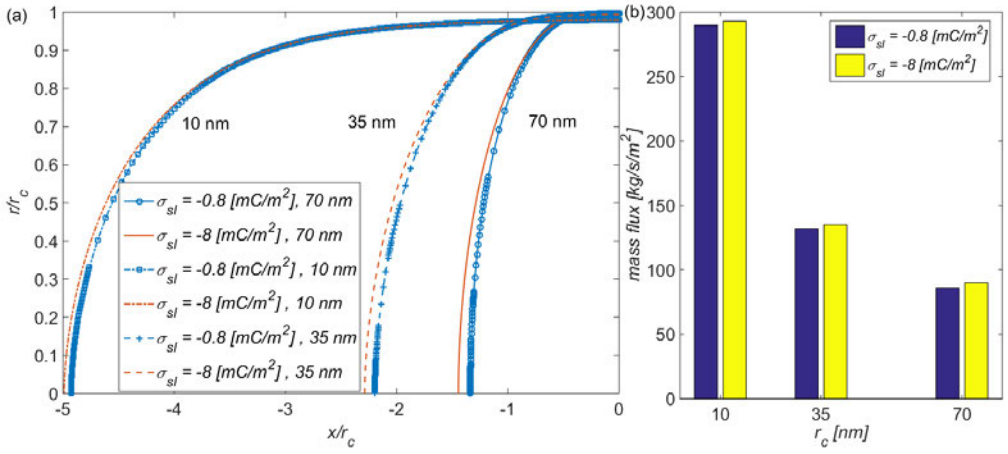


**Figure 2.8:** Effect of pore radius on the meniscus shape and evaporation mass flux. (a) The radius effect on the meniscus shape with different surface charge densities corresponding to $T_w = 90$ °C and $RH$ = 0.3. The dashed-dot lines represent $r = 10$ $[\mathbf{nm}]$; the dashed lines represent $r = 35$ $[\mathbf{nm}]$; the solid lines represent $r = 70$ $[\mathbf{nm}]$. The lines with markers represent a surface charge density of -0.8 $[\mathbf{mC/m^2}]$ while lines without markers represent a surface charge density of -8 $[\mathbf{mC/m^2}]$. (b) The corresponding evaporation mass flux at $T_w = 90$ °C and $RH$ = 0.3.

Fig.2.8 shows the effect of the pore radius on the meniscus shape for $T = 90$ °C and $RH$ = 0.3. It is observed the meniscus becomes more extended as the pore radius reduces, and this trend is the same for different values of surface charge densities. As a result of the meniscus extension, smaller nanopores exhibit larger evaporation fluxes (see fig.2.8(b)). Taking $\sigma_{sl} = -8$ $[\mathbf{mC/m^2}]$ as an example, the evaporation flux is only 86 $[\mathbf{kg/s/m^2}]$ for the nanopore with a radius of 70 $[\mathbf{nm}]$, but reaches 293 $[\mathbf{kg/s/m^2}]$ for the nanopore with a radius of 10 $[\mathbf{nm}]$. One possible explanation for the more extended meniscus and larger evaporation flux in the

smaller nanopore is that the disjoining pressure increases with the decreasing pore radius. To verify this explanation, we plot $P_d$ (measured from the non-evaporating thin film) V.S. the pore radius in fig.2.9 with $T = 90$ °C, $RH = 0.3$ and $\hat{\sigma} = 0.3$. The orange diamond represents the data with $\sigma_{sl} = -8$ $[\mathbf{mC/m^2}]$ while the blue triangle represents $\sigma_{sl} = -0.8$ $[\mathbf{mC/m^2}]$. Surprisingly, we actually found that $P_d$ would slightly decrease with the decreasing radius, varying from 202 to 196 **[MPa]** as the pore radius decreases from 70 to 10 **[nm]**. This decreasing trend and the magnitude of the disjoining pressure is consistent with the previous modeling study reported by Narayanan *et al.* Narayanan et al. (2011) The large disjoining pressure results from the ultrathin non-evaporating thin film thickness and the decreasing trend of the disjoining pressure can be attributed to the increasing non-evaporation thin film thickness in smaller nanopores Narayanan et al. (2011). As show in the inset figure of fig.2.9, the thickness of the non-evaporating thin film indeed slightly decreases as the pore radius increases. However, this trend is different from what has been reported in a recent experimental study by Zou *et al.* Zhou et al. (2019), where the water disjoining pressure in nanochannels was calculated based on wicking experiments and molecular dynamics (MD) simulation of contact angle. Also, the magnitude of our calculated disjoining pressure in nanopores is two orders of magnitude higher than their results in nanochannels. We attribute these difference to the difference in experiments (i.e., evaporation V.S. wicking), simulation methods (i.e., continuum modeling V.S. MD simulation), operating conditions (including temperature and humidity) as well as nanoconfinements (1-D confined nanochannel V.S. 2-D confined nanopores).

Nevertheless, our modeling results show that the increasing extension of the evaporation area in smaller nanopores does not stem from the increasing disjoin-

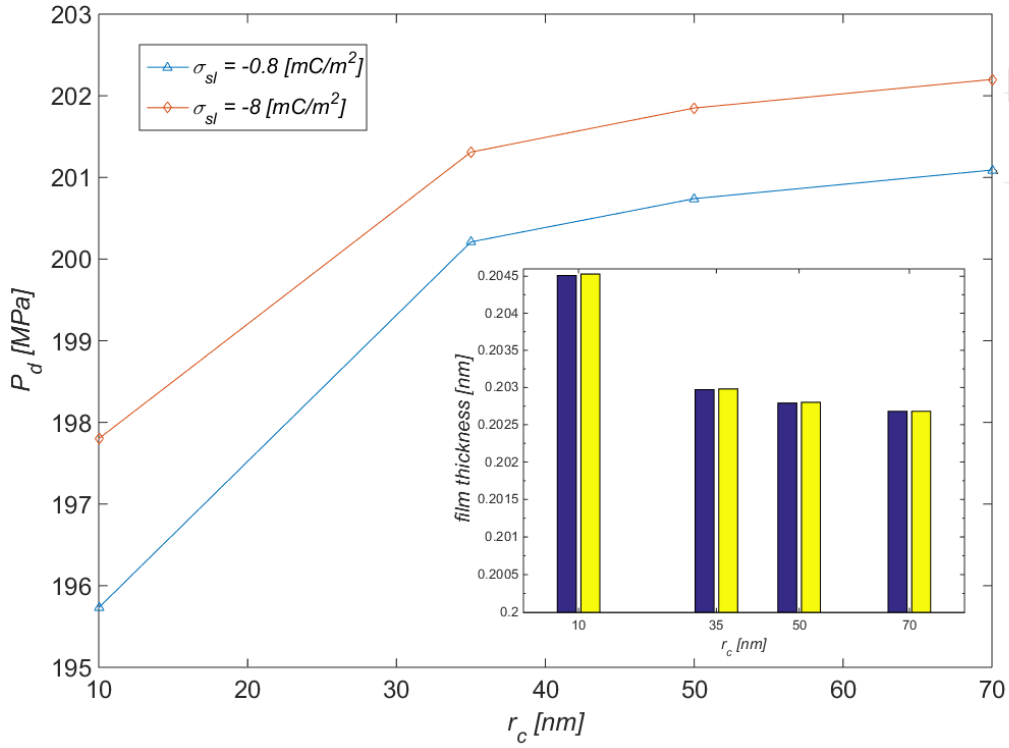


**Figure 2.9:** The disjoining pressure versus the pore radius with different solid-liquid surface charge densities with $T = 90°\text{C}$, $RH = 0.3$, and $\hat{\sigma} = 0.3$. The inset figure shows the liquid film thickness versus the pore radius.

ing pressure. Instead, we believe that it is a result of relatively larger range of disjoining pressure in smaller nanopores. fig.2.10 shows the axial variation of capillary and disjoining pressure for nanopores of pore radii 10 and 70 [**nm**] at two different surface charge densities. It is clear that the disjoining pressure is significant over a larger portion of the interface in the smaller nanopore. At the surface charge density of -0.8 [$\mathbf{mC/m^2}$], the regimes where the magnitude of the disjoining pressure is significant ($P_d/P_v \geq 1$ ) ends at $x/r_c \sim -4.5$ for nanopore with a pore radius of 10 [**nm**] and at $x/r_c \sim -0.5$ for nanopore with a pore radius of 70 [**nm**], respectively. Consequently, fluid flow can be sustained over a relatively longer re-

gions in smaller nanopores, leading to the more extended meniscus and the higher evaporation flux per pore area. It is worth noting that when the surface charge density increases to -8 $[\mathbf{mC/m^2}]$, $P_{ele}$ increases and the region where the disjoining pressure is significant becomes even larger, ending at $x/r_c \sim -5$. This further extension of the meniscus also leads to an increase in the evaporation mass flux as demonstrated in the inset of fig.2.8.

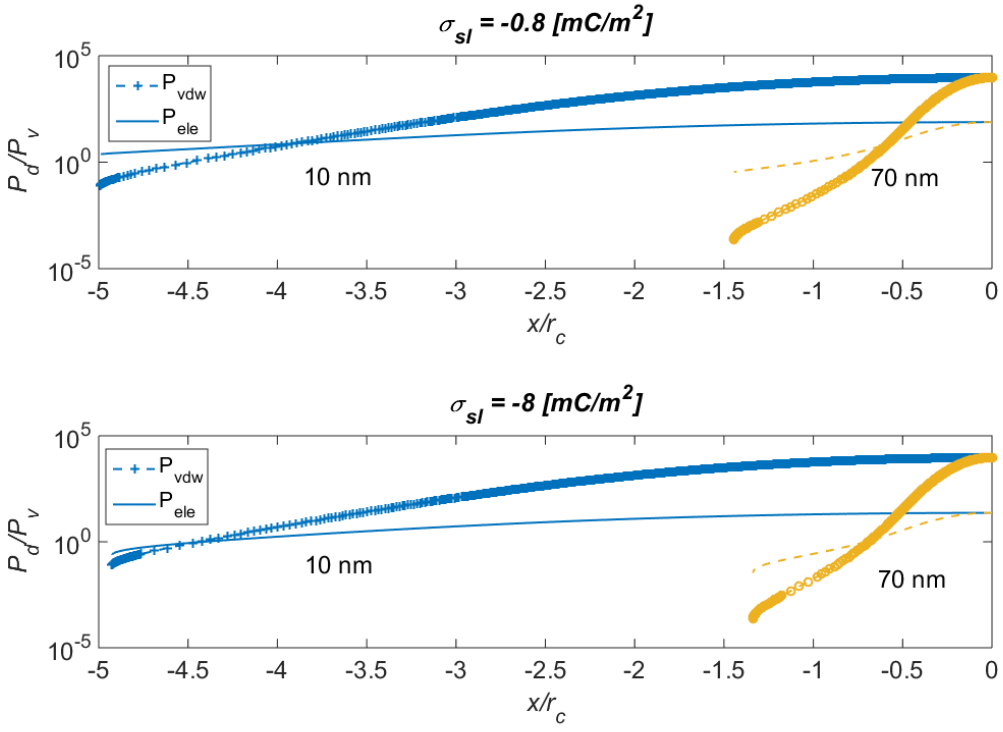


**Figure 2.10:** Axial variation of the normalized disjoining pressure for different surface charges at -0.8 and -8 $[\mathbf{mC/m^2}]$ with different pore radius of 10 and 70 $[\mathbf{nm}]$ at $T_w = 90$ °C, and $RH$ = 0.3. Same color represents the same radius. Lines with markers represent $P_{vdw}$ while lines without markers represent $P_{ele}$.

### 2.3.4 Thermocapillary stresses in nanopores with various surface charge densities

The effect of the thermocapillary stresses on the meniscus shape is presented in fig.2.11 at 90 °C with $RH$ = 0.3.

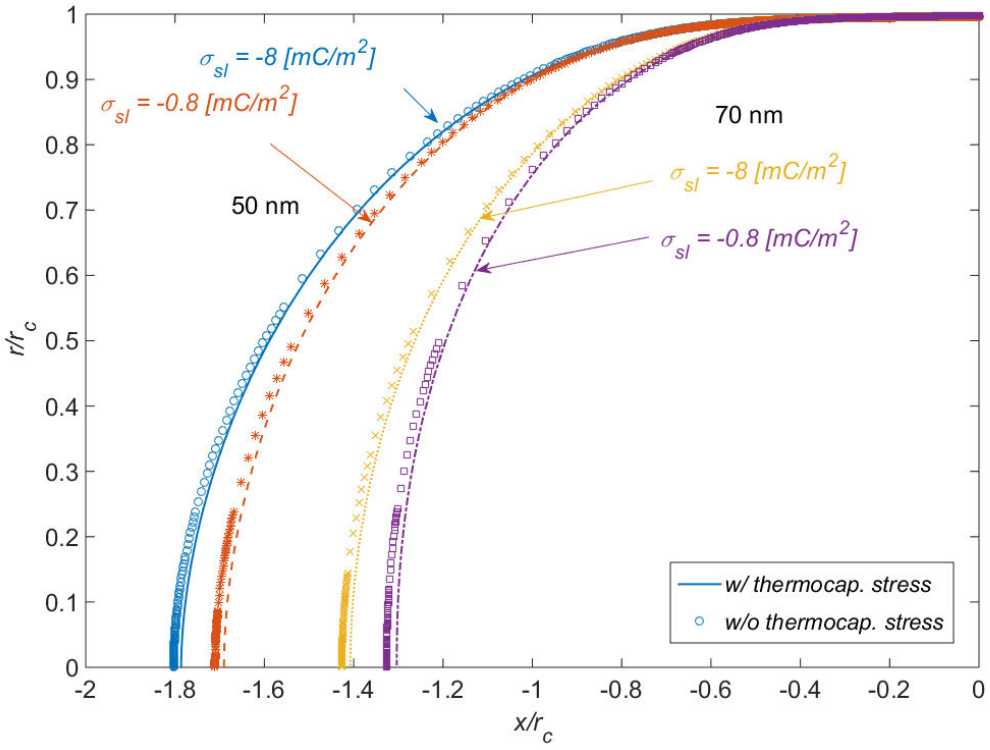


**Figure 2.11:** The effect of the thermocapillary stresses on the meniscus shape with different surface charge densities corresponding to $T_w$ = 90 °C and $RH$ = 0.3. The lines represent results with thermocapillary stresses while the markers represent results without thermocapillary stresses.

The predictions with the thermocapillary stresses are plotted in solid lines while the results without the thermocapillary stresses are plotted in dotted markers. As shown in the figure, the thermocapillary effect has negligible effect on the meniscus shape for all of the cases considered (either 50 or 70 [nm] pores with -8

or -0.8 $[\mathbf{mC/m^2}]$). This can be justified by observing the temperature change along the interface. The results are summarized in Table 2.1 and the maximum temperature change along the meniscus is 3.98 °C. The corresponding maximum surface tension change is $6.88 \times 10^{-4}$ $[\mathbf{N/m}]$, which is around 1% of the original value and is negligible. These results show that the temperature gradient along the meniscus is not significant to affect the evaporation mass flux.

| max $\Delta T_{li}$ | 50 $[\mathbf{nm}]$ | 70 $[\mathbf{nm}]$ |
|---|---|---|
| -8 $[\mathbf{mC/m^2}]$ | 2.0802 °C | 3.2866 °C |
| -0.8 $[\mathbf{mC/m^2}]$ | 2.5829 °C | 3.9809 °C |

**Table 2.1:** Temperature difference along the liquid-vapor interface.

### 2.3.5 Temperature and relative humidity effect

Although the thermal capillary effect only causes negligible change of the evaporation area and evaporation flux, the operating temperature can still significantly affect the evaporation performance via the other two coupling mechanisms. Fig.2.12 demonstrates the effect of the wall temperature on the meniscus shape and the evaporation mass flux with different surface charge densities with $r = 50$ $\mathbf{nm}$ and $RH$ = 0.3.

It is observed that the length of the meniscus reduces as the temperature increases from 20 to 90 °C yet the average mass flux increases as the temperature increases. This dramatic jump in the performance is due to a higher vapor pressure at the interface. The magnitude of $\Pi_8$ decreases from 1.4286 to 0.0583. The decrease in this term results in a lower driving force for liquid flow into the thin film regime. Thus, the gradient of the curvature must be higher at a higher temperature to sustain a higher evaporation rate. This in turn results in a contraction of the meniscus.

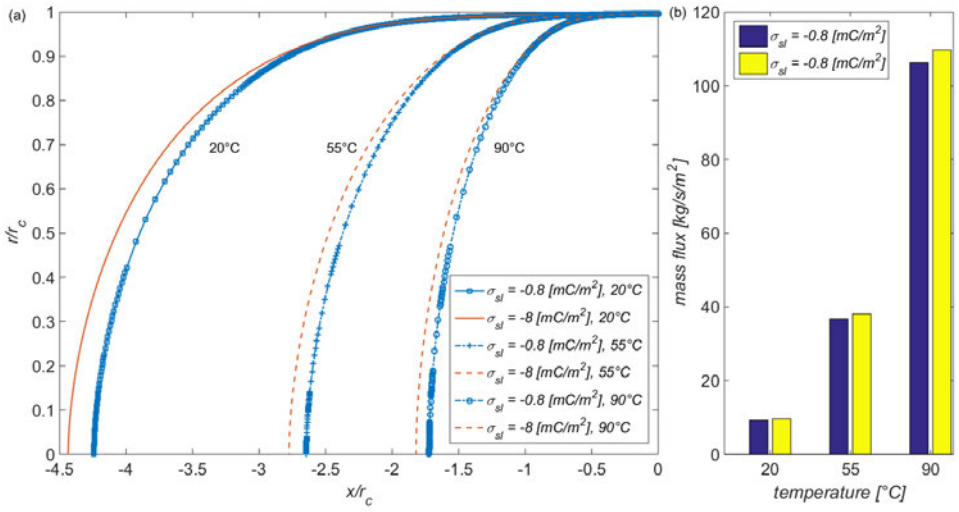


**Figure 2.12:** Effect of temperature on the meniscus shape and evaporation flux. (a) The temperature effect on the meniscus shape with different surface charge densities corresponding to $r = 50$ $[\mathbf{nm}]$ and $RH$ = 0.3. Lines with markers represent a surface charge density of -0.8 $[\mathbf{mC/m^2}]$ while lines without markers represent a surface charge density of -8 $[\mathbf{mC/m^2}]$. (b) The corresponding evaporation mass flux $[\mathbf{kg/m^2s}]$ at two different surface charge densities.

Interestingly, this trend is counter-intuitive and is in conflict with the results published in Lu et al. (2015), where the meniscus shape should start flat and becomes fully extended as the temperature increases to drive more water to the meniscus area. Further experimental work is encouraged to justify this trend. In addition, the meniscus shape becomes more extended as the surface charge density increases at a given temperature. This is because that as the surface charge density increases, the disjoining pressure term increases, leading to a smaller gradient of curvature locally and extends the meniscus further. This results in an increase in the average mass flux as shown in Fig.2.12b.

Fig.2.13 shows the shape of the meniscus at different relative humidity and different surface charge densities. Notice that while the Schrage equation states

that the mass flux from nanopores is linearly proportional to the relative humidity, the results from this study suggests a non-linear trend as shown in Fig.2.13b.

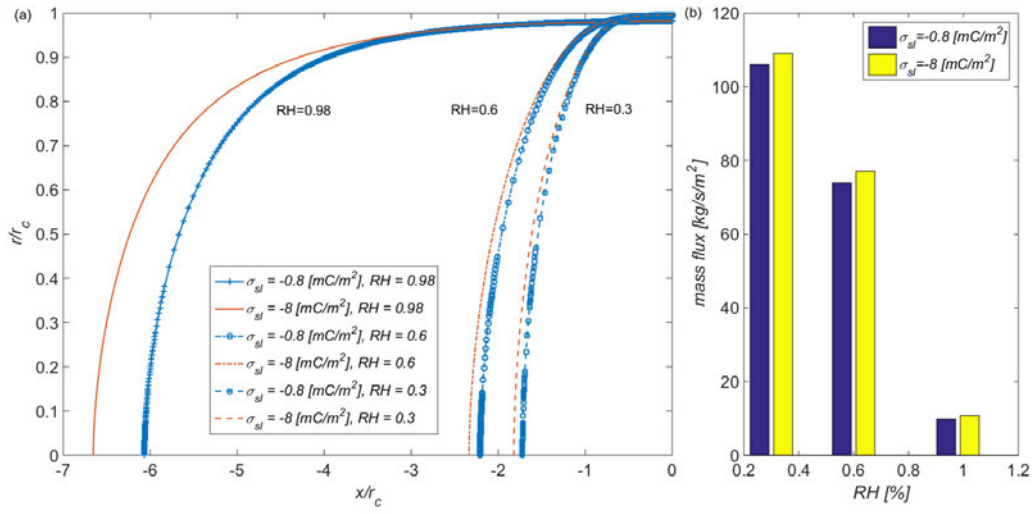


**Figure 2.13:** Effect of relative humidity on the meniscus shape and the evaproation mass flux. (a) The relative humidity effect on the meniscus shape with different surface charge densities corresponding to $r = 50$ **nm** T = 90 °C. Lines with markers represent a surface charge density of -0.8 $[\mathbf{mC/m^2}]$ while lines without markers represent a surface charge density of -8 $[\mathbf{mC/m^2}]$. (b) The corresponding evaporation mass flux $[\mathbf{kg/m^2s}]$ at two different surface charge densities.

The discrepancy comes from the consideration of the extended meniscus. In addition, the effect of increasing the relative humidity is to decrease the potential for evaporation and is analogous to the effect of decreasing the temperature. As a result, the meniscus extended further as the relative humidity increases.

### 2.3.6 Comparison with literature data

Fig.2.14 compares the ratio between the theoretical mass flux obtained in this work at $T_w = 20$ $[\mathbf{°C}]$, $P_v = 150$ $[\mathbf{Pa}]$ and $RH$ = 0.3 with the experimental data obtained in Li et al. (2019) as a function of the pore radius. The surface charge density

reported in Li et al. (2019) is in the range from -2 to 0 $[\mathbf{mC/m^2}]$ and the corresponding theoretical mass flux is relatively insensitive to the surface charge density in this range. Meanwhile, the surface charge density on the meniscus is assumed to be a constant at -2.4 $[\mathbf{mC/m^2}]$ Poli et al. (2020). It is shown that the mass flux ratio ($\dot{m}''_{theo}/\dot{m}''_{exp}$), which is an indicator of the degree of discrepancy between the theoretical value and the data, is larger than one, implying that all of the experiment data is below the theoretical value. More importantly, the mass flux ratio increases from 9.3 to 21.3 as the pore radius decreases from 152.3 to 13.9 $[\mathbf{nm}]$. We believe the increase of the difference between the theoretical value and the data originates from the shape of the meniscus.Since the nanopore devices for the experimental studies are specifically designed to ensure that liquid transport to the evaporation interface is not the transport limit, the meniscus shape may not correspond to the fully extended case. In fact, based on the measured evaporation rates and the device dimensions, we can calculate the corresponding apparent contact angle for all the experimental cases. As shown in the inset of Fig. 14, the apparent contact angle actually increases from 21.2 to 83.8 as the nanopore radius decreases from 152.3 to 13.9 $[\mathbf{nm}]$, indicating that the meniscus is the flattest when the pore radius is 13.9 [nm]. In contrary, the theoretical model in this work calculates the fully extended meniscus for all nanopores and our results show that smaller nanopores would have more extended menisci and thus more evaporation area inside the nanopores. Such difference of the meniscus shape thus would lead to the observed large difference between the theoretical predictions and the reported experimental results and smaller nanopores are expected to show larger difference. This figure is significant because it demonstrates the importance of carefully designing the conduit hydraulic resistance at a known working temperature - we can simply engineer

the conduit geometry profile and increase the hydraulic resistance to obtain a fully extended meniscus, leading to a higher evaporation mass flux. This is in contradictory to the mainstream articles Lu et al. (2019, 2016); Narayanan et al. (2013); Lu et al. (2017); Hanks et al. (2018) where the hydraulic resistance is minimized with multi-tier structures.

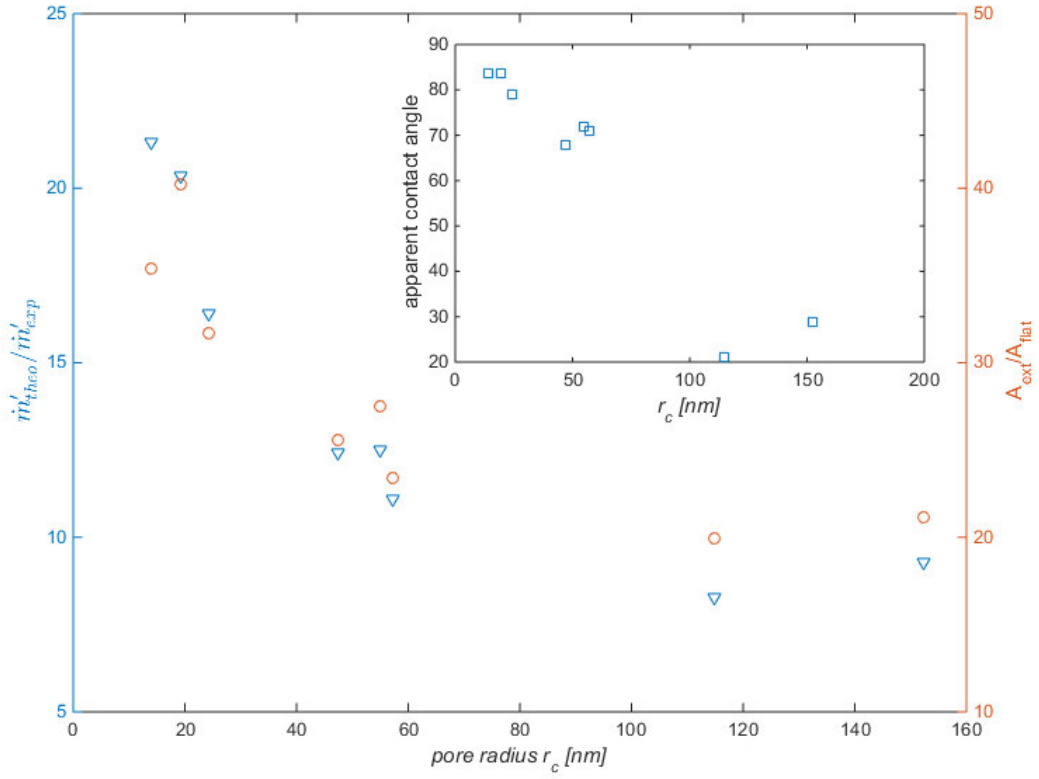


**Figure 2.14:** The ratio of theoretically computed mass flux versus experiment data obtained from Li et al. (2019) with $T_w = 20$ °C, $P_v = 150$ [**Pa**] and $RH$ = 0.3. The inset figure shows the apparent contact angle as a function of pore radius obtained from Li et al. (2019).

Finally, it is worth pointing out the difference of the fundamental mechanism leading to the increase of evaporation mass flux in this work and in Li et al. (2019). In Li's hypothesis, the proton concentration inside the nanopore regime is the key

factor, and the evaporation flux would be higher given a higher proton concentration. Hence, as the pore diameter becomes smaller, the proton concentration would increase due to the charge conservation equation as the electrical double layer overlaps with each other, $[\mathbf{H_3O^+}] \propto r^{-1}$. This would lead to a higher evaporation mass flux even if the meniscus is flat, as reported in their SI. However, in this analysis, the mechanism that leads to an increase in the mass flux is due to a larger evaporating area inside the pore. Thus, if the meniscus shape remains flat, the evaporation flux would not increase as the pore radius decreases. Furthermore, the accommodation factor increases as the pore radius decreases in Li et al. (2019) while in this work, the evaporation coefficient remains a constant $\hat{\sigma} = 0.3$, which is in line with Lu et al. (2019). Further experiments and simulations should be conducted to address these issues and to verify the effect of surface charges on evaporation kinetics.

It is worth noting that we only model traditional hydrophilic nanopores in this study where the nanopore surface in contact with the water is hydrophilic and the thickness of the nanopore is hundreds of nanometers. We believe only contact angle below 90 degree can induce negative liquid pressure and capillary flow to ensure liquid water supply to the evaporation interface. Since hydrophobic pores do not provide such characteristics in theory, our model would not apply to this situation. It is also note worthy that a recent article published by Xiao et. al. Xiao et al. (2022) did evaporation experiments with graphene nanopores and claimed that such device had a better performance than SiN counterparts under a pore diameter of 60 $[\mathbf{nm}]$. However, since the contact angle of graphene is still on a heated debate Prydatko et al. (2018); Belyaeva & Schneider (2020) and the membrane is only an atom thick, we avoid comparing their experiment data with this study to

prevent further confusion. Further development is needed for addressing the theoretical maximum evaporation mass flux for hydrophobic pores and the thickness effect of the membrane on the evaporation kinetics.

In this chapter, we numerically explored the effect of the pore wall and the meniscus surface charge densities on the kinetically-limited evaporation. We found that the increase of the mass flux from a single nanopore is majorly due to the extension of the meniscus originating from a stronger disjoining pressure.

# CHAPTER 3

# Experimental investigation of tuning kinetically-limited evaporation in nanopore by adjusting meniscus area

## 3.1 INTRODUCTION

Exciting opportunities have been presented for nanoscale evaporators in the past decade. Theories had been developed to address the potential increase of evaporation mass flux from nanopores due to the long-range electrostatic force Narayanan et al. (2011), the slip effect Pati et al. (2013), and the short-range hydrophobic force stemming from the introduction of nanoparticles inside a nanopore Dwivedi & Singh (2022). A general consensus is that as the disjoining pressure becomes higher, the evaporation mass flux from nanopores would increase due to the extended meniscus Li et al. (2017, 2019); Lu et al. (2017); Hanks et al. (2018); Lu et al. (2019); Hanks et al. (2020). However, based on the experiment data, we concluded that the evaporation rate decreases with the increase of meniscus area, indicating the actual evaporation coefficient decreases, which may be caused by the stronger h-bond or the disturbance of the surface charge density.

## 3.2 EXPERIMENT METHOD

Our previous modeling work pointed out that the meniscus area plays a critical roll in determining the performance of evaporation from nanopores at a given working condition. One promising method to actively tune the area is to tune the hydraulic resistance of the water supply conduit. Since the volume flow rate ($Q = \Delta P/R_t$), where $\Delta P$ is the pressure drop across the conduit ($\Delta P \propto 4\sigma_l \cos\theta/d$) and $R_t$ is the total hydraulic resistance of the nanochannel ($R_t = 12\mu l_c/wh^3 + 128\mu l_p/\pi d^4$

N), is constant at a known condition, $\Delta P$ must increase as $R_t$ increases and hence $\theta$ should decrease to increase $\cos\theta$. As $\theta$ decreases, the meniscus is further extended into the nanopore and the meniscus area becomes larger. On the other hand, we can tune the hydraulic resistance by altering the conduit height since $R_t \propto h^{-3}$. Therefore, we prepared three channel heights: 66, 91, and 121 nm with constant channel length and width of 1 mm and 5 $\mu$m, respectively, to observe the effect of the meniscus on the evaporation rate from nanopores.

The materials and experimental setup are similar to previous studies published from our group Li et al. (2019, 2017). The fabrication steps are similar to Li et al. (2019). After anodic bonding, we rinse the chip inside ethanol and octanethiol for 2 hours to create a self-assembled monolayer on the gold layer. This could prevent water film expanding outside of the nanopore during the evaporation experiment. A subsequent cleaning with ethanol and water bath is used to clean extra thiol on the surface. Immediately after surface modification, we dry the whole chip under vacuum (by what machine, 350 Pa) to remove any organic compounds that could possibly affect the evaporation rate of pure water. DI water is then introduced into the reservoir as shown in fig.3.1(a). There are two types of channels used in this study - one with open nanopores (termed as open channels) and the other with sealed SiN membrane (termed as closed channels). After water filled the channels, the open ones would dissipate air bubbles with in 10 minutes while the closed channels would take up to 2 hours to dissolve air completely inside the channels. As the channels are fully filled with water with no bubbles visible in the system as shown in fig.3.1(b), we would apply vacuum (ranging from 1400 to 350 Pa) to the chip and record the meniscus receding position with a high speed camera (Hamamatsu ORCA-Flash 4.0) mounted on an inverted microscope (Olympus

IX81 ZDC). Fig.3.1(c) shows the channel cross-section by using AFM and fig.3.1(d) shows a typical nanopore array with 100 nm in diameter and with 25 nanopores.

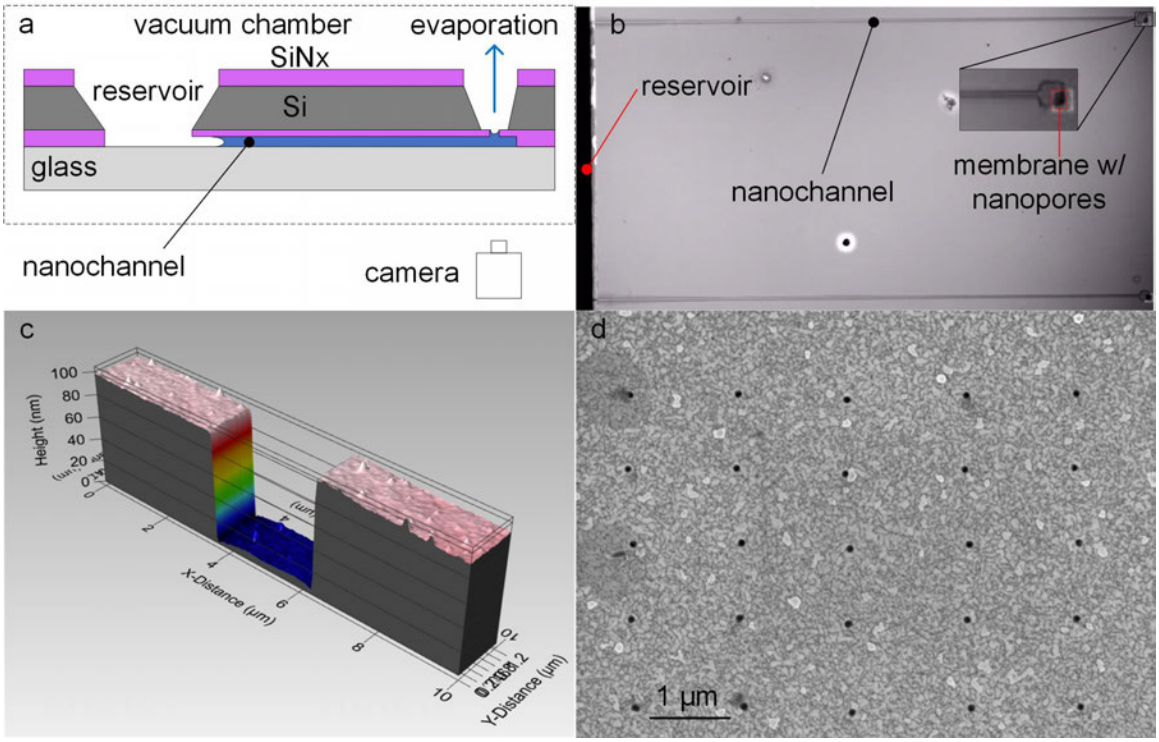


**Figure 3.1:** (a) Schematic of the experiment setup. Water enters into the nanochannel through the reservoir and exits the channel through the nanopores by evaporation. During the experiment, the vacuum chamber pumps down the chamber to 350 - 1400 Pa. (b) A snapshot of the meniscus receding process recorded by a high speed camera. (c) The AFM image of the nanochannel cross section. (d) The SEM image of the nanopores drilled by FIB on to the silicon nitride membrane. The scale bar is 1 $\mu$m.

Fig.3.2(a) shows the instance of water meniscus receded inside a nanochannel. Despite the pressure of the vacuum chamber varies from experiment to experiment, the pressure during one experiment is stable and the fluctuation is typically within 25 Pa, which is around 7% of the total pressure inside the vacuum chamber. Fig.3.2(b) depicts the instance when the water meniscus receded fur-

ther inside the nanochannel. It is note worthy that the water would always recede from the entrance. This is because we intentionally make the nanopore radius ($r = d/2$) smaller than the channel height ($h$) and the liquid pressure at the entrance ($P_e = P_{amb} - 2\sigma_l \cos\theta_c/h$) is larger than the liquid pressure at the nanopores ($P_n = P_{amb} - 4\sigma_l \cos\theta/d$). Fig.3.2(c) and (d) show the meniscus position versus time with open and closed channels, respectively. During the evaporation process, the vapor would exit through both the entrance and the nanopores for a open one. The equation to describe this process is:

$$\frac{dx}{dt} = D\frac{\rho_{v,n} - \rho_{v,\infty}}{x\rho_l} + v_r, \tag{3.1}$$

where $x$ is the location of the meniscus ($x = 0$ at the entrance), $D$ is the effective diffusion coefficient of water drying rate, $\rho_{v,n}$ and $\rho_{v,\infty}$ are the vapor density at the meniscus position and the ambient vapor density, $\rho_l$ is the liquid density, and $v_r$ is the meniscus receding speed in the nanochannel due to evaporation at the nanopore. To find the effective diffusion coefficient $D$ in eq.3.1, we perform a controlled experiment on the closed channels, where the meniscus receding curve can be modeled by:

$$\frac{dx}{dt} = D\frac{\rho_{v,n} - \rho_{v,\infty}}{x\rho_l} \tag{3.2}$$

Therefore, $D$ could be found by fitting the solution of eq.3.2 to the experiment curve as shown in fig.3.2(d). The solution is displayed as the blue-dashed curve. A second fitting is used to fit the solution of eq.3.1 in fig.3.2(c) as shown as the green-dashed curve. The slope of the red-dashed line would be $v_r$. We note that $D$ is on the order of $10^{-4}$ $\mathrm{m}^2/\mathrm{s}$ and is significantly larger than vapor diffusion coefficient in Knudsen regime ($10^{-5} \sim 10^{-6}$ $\mathrm{m}^2/\mathrm{s}$) as part of the liquid does not evaporate.

Instead, the liquid creeps through the channel corner and the process is detailed by Eijkel et al. (2005).

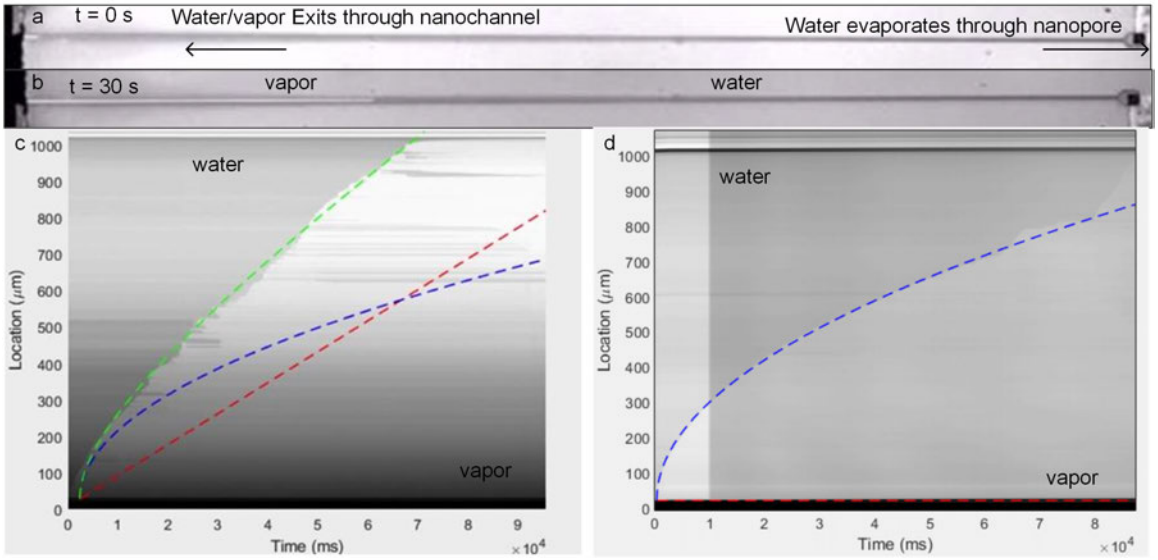


**Figure 3.2:** (a) The meniscus just enters the nanochannel from the reservoir. Meanwhile, water also exits the nanochannel through the nanopore. (b) At $t = 30$ s, the meniscus recedes further inside the nanochannel. The white part on the left side of the channel represents the vapor while the darker part on the right side represents water. (c) If we rotate fig.(a) and (b) counterclockwise and arrange each column in a chronological order in the horizontal axis, we can obtain fig.(c), where we can track the meniscus location with respect to time. Fig.(c) represents the receding curve for open channels. The blue dashed line is obtained by fitting fig.(d), where a separate experiment is done for a closed channel on the same chip. By subtracting the green dashed line with the blue dashed line, we obtain the red dashed-line, which represent the evaporation from nanopores.

## 3.3 RESULTS AND DISCUSSION

Assuming the meniscus is part of a sphere, the meniscus area could be estimated by:

$$A_m = \frac{\pi d^2}{2 + 2\sin\theta^*}, \tag{3.3}$$

where $\theta^*$ is the apparent contact angle at the nanopore during evaporation. The normalized meniscus area can then be computed by $A_m/A_{pore}$, where $A_{pore} = \pi r^2$. The apparent contact angle can be estimated at two time instances: (1) when the meniscus just enters the nanochannel, $\theta_1^*$ corresponds to the minimum value possible since the hydraulic resistance is the largest. (2) When the meniscus just enters the nanopore, $\theta_2^*$ corresponds to the maximum value possible since the hydraulic resistance is the smallest. A general equation for $\theta^*$ writes:

$$\theta^* = \cos^{-1}\left(\frac{d}{4\sigma_l}[v_r whR + \frac{2\sigma_l \cos\theta}{h}]\right), \tag{3.4}$$

as $\theta^* = \theta_1^*$,

$$R = R_t = \frac{12\mu l_c}{wh^3} + \frac{128\mu l_p}{\pi d^4 N} \tag{3.5}$$

$\theta^* = \theta_2^*$,

$$R = R_{pore} = \frac{128\mu l_p}{\pi d^4 N}, \tag{3.6}$$

where $\theta$ is the contact angle at the nanochannel entrance and is assumed to be 30°Li et al. (2019).

The measured evaporation velocity versus the total hydraulic resistance is plotted in fig.3.3 where the data is divided into three groups of nanopore diameter. From this figure, we can examine the data in three sections: 1. a $Rt$ smaller than $2 \times 10^{21}$ $[\mathbf{Pa/m^3/s}]$; 2. $2 \times 10^{21} < Rt < 4 \times 10^{21}$ $[\mathbf{Pa/m^3/s}]$; 3. $Rt > 7 \times 10^{21}$ $[\mathbf{Pa/m^3/s}]$. It is observed that there is no nanopore diameter dependence on the evaporation velocity in section 1 and 3 while the evaporation velocity increases with reducing the nanopore diameter in section 2. This is not completely consistent with the literature data from Li et al. (2019) (marked by red circles), which show that a smaller pore would always exhibit a higher evaporation velocity even

within section 1 and 3. On the other hand, we can see that at a given $Rt$, the data scatter almost up to two orders of magnitude. The data scattering issue will be further discussed in detail in Appendix A. Also, for nanopores with similar diameters, the evaporation velocity shows a slightly negative correlation with $Rt$.

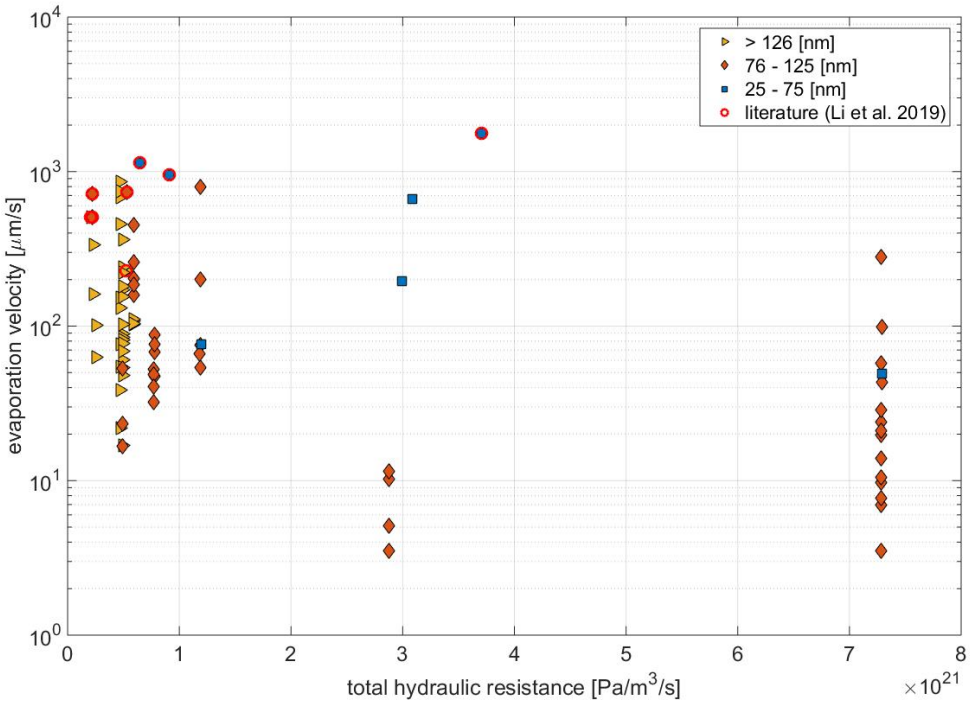


**Figure 3.3:** The measured evaporation velocity [um/s] versus the total hydraulic resistance.

Fig.3.4(a) shows the effect of the total hydraulic resistance on the normalized meniscus area. The blue dots correspond to $\theta^* = \theta_1^*$ and the red crosses correspond to $\theta^* = \theta_2^*$. There are two trends in this figure. First, since the meniscus is extended the most for $\theta_1^*$, it is expected that $A_{m1}/A_{pore}$ is larger than $A_{m2}/A_{pore}$. This trend is observed and most obvious as $R_t$ approaches $7 \times 10^{21}$. This validated our method of estimating the meniscus contact angle. On the other hand, both $A_{m1}/A_{pore}$ and $A_{m2}/A_{pore}$ increases as $R_t$ increases. This trend is a solid proof that one can tune

the meniscus area by changing the total hydraulic resistance of the nanochannel.

Fig.3.4(b) shows the effect of the hydraulic resistance on the normalized evaporation rate 1 $\sigma_{exp1}$& 2 $\sigma_{exp2}$. The normalized evaporation rate is obtained by:

$$\sigma_{\exp} = \frac{v_r wh}{N\pi r^2} \frac{1}{Q_{HKS}} \frac{A_{pore}}{A_{m,i}},\ i = 1, 2, \tag{3.7}$$

$$Q_{HKS} = \frac{2\sigma}{2-\sigma} \sqrt{\frac{M}{2\pi R_g}} (\frac{P_{eqm}}{\sqrt{T_i^l}} - \frac{P_v}{\sqrt{T_i^v}}), \tag{3.8}$$

where $\sigma = 1$ is the accommodation coefficient, $M$ is the molar weight, $R_g$ is the gas constant, $P_{eqm}$ is the equilibrium vapor pressure at the interface, $P_v$ is the partial vapor pressure, $T_i^l$ is the liquid temperature at the meniscus, and $T_i^v$ is the vapor temperature just above the meniscus. In this study, we assume that $T_i^l = T_i^v$, $P_{eqm} = P_{sat}$, and $P_v = P_{amb}$ by following Li et al.Li et al. (2019). We discovered that there is a mildly negative correlation between $\sigma_{exp1\&2}$ and $R_t$.

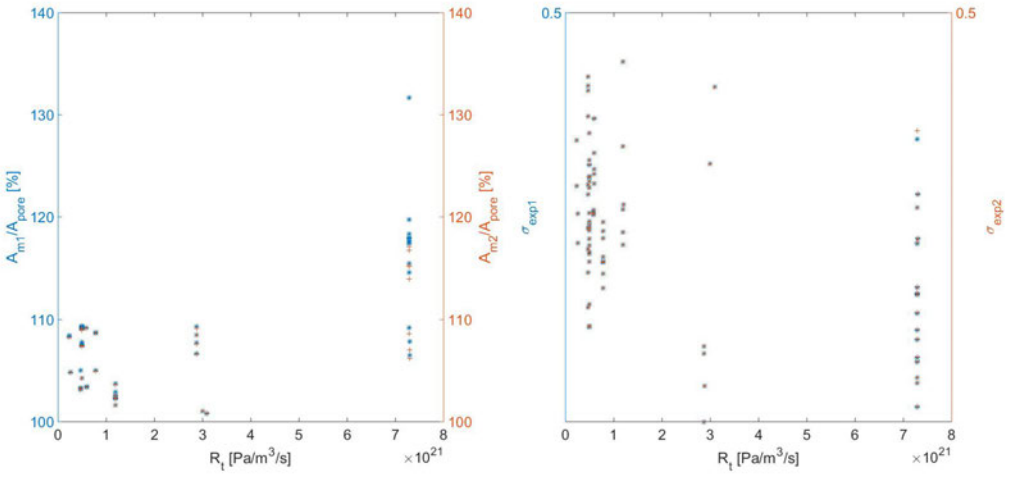


**Figure 3.4:** (a) The total hydraulic resistance ($R_t$) versus the normalized meniscus area for $\theta_1^*$ ($A_{m1}/A_{pore}$, blue symbol) and $\theta_2^*$ ($A_{m2}/A_{pore}$, red symbol). $\theta_1^*$ corresponds to the case when the meniscus just enters the nanochannel while $\theta_2^*$ corresponds to the case when the meniscus just enters the nanopores. We observe that the normalized meniscus area increases monotonically as the total hydraulic resistance increases, independent of $\theta_1^*$ and $\theta_2^*$. (b) The total hydraulic resistance ($R_t$) versus the normalized evaporation rate for $\theta_1^*$ and $\theta_2^*$. The vertical axis is in log scale. We found that the normalized evaporation rate decreases mildly as the total hydraulic resistance increases.

To understand the trend, we plot $\sigma_{exp1}$ against $A_{m1}/A_{pore}$ in fig.3.5 and the result is astonishing. $\sigma_{exp2}$ is discarded since the magnitude is similar to $\sigma_{exp1}$ and the behavior is the same. Fig.3.5(a) shows all the data collected in this study and divided the data into three sections: nanopore diameter ranging from 25 - 75 nm are shown in blue crosses, nanopore diameter ranging from 76 - 125 nm are shown in red Xes, and nanopore diameter ranging from 126 - 175 nm are shown in yellow circles. We found that $\sigma_{exp1}$ monotonically decreases as $A_{m1}/A_{pore}$ increases, independent of the pore diameter. This indicates that as the meniscus becomes more extended into the nanopore, the evaporation rate decreases at a given working condition.

This is in contrary to the main trend where researchers tend to believe the opposite is true Narayanan et al. (2011); Pati et al. (2013); John et al. (2021). A correlation between the effective accommodation coefficient due to the curved meniscus and the porosity effect is provided by John et al. John et al. (2021):

$$\begin{aligned}\sigma_{eff} = \phi\times(&-0.012S'^3 + 0.057S'^2\sigma + 0.018S'^2h - 0.06S'^2 \\ &- 0.448S'\sigma^2 + 0.028S'\sigma h + 0.208S'\sigma \\ &+ 0.009S'h^2 - 0.113S'h + 0.325S' + 0.071\sigma^3 \\ &- 0.046\sigma^2 h + 0.211\sigma^2 + 0.109\sigma h^2 \\ &- 0.45\sigma h + 0.933\sigma - 0.08h^3 + 0.158h^2 \\ &+ 0.113h - 0.29),\end{aligned} \tag{3.9}$$

where $\phi = 1$ is the porosity of the nanopores, $S' = A_m/A_{pore}$, and $\sigma$ is the accommodation coefficient. The prediction of eq.3.9 are shown in fig.3.5 as black solid lines, where three $\sigma$ are used. For $\sigma = 1$, the theory predicts that the evaporation mass flux is independent of how the meniscus is curved. This is in line with Lu et al.Lu et al. (2015). However, as $\sigma$ decreases, the theory predicts that the evaporation mass flux from nanopores should increase as the meniscus is curved. Fig.3.5 corresponds to nanopore diameter ranging from 25 - 75 nm, nanopore diameter ranging from 76 - 125 nm, and nanopore diameter ranging from 126 - 175 nm, respectively. By comparing the theory and the prediction, it is clear that the vapor kinetics does not play a major role since the two trends are contradictory with each other.

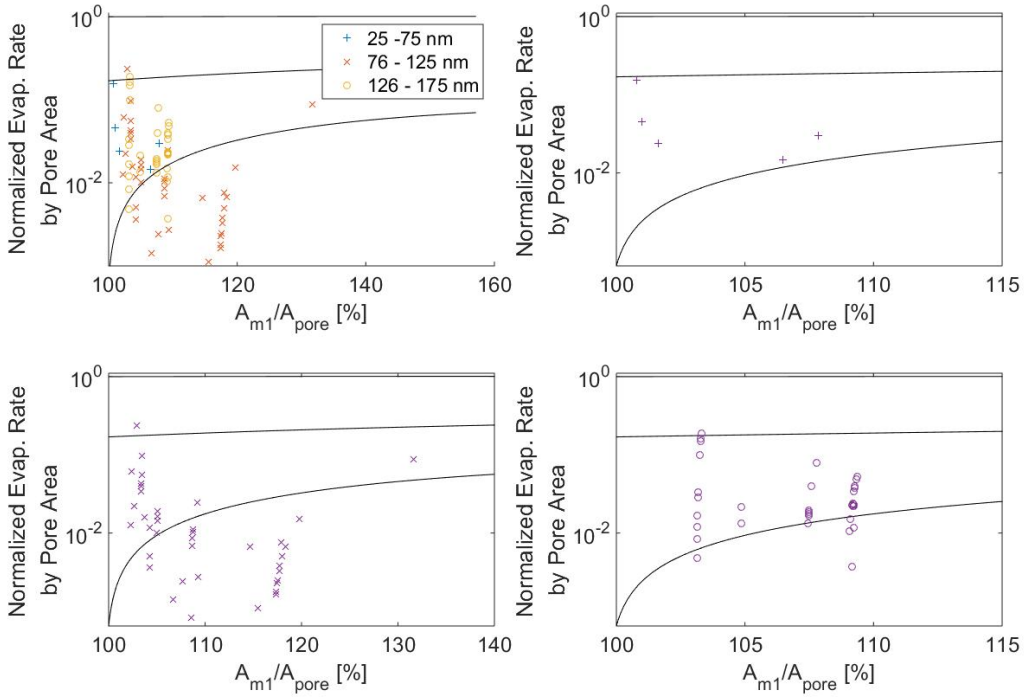


**Figure 3.5:** Effect of the meniscus area vs. the normalized evaporation rate by pore area.

To find the true evaporation coefficient, we normalize the evaporation rate by the estimated meniscus area and the results are plotted in Fig.3.6. The inset figure shows the estimated heat flux versus the normalized area. The figure clearly shows that as normalized area increases, both the heat flux and the true evaporation coefficient decreases monotonically. This implies that the chance of a vapor molecule getting reflected by the meniscus increases as normalized area increases. Thus, the question is: what could possibly slow down the evaporation rate from nanopores under vacuum?

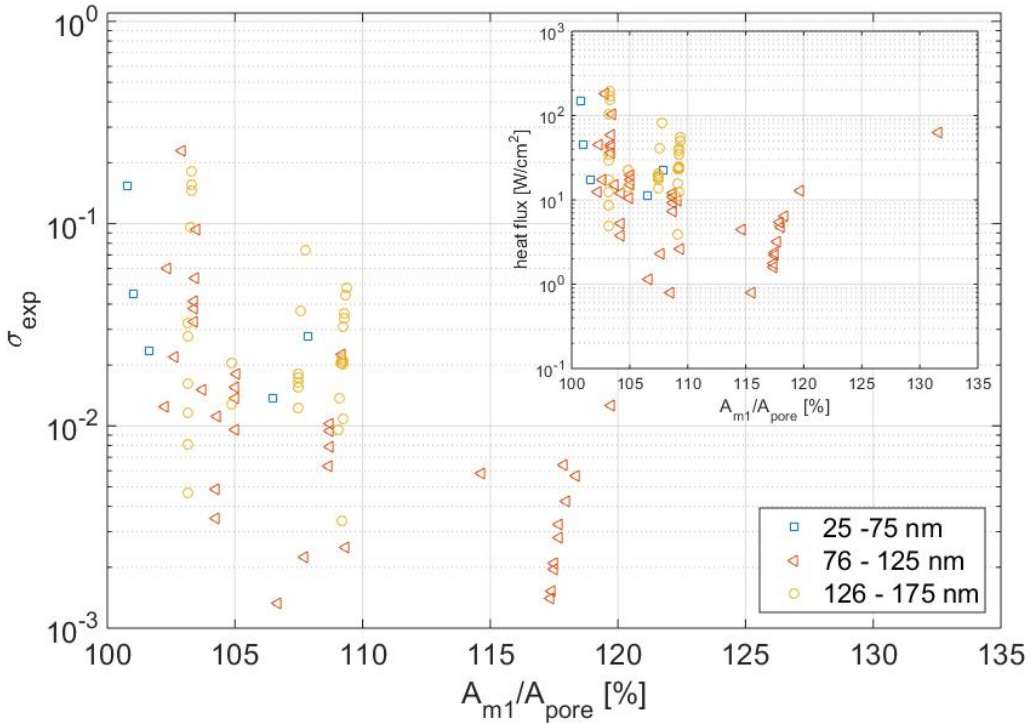


**Figure 3.6:** We plot the normalized meniscus area ($A_{m1}/A_{pore}$) versus the normalized evaporation rate ($\sigma_{exp}$) and the inset figure is the estimated heat flux.

One potential hypothesis to explain the above data set is that the negative pressure of the liquid increases the strength of the H-bonds and reduce the evaporation rate. Pointed out by Pálinkás et al. (1984) in fig.3.7(a), the probability of finding a certain numbers of H-bonds reduces as the pressure increases from natural pressure (NP) to high pressure (HP). In addition, Seyfi et al. (2017) concluded that *"Changes in hydrogen-bonds certainly affect water evaporation. Reinforced hydrogen-bonds prevent the evaporation of water, while weakened hydrogen bonds will increase water evaporation."* As a result, a higher liquid pressure results in a weaker H-bond network because the number of H-bonds decreases, leading to a higher evaporation flux. Based on this rational, it is reasonable to hypothesize that when the liquid

water is at higher negative pressure (corresponding to the more extended meniscus), the evaporation flux would decrease as the strength of the H-Bond network would increase and it becomes more difficult for water molecules to leave the liquid phase. However, To the best of my knowledge, no literature has published such results and a MD simulation could help us understand whether this hypothesis is true.

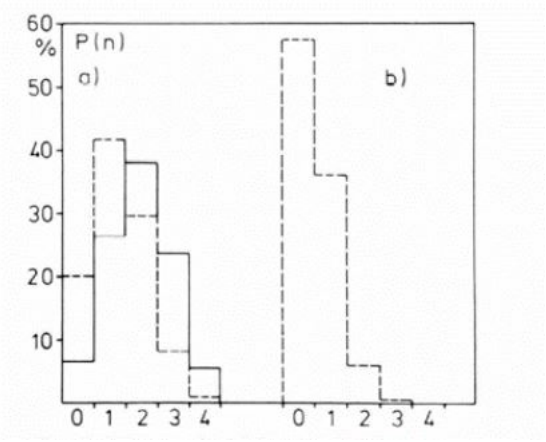


**Figure 3.7:** The probability of discovering the number of H-bonds formed simultaneously by water molecules, computed for the first four (a) and for the second four (b) neighbors. The solid line is for normal pressure water and the dashed line is for high pressure water Pálinkás et al. (1984)

.

Another potential mechanism is that the extended meniscus gives rise to different surface charge density at the liquid-vapor interface, which changes the orientation of water molecules at the interface and thus affects the evaporation flux. Published by Poli et al. (2020), the surface charge density at the bulk liquid interface for pure water (without protons and hydroxides) is -2.4 $[\mathbf{mC/m^2}]$. This negative charge originates from the orientation of the hydrogen bond network, leading to small amounts of charge transfer among it. Meanwhile, previous experimental evidences has shown that the orientation of the water molecules at the

interface plays a critical role in determining the evaporation rate Rana et al. (2022). As the nanopore surface itself is negatively charged, it is very likely that the surface charge density and the orientation of water molecules at the liquid-vapor interface for different extended menisci would be different from those at the bulk liquid-vapor interface. In fact, the more extended the meniscus, the stronger interaction between the pore surface and the liquid-vapor interface. Therefore, it is expected that there would be a larger change of the interfacial surface charge density for the more extended meniscus. To further validate this hypothesis, it is necessary to develop new measurement technique to measure the surface charge density and water molecule orientation at the nanopore liquid-vapor interface and/or conduct MD simulation that considers the charged pore surface and water molecule orientation.

In this chapter, we experimentally measured the kinetically-limited evaporation with various hydraulic resistances. After processing the experiment images, we found that: first, the evaporation data is scatter a lot and we proposed a novel MEMS device in Appendix A to improve the experiment accuracy. Also, we found that the evaporation coefficient decreases when the meniscus area increases. This trend is in contradictory to the DSMC simulation result and we further propose two possible mechanisms to try to explain the trend. More work is needed for the MD simulation teams to help us understand the root cause.

# CHAPTER 4

# Theoretical and experimental study of surface heating membrane distillation using novel membrane designs

## 4.1 PROJECT SUMMARY

A novel membrane covered with a thin porous heating layer and a thermal insulation layer is proposed to outperform the state-of-the-art surface heating membrane desalination device in terms of mass flux and heat utilization efficiency (HUE) in the literature. A 1D analysis is conducted to model the vapor transport and temperature distribution within the system. Four parameters are playing a key role: the thermal conductivity, porosity, and the thickness of the membrane, as well as the thermal conductivity coefficient of the insulation layer. The optimized mass flux and HUE is 152.63% and 28% higher than the state-of-the-art device, respectively. We believe our approach could potentially solve the water scarcity issue. We conducted the experiment with two types of membranes: the first one is a parlyene C membrane and the other one is the laser-reduced graphite oxide (LrGO) membrane. The purpose of using the parylene C membrane is to test a well-controlled micro-pore array membrane fabricated by the state-of-the-art MEMS technology. However, it cannot prevent liquid from penetrating and future research effort is needed to overcome this barrier. Furthermore, the fabrication process can only produce a porosity of 27.8%. This is too low compared to an ideal porosity of 74%. On the other hand, while the LrGO membrane successfully separates water and the wood insulation layer improves the SHMD performance, the measured mass flux is still only 33% of the state-of-the-art result Zuo et al. (2020). We believe this is probably due to the large thickness of the membrane (i.e., 100 $\mu m$). Future re-

search effort is needed to reduce this thickness while still being strong enough to withstand the laser process.

## 4.2 STATEMENT OF THE PROBLEM TO BE INVESTIGATED

Membrane desalination (MD) is one of the most promising technologies to resolve water scarcity issue occurring over the world with 1.8 billion people involved Dongare et al. (2017); Deshmukh et al. (2018). Similar to forward osmosis mentioned in the previous section, MD technology utilized a hydrophobic membrane to separate two bodies of water with low and high concentration. The feed side with high salinity is heated above room temperature to establish a temperature difference across the membrane. This temperature difference is the driving potential for evaporating water from the feed side and condensing desalinated water on the permeate side. However, traditional MD suffers from temperature polarization, which reduces the temperature gradient and leads to a lower vapor pressure and mass flux Politano et al. (2019). In addition, the average temperature gradient along the feed channel decreases with increasing the length of the feed channel, which imposed a limit on scaling up. Furthermore, heating the feed side outside of the membrane cell increases the system complexity and thermal losses through pipes. To address these issues, localized heating on the membrane either via solar or Joule heating had proven to increase the heat utilization efficiency (HUE) Shafieian & Khiadani (2019); Dudchenko et al. (2017); Politano et al. (2019). Specifically, the state-of-the-art device achieved a mass flux of 47.5 $[\mathbf{kg/m^2h}]$ with a HUE of 50% per single pass. Yet, the device is far from optimized performance nor scalability. Thus, the goal of this study is to propose several novel designs to break the record of the mass flux and HUE both theoretically and experimentally.

## 4.3 BACKGROUND

Surface heating membrane desalination could be achieved by two modes - solar or Joule heating. Solarthermal membranes absorb sunlight as the energy source while electrothermal MD induce heating through an electrically conducting coating. However, the heated plane in solarthermal membrane cells is not at the plane where evaporation happens Dongare et al. (2019). In addition, as the heated plane is in direct contact with fluid flow, additional heat loss caused by conduction through the solar absorbing material and convection through fluids lead to a lower HUE. On the other hand, with the advanced MEMS fabrication technologies available nowadays, we can directly deposit a layer of thin metal film or other electrical conducting material at the evaporating plane. In this fashion, the heat resistance from the source to the meniscus is minimized and the temperature gradient is maximized Dudchenko et al. (2017). However, electrochemical stability limit the power input and hence the water flux Zuo et al. (2020), and electrothermal SHMD membranes are required to possess the following features: (1) high electrical conductivity (2) well-insulated from the surrounding saline water (3) high porosity (4) low thermal conductivity and (5) scalability. These characteristics lead a novel hBN coating on a stainless-steel wire cloth combined with a commercial hydrophobic PVDF membrane succeeded in demonstrating the best performance so far. Despite this sensational breakthrough, our group believe with some improvement of the design and proper selection of the membrane material could lead to a better performance. The design rational is presented in the next section.

## 4.4 RESEARCH DESIGN AND METHODS

### 4.4.1 Theoretical analysis

The first proposed membrane design is shown in fig.4.1 to optimize the performance of SHMD, where the wood side is exposed to the feed flow. A thin layer of parylene C is used to isolate the conducting metal film Al with the saline solution. The vapor gap is formed inside the thickest parylene C layer at the very bottom of the structure.

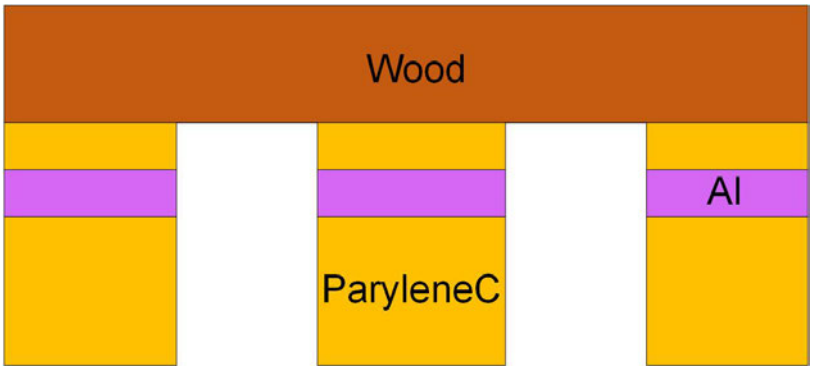


**Figure 4.1:** SHMD design.

The average mass flux across the membrane $J$ is written as $J = \epsilon M_w N_w$, where $M_w$ is the molar mass of water, $\epsilon$ is the porosity of the membrane, and $N_w$ is the net molar water flux across a pore. The maximum evaporation rate across a pore ($N_w$) on the feed and permeate sides is

$$N_w = \frac{S_F - S_P}{\Sigma R}, \tag{4.1}$$

where $S_F$, $S_P$ represent the theoretical maximum vapor transport rate for feed side and permeate side, respectively, and $\Sigma R$ is the sum of vapor transport resistances Lee & Karnik (2010); Lee et al. (2014). $S_F$ and $S_P$ could be determined from the

Hertz equation $S_j = p_j^e/\sqrt{2\pi M_w R_g T_j}$ for $j = R, F$, where $p_j^e$, $R_g$, $T_j$, is the equilibrium vapor pressure, the universal gas constant, and temperature at the vapor-liquid interface, respectively. Eq.4.1 can thus be simplified as

$$S_F - S_P \sim \frac{p_F^e - p_R^e}{\sqrt{2\pi M_w R_g \bar{T}}}, \tag{4.2}$$

where $\bar{T} = (T_F + T_R)/2$. It is shown that the result does not lead to a significant difference (<5%) over the 20-80 **[degC]** in this work by using the mean temperature Deshmukh et al. (2018). The equilibrium vapor pressure for sea water is given by experimental correlations

$$\ln P_{v,sw}/p_{v,w} = -4.5818e^{-4}S - 2.0443e^{-6}S^2, \tag{4.3}$$

where $S$ is the sea water salinity in **g/kg**, $\ln p_{v,w} = a_1/T + a_2 + a_3 T + a_4 T^2 + a_5 T^3 + a_6 \ln T$, $a_1 = -5800$, $a_2 = 1.3915$, $a_3 = -4.864e^{-2}$, $a_4 = 4.1765e^{-5}$, $a_5 = -1.4452e^{-8}$, $a_6 = 6.546$ Nayar et al. (2016). The total vapor transport resistance $\Sigma R$ is the sum of the transport resistance ($R_t$) and the interfacial resistances ($R_i$). The interfacial resistances is given as $R_i = (1 - \hat{\sigma})/\hat{\sigma}$, where $\hat{\sigma}$ is the accommodation factor. The physical meaning of this factor is that this is the fraction of the vapor molecules condense onto the bulk liquid versus the total vapor molecules approach the meniscus. Thus, $1 - \hat{\sigma}$ portion of the vapor molecules reflect back and do not condense. The transport resistance is given by

$$R_t = \frac{1}{\eta_{eff}} = \frac{(1 - p_0/p_t)\bar{v_w} l}{4 D_{wa}} + \frac{1}{\eta}, \tag{4.4}$$

where $\eta_{eff}$ is the effective vapor transmission probability, $p_0$ is the partial vapor

pressure, $p_t$ is the total pressure, $\bar{v_w}$ is the mean molecular speed of water vapor and equals to $\sqrt{8R_g\bar{T}/\pi M_w}$ Carey (2020), $l$ is the thickness of the air gap, namely, the hydrophobic membrane thickness, $D_{wa}$ is the effective vapor diffusion coefficient in air, which is given by $D_{wa} = 1.87e^{-10}\bar{T}/p_t$, $\eta$ is the vapor transmission probability in the Knudsen regime.

$$\eta = 1 + \frac{L^2}{4} - \frac{L}{4}(L^2+4)^{0.5} - \frac{[(8-L^2)(L^2+4)^{0.5} + L^3 - 16]^2}{72L(L^2+4)^{0.5} - 288\ln(L+L^2+2) + 288\ln 2} \tag{4.5}$$

Combining the above equations, the mass flux across the membrane reads

$$J = \epsilon\sqrt{\frac{M_w}{2\pi R_g\bar{T}}}[\frac{(1-p_0/p_t)\bar{v_w}l}{4D_{wa}} + \frac{1}{\eta} + 2\frac{1-\hat{\sigma}}{\hat{\sigma}}]^{-1}(p_F^e - p_R^e), \tag{4.6}$$

by assuming the accommodation factor at both sides of the membrane equal to each other.

The heat flux across the membrane ($q$) is composed of two parts - conduction through the membrane with an effective thermal conductivity of ($k_m$) and the latent heat ($h_{fg}$) associated with phase change across the membrane. The heat flux could be modeled as

$$q = \frac{k_m}{l}(T_{F,m} - T_{P,m}) + Jh_{fg}, \tag{4.7}$$

where $T_{F,m}$ is the liquid temperature at the feed side on the membrane, $T_{P.m}$ is the liquid temperature at the permeate side on the membrane. $k_m = \epsilon k_g + (1-\epsilon)k_m$, where $k_g$ is the thermal conductivity of gas, and $k_m$ is the thermal conductivity of the membrane. Conserving energy from the membrane heating surface to the feed liquid, we have

$$h_f(T_{F,i} - T_{F,b}) + JC_p(T_{F,m} - T_{F,b}) + q = q_s, \tag{4.8}$$

$$h_f(T_{F,i} - T_{T_{F,b}}) = K_i(T_{F,m} - T_{F,i}) \tag{4.9}$$

where $h_f$ is the heat transfer coefficient of the feed side fluid, $C_p$ is the heat capacity of water, $q_s$ is the input heat flux, $K_i$ is the thermal conductivity coefficient ($K_i = k_i/l_i$) of the insulation layer,$k_i$ is the thermal conductivity of the insulation layer, $l_i$ is the thickness of the insulation layer, $T_{F,i}$ and $T_{F,b}$ is the temperature at the interface between the membrane and the wood insulator and the bulk feed fluid temperature, respectively. On the other hand, energy conservation on the permeate side reads

$$T_{P,m} = T_{P,b} + \frac{q}{h_p + JC_p}, \tag{4.10}$$

where $h_p$ is the heat transfer coefficient of the permeate side fluid. The equations above form a systems of equations to solve for $T_{F,m}$, $T_{P,m}$, $q$, and $J$.

The second design focused on the scalability of the fabrication process. Instead of using expensive MEMS fabrication technology to make the sample with well defined geometry and straight pores, we collaborated with MIT The Grossman Group to develop a conductive laser-reduced graphene oxide (LrGO) membrane Straub et al. (2021). The only equation changed from the above analysis is eq.4.6 to be:

$$J = B(p_F^e - p_R^e), \tag{4.11}$$

where $B$ is the membrane permeability coefficient. For a system operating under normal pressure, $Kn < 0.01$, $B$ is found by Khayet (2011):

$$B = \frac{\pi}{RT}\frac{P_t D_i}{P_a}\frac{r^2}{\tau\delta}, \tag{4.12}$$

where $P_t$ is the total pressure inside the pore, $D_i$ is the vapor diffusivity, $P_a = P_t - P_l$

is the air pressure inside the pore, $P_l$ is the saturation vapor pressure inside the pore, $r$ the pore radius, $\tau$ the tortuosity of the membrane and $\delta$ is the membrane thickness. Since a lot of the membrane parameter is missing (not provided by the collaborator), $B$ serves as a fitting factor to match the experiment data with the theory.

### 4.4.2 Design rational

Four key design parameters play a key role in determining the performance of an SHMD membrane - the thermal conductivity of the membrane $k_m$, the porosity of the membrane $\epsilon$, the pore radius $r$, and the thermal conductivity coefficient of the insulation layer $K_i$.

Fig.4.2 shows the effect of thermal conductivity on the water flux across the membrane with different membrane thicknesses. From the figure, we can observe two trends. The first one is with a lower $k_m$, the mass flux increases at given a membrane thickness. Thus, polymer-based membrane material is suitable for membrane desalination as their thermal conductivity is on the order of 0.1 **W/mK**. We chose perylene C as the membrane material as it features the lowest thermal conductivity while being easy to process by MEMS technology on a wafer scale Liu et al. (2018). On the other hand, carbon black materials and commercial AAO membranes have a thermal conductivity of 2 **W/mK** Chen & Li (2020). As the membrane thickness increases, the mass flux first increases and then decreases for $k_m = 0.2$ (blue dots), and features an optimum value at a thickness around 1000 $\mu$**m**. This is due to the competition between the thermal gradient and the vapor transport resistance across the membrane. A thicker membrane results in a larger thermal gradient while the vapor transport resistance becomes higher, and vice

versa. A suitable range for the membrane is therefore between 10 to 100 $\mu\mathbf{m}$ while it is hard to manufacture membranes above 100 $\mu\mathbf{m}$ based on current MEMS fabrication technology. Notice that the state-of-the-art performance (red line) is well below the estimated mass flux of $\sim$100 $\mathbf{kg/m^2h}$.

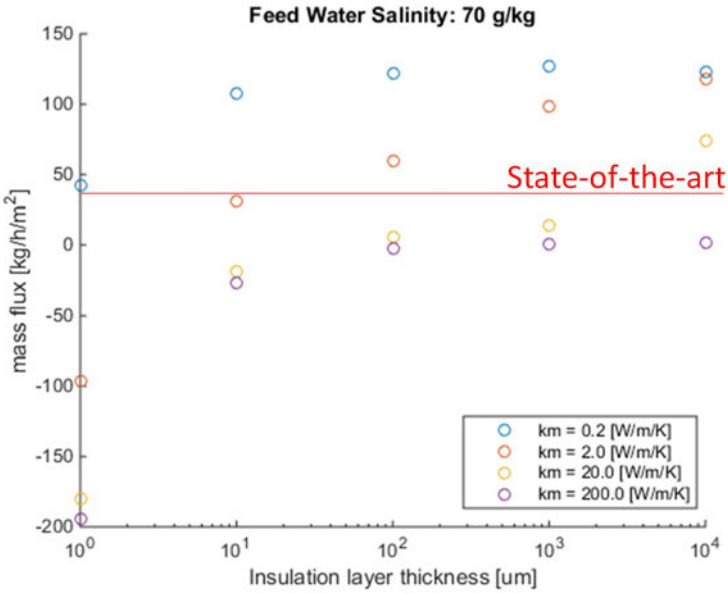


**Figure 4.2:** membrane thickness versus mass flux across the membrane with different membrane thermal conductivity.

The second most important parameter is the membrane porosity $\epsilon$, and the effect of porosity on the mass flux with different membrane thicknesses is shown in fig.4.3. In the selected membrane thickness ranging from 10 to 100 $\mu m$, only the membrane with a porosity of 0.74 could outperform the state-of-the-art device by nearly three times.

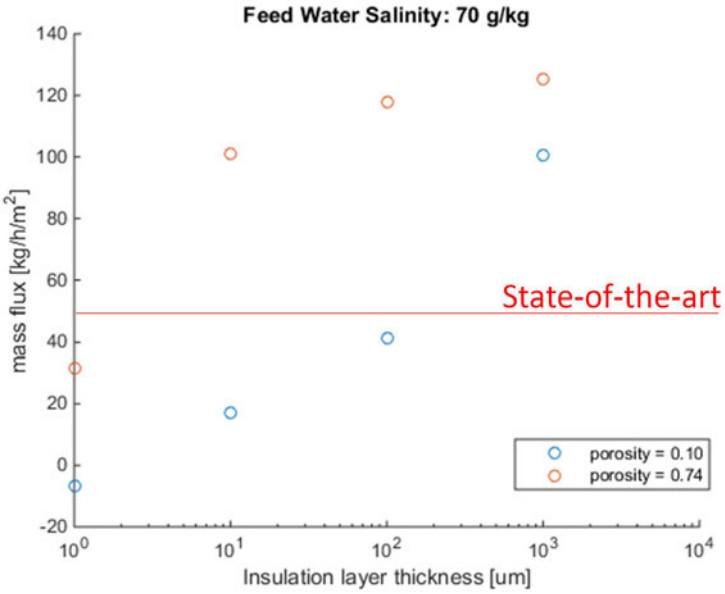


**Figure 4.3:** Membrane thickness versus mass flux with different membrane porosity.

The effect of pore diameter is shown in fig.4.4. It is observed that a larger pore radius could lead to better performance between a membrane thickness of 10 to 100 $\mu m$. However, it is reported in the literature that larger pores are vulnerable to water penetrating into the air gap regime. Thus, the upper bound of the pore radius is not yet determined. Further experiments are required to determine this limit given a working condition.

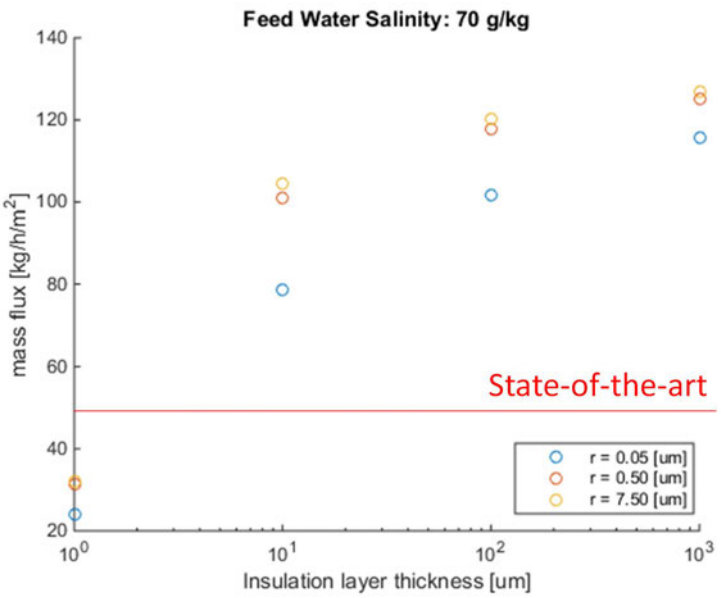


**Figure 4.4:** Membrane thickness versus mass flux with different pore radius.

Finally, the effect of the thermal conductivity coefficient is shown in fig.4.5. It is clear that a lower $K_i$ results in a higher mass flux. Wood is selected as the insulation layer as it is permeable with a low thermal conductivity ($\sim$0.2.) Liu et al. (2017). Furthermore, with a $K_i = 40$, the $HUE_{sp}$, which is the heat utilization efficiency per single pass could be increased to 73%, which is shown in fig.4.6.

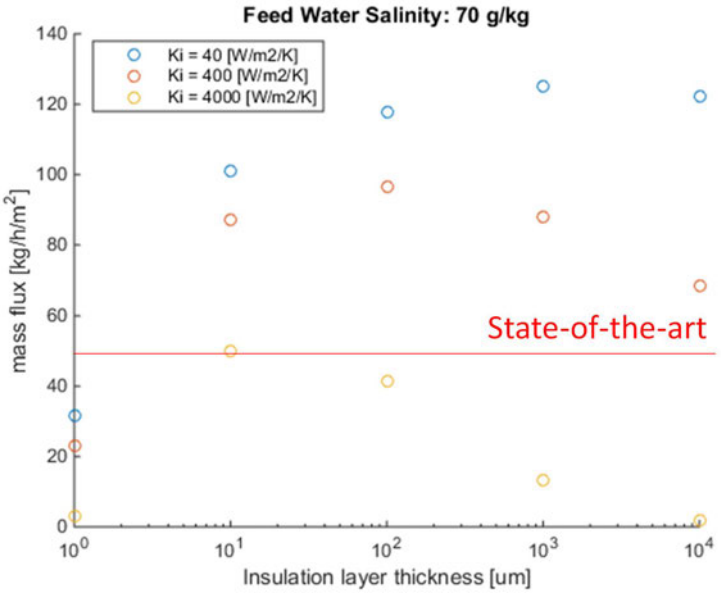


**Figure 4.5:** The effect of the thermal conductivity coefficient on the mass flux at various membrane thickness.

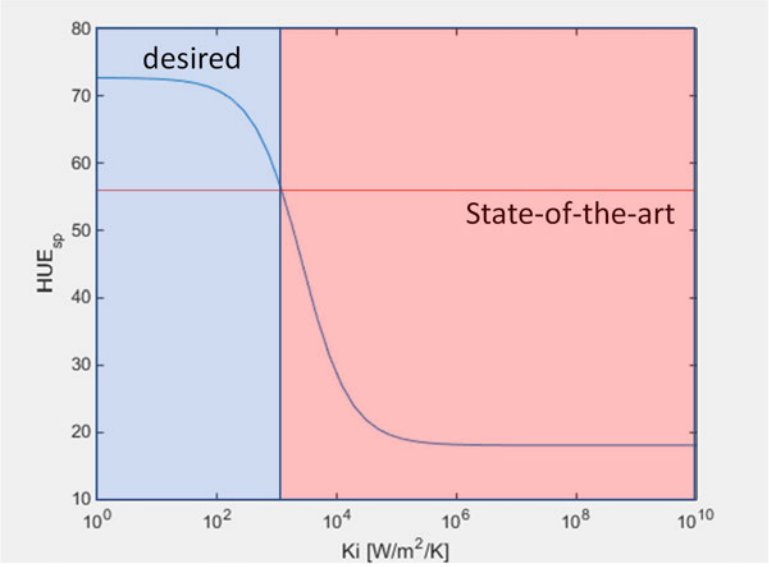


**Figure 4.6:** $K_i$ versus $HUE_{sp}$

In sum, based on the 1D analysis, an optimized mass flux of 120 $\mathbf{kg/m^2h}$ has been demonstrated to be feasible given that the membrane is made of parylene C with a thermal conductivity of 0.2, a thickness of 10-100 $\mu\mathbf{m}$, a porosity of 0.74,

a pore radius around 7.5 $\mu\mathbf{m}$, and with a wood insulation layer with a thermal conductivity coefficient of 40 $\mathbf{W/m^2K}$. The estimated mass flux and $HUE_{sp}$ is 152.63% and 28% higher than the state-of-the-art device.

### 4.4.3 Experiment setup

In addition to the modeling effort, we have also built an SHMD setup and tested two types of membranes: PKU pareylene sample with well-defined geometry, but low porosity and relatively high fabrication cost; idea system to compare with theoretical results; MIT LrGO sample, scalable fabrication, good wetting control, less control on membrane properties. The schematic of the experiment setup is shown in fig.4.8 and in fig.4.7. The system consists of two water loops: the feed water loop containing saline water to be desalinated and the permeate water loop containing pure water. The saline water is pumped from pump 1 into the membrane desalination cell. The volume flow rate of both permeate and feed side are set at 25 **mL/min** by using two Masterflex L/s models. Then, we applied a AC voltage to heat up the conductive layer on the membrane. As the membrane is heated up, it evaporates water from the feed side. The vapor transport to the other side of the membrane and condenses into the permeate side. The mass flux evaporated from the feed side to the permeate side could be obtained as

$$\dot{m}'' = \frac{m(t=0) - m(t=end)}{\Delta t} \frac{1}{\epsilon A_t}, \tag{4.13}$$

where $A_t$ is the total area of the membrane. The rest of the feed side water has been heated up and needed to be chilled back to room temperature. We did this by placing the tubes into a chiller, which can dissipate 10 W of heat flow. This cooling power is more than enough because the power input to the membrane is

typically less than 5 W. On the other hand, the pure water exits the membrane cell and enters the balance and returns to pump 2.

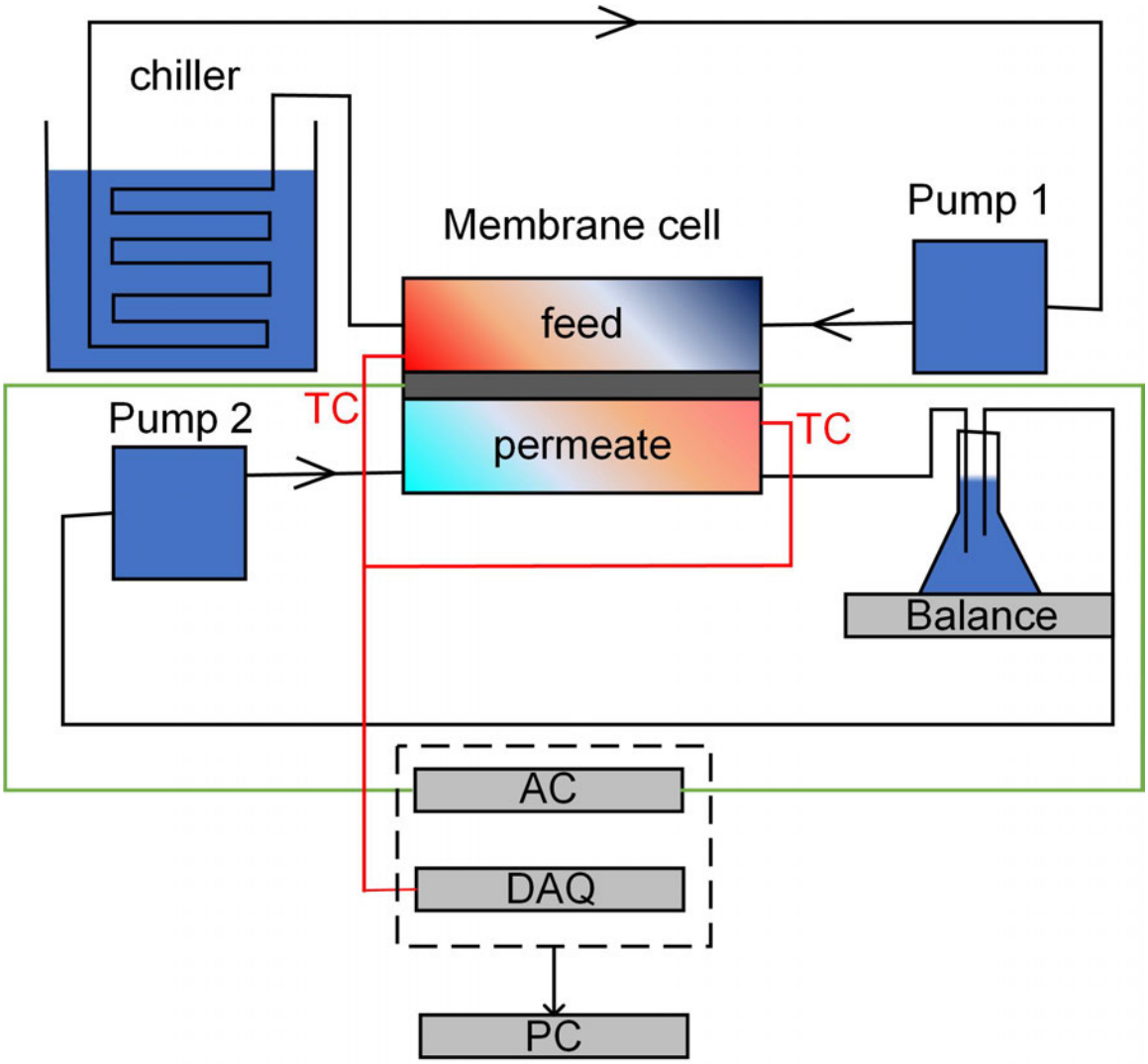


**Figure 4.7:** Catroon of the experiment setup.

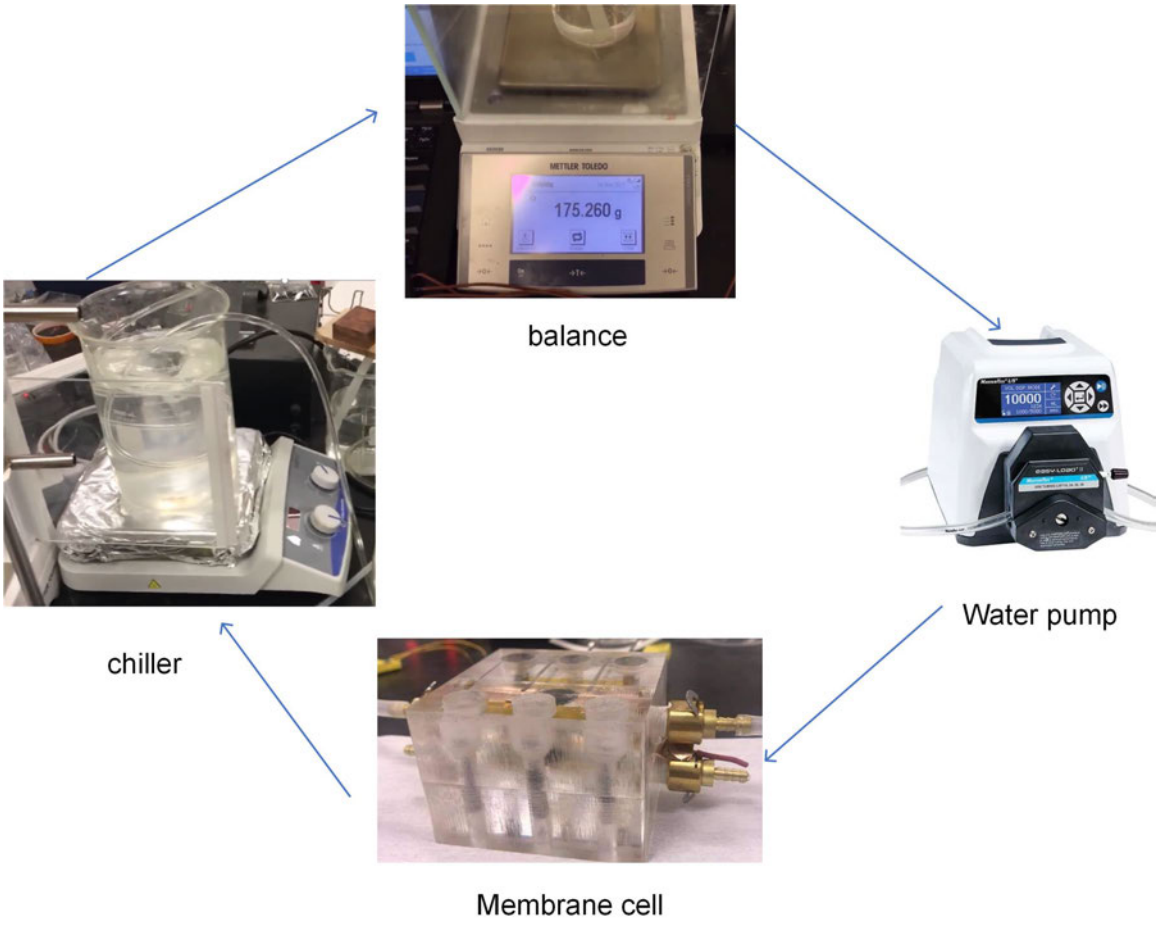


**Figure 4.8:** Images of the experiment setup.

### 4.4.4 Uncertainty analysis

The relative uncertainty of this measurement method could be quantified as:

$$\frac{\delta \dot{m}''}{\Delta \dot{m}''} = \sqrt{(\frac{dm}{\Delta m})^2 + (\frac{dA}{A})^2 + (\frac{dt}{\Delta t})^2}, \tag{4.14}$$

$dm$ is 0.001 **g**, $dA = 0.05e-3 * (1.855e-2 + 0.2e-2)\ m^2$ and $dt$ is 1 **min**. Since the membrane area $A = 4.8e-5\ m^2$, the time scale for the measurement is 3 hours, the dominating uncertainty comes from the mass measurement. However, with the high precision of the mass balance, the maximum uncertainty is 1.73% in this

study.

## 4.5 RESULTS AND DISCUSSION

### 4.5.1 Parylene C membrane characterization

The parylene C membrane is fabricated at the Peking University and are termed as the PKU samples here after Liu et al. (2018). We prepared three thicknesses of the membrane with different pore sizes and porosities shown as the below table:

| Thickness [$\mu$m] | pore radius [$\mu$m] | porosity [%] |
|---|---|---|
| 24 | 4 | 12.8 |
| 17 | 4.5 | 27.8 |
| 10 | 5 | 27.6 |

**Table 4.1:** PKU sample parameters

The SEM image of the samples:

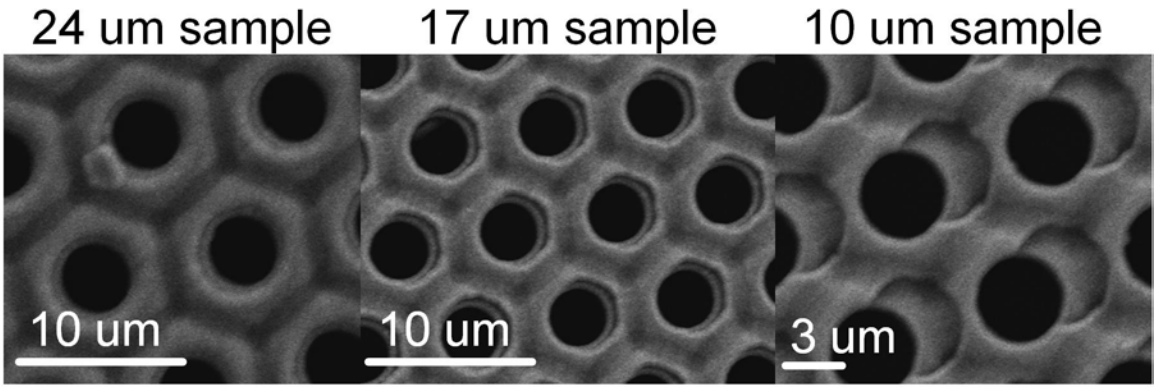


**Figure 4.9:** PKU sample SEM

We conducted heating experiments in air to figure out what is the maximum power that can be applied to the membrane before burning it. For a 24 $\mu$m sample, the maximum power that can be applied is 4.5 **W** and the maximum temperature

on the sample reaches 240 °C, which is recorded by a IR camera. Note that the temperature distribution is quite uniform.

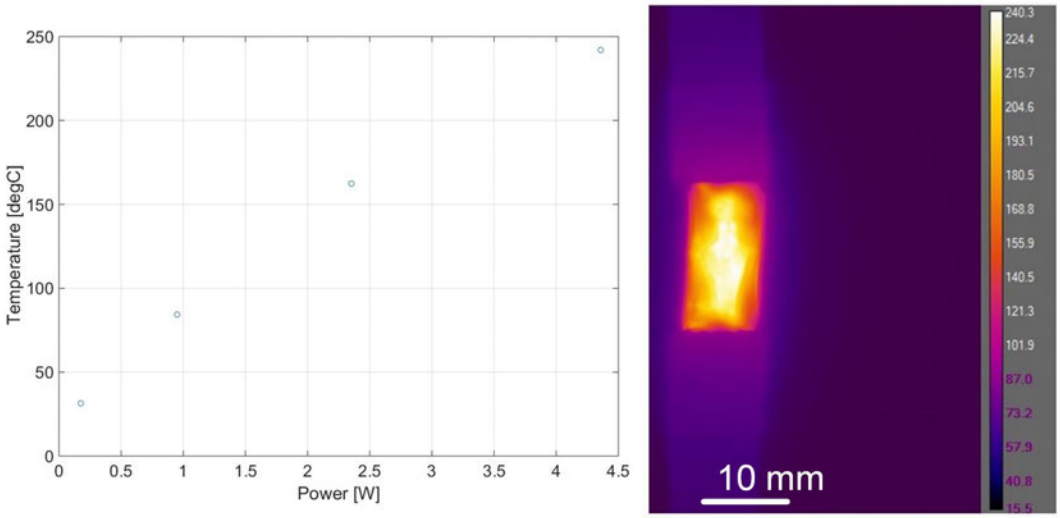


**Figure 4.10:** (left) power versus temperature, (right) PKU 24 $\mu$m IR image at maximum power.

For a 10 $\mu$m sample, the maximum power is 1.6 **W** and there is a local hot spot on the sample with a temperature up to 350 °C, making it an non-ideal membrane. The reason that the mass flux is low is that the membrane is poorly designed: first, the hydrophobic layer has a nominal thickness of 100 $\mu$m. Typical membranes for SHMD applications have a thickness of 25 $\mu$m. Another reason is that the pore geometry is not straight. The vapor exiting the feed side would have to go through a twisted path before reaching the permeate side compared to a straight channel. This would induce more vapor transport resistance and lower the heat and mass flux.

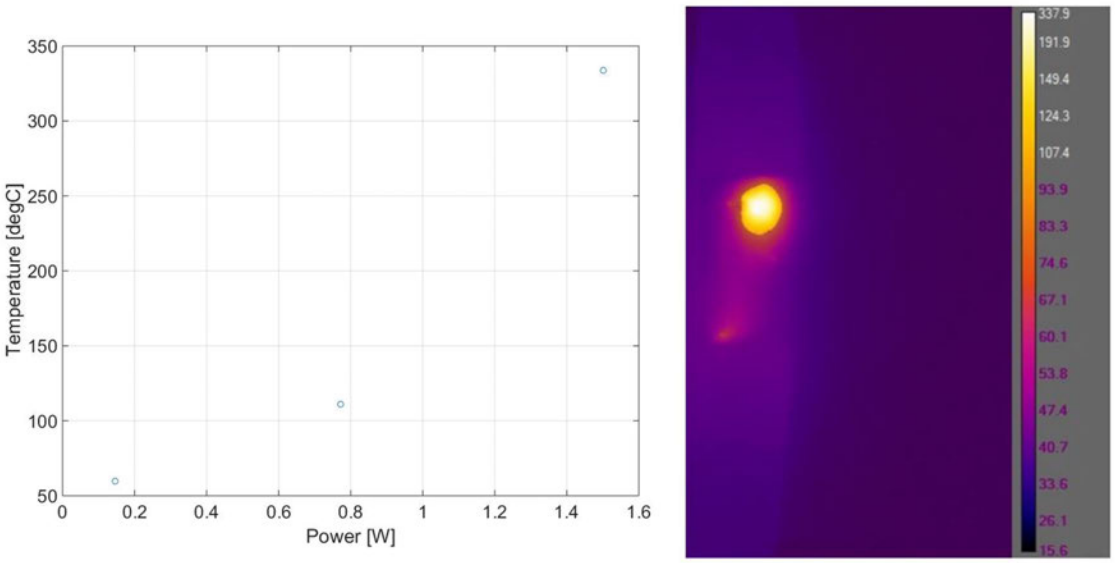


**Figure 4.11:** (left) power versus temperature, (right) PKU 10 $\mu$m IR image at maximum power.

Then, we did a dye diffusion test with Cary 60 UV-Vis to determine whether the membrane is water impermeable. One side has a dye concentration of $0.1$ **mM** while the other side is pure DI water, with the membrane separating both liquid bodies. Unfortunately, the dye penetrates into the DI water as shown in the below figure, where the concentration of the dye in the DI water side increases over time.

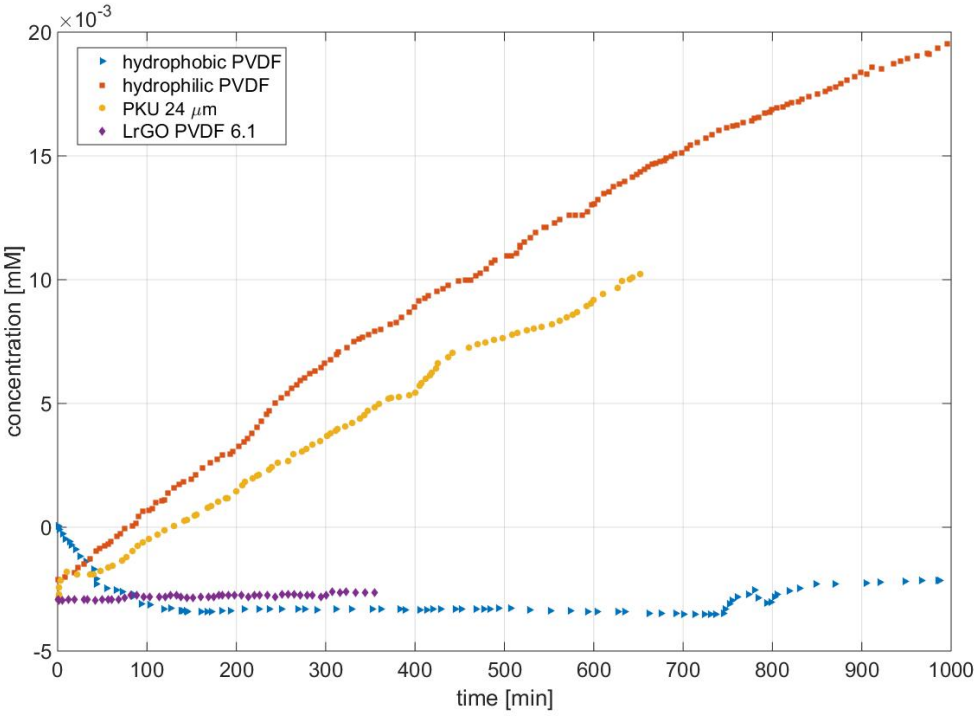


**Figure 4.12:** Time versus concentration of dye in the DI water side for various membranes: 1. a hydrophobic PVDF membrane represented by blue triangle; 2. a hydrophilic PVDF membrane represented by red squares; 3. a PKU 24 $\mu$m sample represented by yellow dots; 4. a LrGO membrane represented by purple diamonds.

This result indicated the water would penetrate through the membrane during the SHMD experiment, yet, we tried to put this membrane to the membrane desalination cell. Not surprisingly, we observe large amount of bubbles emerging from the membrane indicating that the water permeate through the membrane and we stopped progressing in this direction.

### 4.5.2 LrGO membrane characterization

Based on the experience we gained for the PKU samples, the first experiment we conducted on the LrGO samples is the dye diffusion test and the result is shown

in fig.4.12.

This result is exciting since this membrane is working. Then, we conducted several experiments to decide which experimental configuration would lead to the best performance i.e. should we use silver paste (The silver paste is typically used to make sure good contact between two conductive parts to reduce the electrical resistance)? should we use the edge part of the sample or the center part of the sample? What is the maximum power that the sample can hold?

Fig.4.13 shows the effect of silver paste on the LrGO membrane. We observe from the figure that the sample with silver paste has a steady power output at 1 **W** and the temperature reaches 45 °C while the power decays steadily for the sample w/o silver paste and the temperature only reaches 35 °C. Thus, silver paste is required.

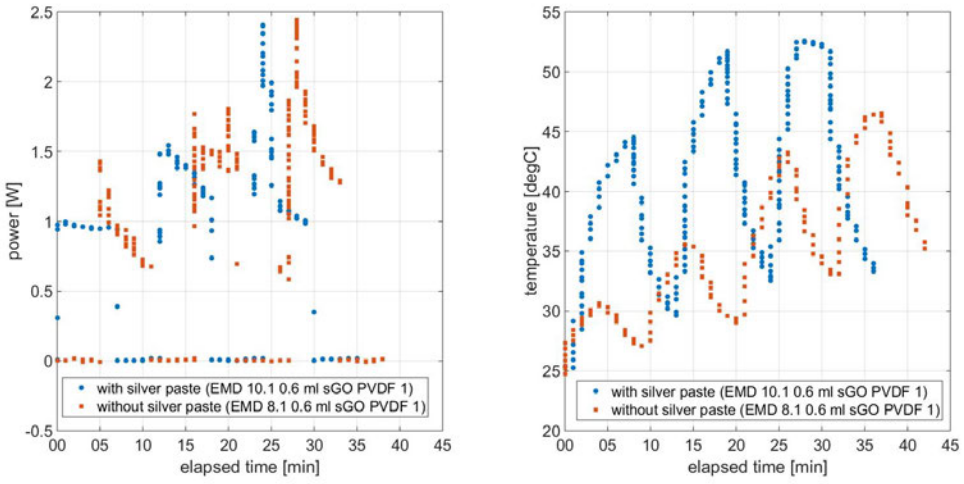


**Figure 4.13:** The effect of silver paste on the power and temperature response of the LrGO membrane. (left) power. (right) temperature.

Next, we test the effect of edge/center sample:

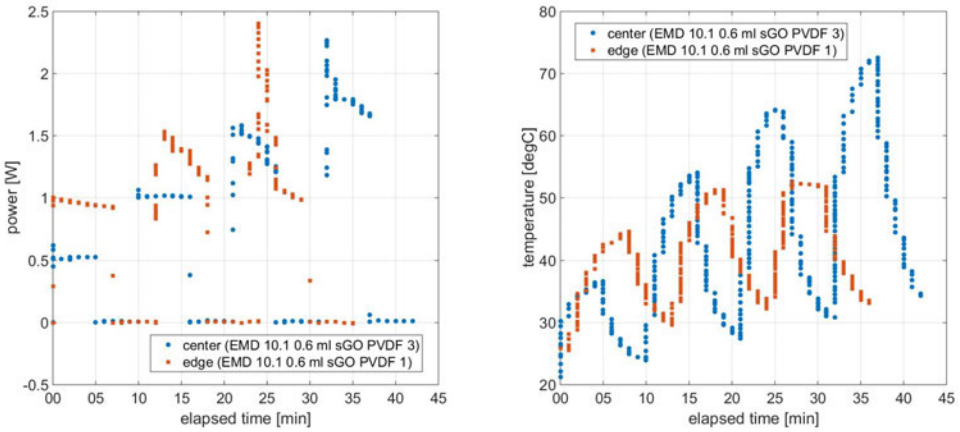


**Figure 4.14:** The effect of edge/center on the power and temperature response of the LrGO membrane. (left) power. (right) temperature.

While the power starts to decay at 1.5 **W** for both samples,the center sample has a higher temperature response at 1 **W**. PVDF became black means that the polymer/LrGO is burned and cannot be further tested. A higher temperature response means that the maximum mass flux could potentially be higher. Thus, we concluded that center sample with silver paste is suitable for the experiment.

After these tests, we found the the PVDF membrane became black as shown in fig.4.15.

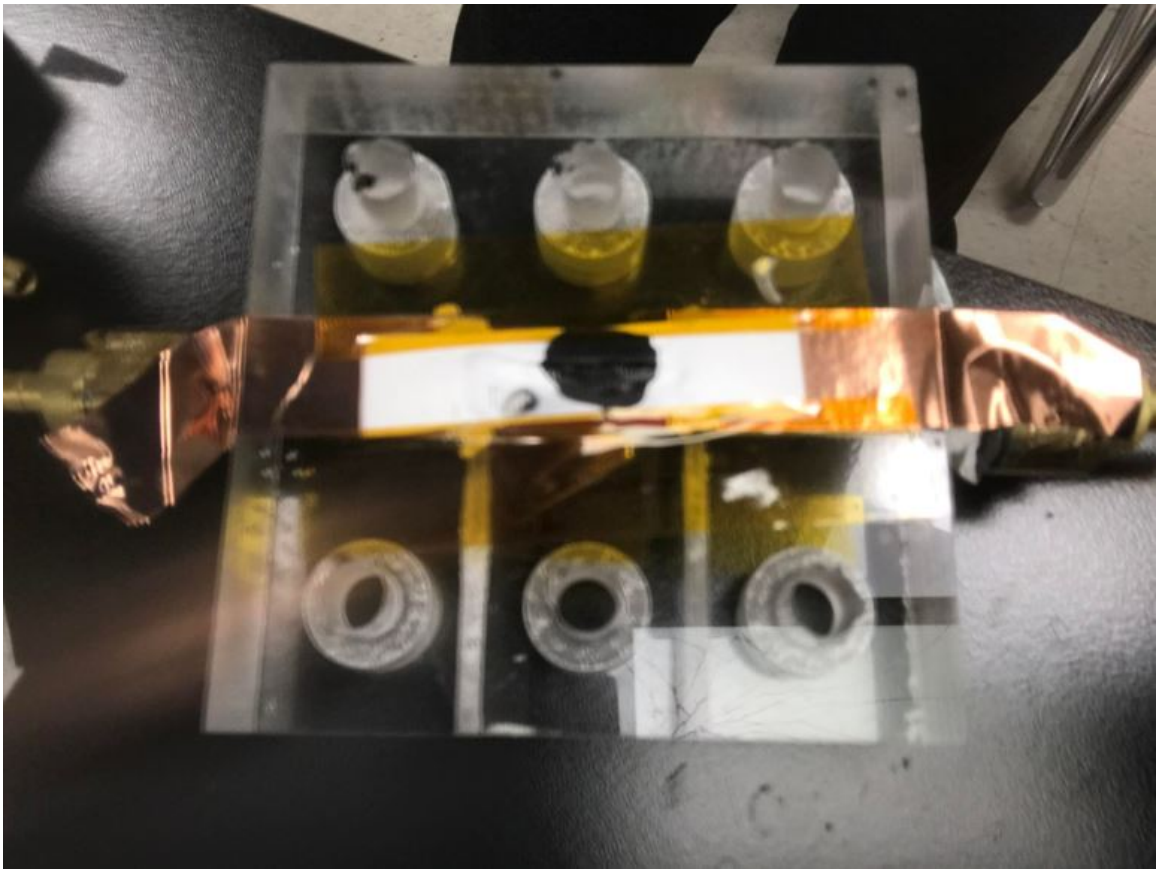

**Figure 4.15:** Burned PVDF sample after the experiment.

Therefore, we researched for membrane candidates:

| Name | Melting point (degC) | Thickness (um) | Pore size (um) | Porosity | Diameter (mm) | Notes |
|---|---|---|---|---|---|---|
| PVDF | 177 | 65-160 | 0.22 – 1 | N/A | N/A | |
| PTFE | 327 | N/A | 0.2 – 5 | N/A | 90 | |
| Glass fiber | 550-1135 | 254 – 1270 | 0.5 – 1 | N/A | 37-293 | Need to modify to hydrophobic |

**Figure 4.16:** Membrane candidates.

Based on Table.4.16, PTFE has a higher melting point than PVDF with similar pore sizes and is a hydrophobic membrane. Also, it is commercially available. Thus, we decide to test this material. The result is shown in fig.4.17.

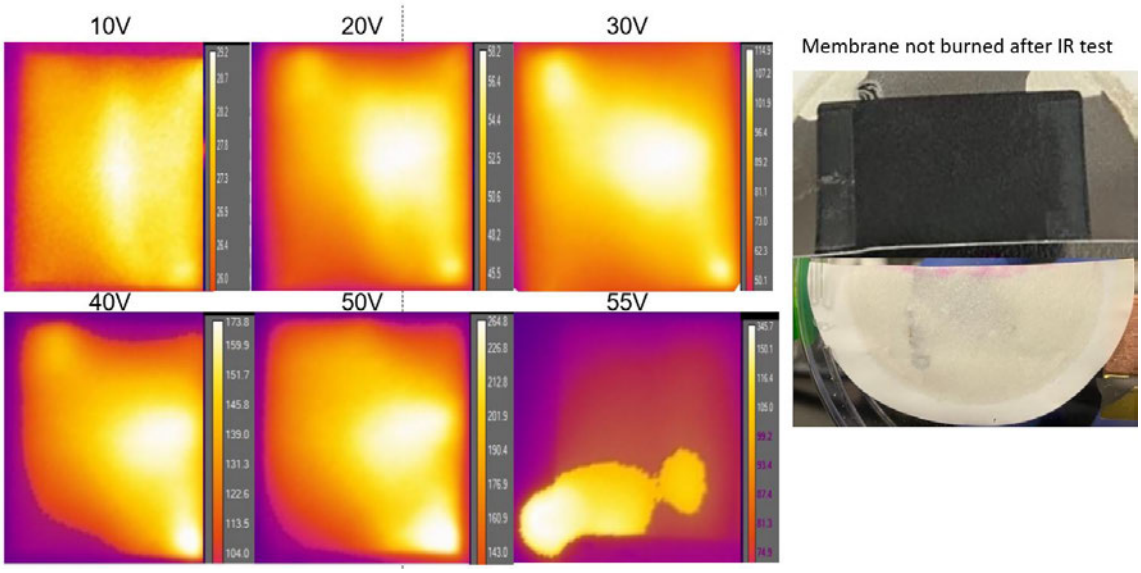


**Figure 4.17:** PTFE dry test with IR camera.

We observe that the PTFE membrane does not burn even with a maximum temperature of 345 °C. Then, we tested the membrane performance as shown in fig.4.18.

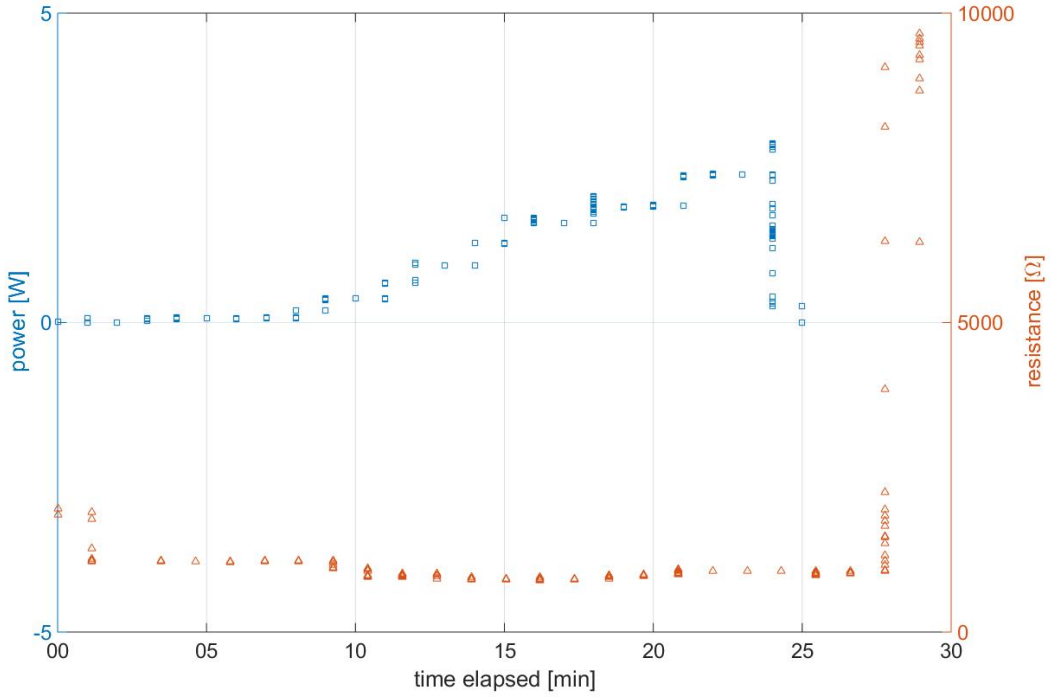


**Figure 4.18:** PTFE membrane power response in air.

From this figure, the PTFE power is stable at 2.4 **W**, which is much better than the PVDF, which starts to decay at 1.5 **W**. Thus, we proceed with the PTFE membrane to conduct the water desalination test.

### 4.5.3 LrGO PTFE membrane desalination result

The results are summarized in fig.4.19. The orange dots in the figure shows the state-of-the-art experiment result from the literature using 100 **g/L** NaCl solution. The blue dots represent LrGO PTFE membrane with DI water. The grey dots are for 70 **g/L** NaCl solution. By comparing the literature data (max 42 $[\mathbf{kg/m^2/h}]$ with the grey dots (max 8 $[\mathbf{kg/m^2/h}]$), we found our experiment data shows two outliers with extremely high $\mathbf{HUE_{sp}}$. The two data on the top is considered as outliers

because the value are way higher than the pure water case, which does not make sense at all. The outliers may due to bad contact between the LrGO and the copper tape during the assembly procedure. The relative poor performance of the LrGO membrane may be caused by a thick PVDF membrane (100 $\mu$m) compared to 25 $\mu$m of what the literature data used. Another possible reason is that the porosity of the membrane is too low so the vapor cannot pass through the membrane easily. If we want to improve the performance, a thinner membrane with higher porosity should be tested.

Finally, the yellow dot represents 70 **g/L** NaCl solution with 3 **mm** wood membrane. It demonstrates a 129% increase in performance and proves that the thermal insulation layer concept works.

Using the measured water flux to solve for the membrane permeability coefficient, $B$, we found $B = 3.58e^{-8}$ $\mathbf{kg\ m^{-2}\ s^{-1}\ Pa^{-1}}$, which is two orders smaller than the literature value Zuo et al. (2020). In the future, methods to increase this value should be researched.

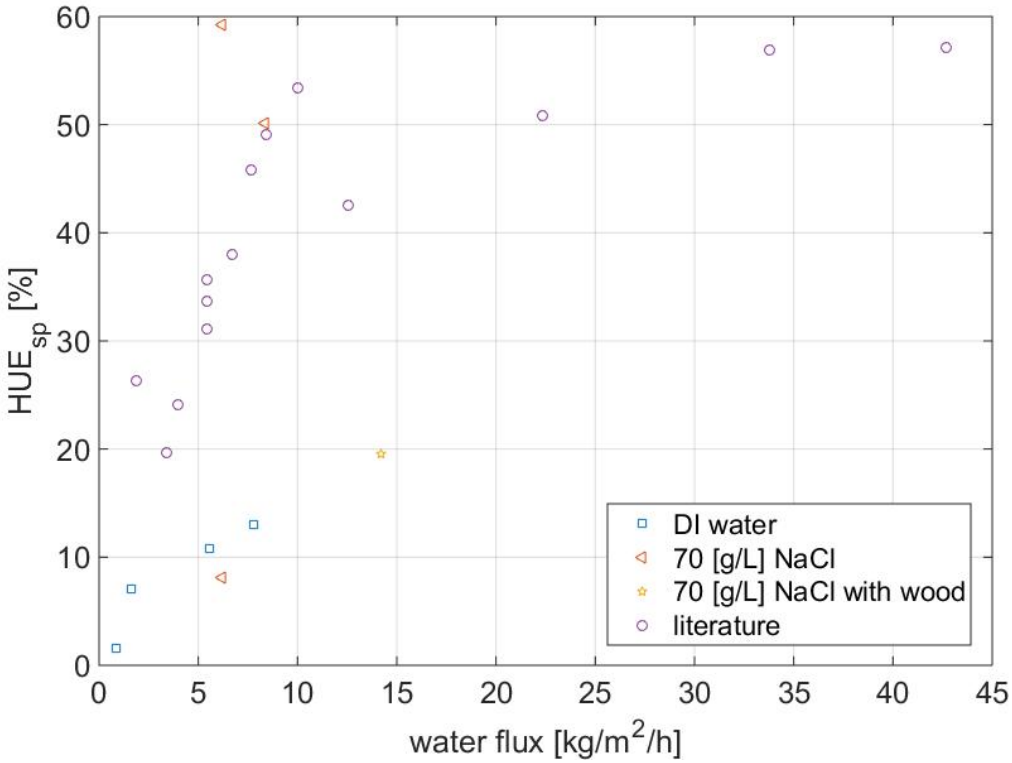


**Figure 4.19:** SHMD experiment result.

In sum, in this chapter, we conducted a 1D analysis for the SHMD system to model the effect of various parameters on the desalination mass flux and $HUE_{sp}$. To the best of our understanding, this is the first theoretical study for a SHMD membrane with an insulation layer. We found the promising membrane configuration to outperform the literature data. On the other hand, we explored the feasibility of our analysis by fabricating the proposed design (Parylene C and LrGO membrane) despite the Parylene C membrane did not work out eventually. We built the experiment setup from scratch and conducted very nice measurements with a relative uncertainty smaller than 2%. Finally, we tested the effectiveness of adding the designed insulation layer and it increases the mass flux by 129%.

# CHAPTER 5

## Conclusion

In conclusion, this thesis explored new fundamentals and applications of capillary evaporation from nanoporous membranes using both numerical and experimental methods. We first developed a semi-continuum numerical analysis to model the meniscus shape and evaporation rate for single nanopores with different confinement/surface properties under various working conditions. We found that increasing the surface charge densities on the pore wall and/or the liquid-vapor interface can significantly extend the meniscus and thus increase the mass flow rate per pore. Based on this rational, we then designed and fabricated a hybrid nanochannel-nanopore device to test whether extending the meniscus (by changing the total hydraulic resistance of the system) could increase the evaporation rate. However, the results show that a flat meniscus is the best configuration for nanoporous evaporators. We believe this is related to how the hydrogen bond change its' structure in confined space or under tremendous tension. Following this study, we tried to apply our understanding of evaporation to surface heating membrane distillation (SHMD) applications. We developed a 1D analysis to model vapor transport and temperature distribution across the SHMD system with an additional thermal insulation layer and investigated the effects of the insulation layer thermal properties and the membrane porosity on the distillation performance. We also experimentally tested two types of new surface heating porous membranes: one being the parlyene C membrane and the other being the LrGO membrane. The parlyene C membrane, despite the well-ordered pore structures, cannot prevent liquid from penetrating and future research effort is needed to overcome this barrier. In addition, the current fabrication process can only produce a porosity of

27.8%. This is too low compared to an ideal porosity of 74%. On the other hand, although the LrGO membrane can separate water and the addition of the wood insulation layer can indeed improve the SHMD performance, the achieved mass flux is still only 33% of the state-of-the-art result Zuo et al. (2020) probably due to the large thickness of the membrane (i.e., 100 $\mu m$). Future research effort is needed to reduce this thickness while still being strong enough to withstand the laser process. Finally, a new suspended nanopore evaporation measurement platform that can potentially solve the data scattering issue present in Chapter 3 by precisely measuring temperature change and heat flux due to nanopore evaporation is proposed.

# APPENDIX A

## Thoughts on improving the evaporation experiment

### A.1 STATEMENT OF THE PROBLEM TO BE INVESTIGATED

Measuring the performance of the kinetically-limited evaporation has been a heated topic for the last decade. While Lu et al. (2016, 2019); Hanks et al. (2018) measured the heat flux from an array of nanopores, Li et al. (2019, 2017); Xiao et al. (2022) focused on measuring the mass flux from nanoslits and nanopores. However, no approaches have been done for measuring the heat flux directly from small array of nanopores. Although the heat flux can be estimated by multiplying it by the latent heat, Tang et al. (2020); Lee et al. (2022); Lu et al. (2020) pointed out that the latent heat may reduce up to 50% as the water molecules change it's structure in nanoscale confinements. Thus, using the bulk latent heat value to estimate the heat flux from mass flux data would lead to an over-estimation of the performance. Furthermore, there are several challenges that the current hybrid nanochannel-nanopore device encounters. First of all, the data gathered from such device is ALWAYS scattering as shown in fig.3.6. Normally, a measurement method should not lead to more than 10% difference for a same sample. However, the extracted $\sigma_{exp}$ scatters from $10^{-1}$ to $10^{-3}$. The resolution of the measurement method is utterly unacceptable. There are two reasons that might contribute to this poor resolution: contamination in water and/or in the nanopore or temperature fluctuation during the experiment. On one hand, contaminants could cause blockage of nanopore and thus reduce the evaporation area. Contaminants could also directly result in significant reduction on evaporation coefficient Carey (2020). Li et al. (2019); Xiao et al. (2022) pointed out that once the nanopore is clean (checked

by SEM), it would be clean for all the subsequent tests. Moreover, based on the SEM data I gathered before and after those measurements, the pores are clean. Based on these observations, contaminant-induced nanopore blockage is unlikely the cause of the scatter data. To further verify this, one should conduct the experiment in an ESEM to monitor the pore profile during evaporation. Compared to the possibility of contaminant-induced nanopore blockage, contaminant-induced change of evaporation kinetics is more likely to be a cause of our experimental observation. However, the direct proof of contaminants affecting evaporation coefficient is harder to achieve. One possible way to do that is to integrate the current hybrid nanochannel-nanopore measurement setup with a high-sensitivity spectroscopy to measure and analyze contaminants during the nanopore evaporation experiment. Also, control experiments can be done by conducting the evaporation experiments in a cleanroom environment with minimum contaminants in the air. Moreover, researchers can use either piranha or oxygen plasma to better clean the hybrid nanochannel-nanopore devices before the evaporation experiment. Those new experiments can potentially determine the effect of contamination during the experiment.

On the other hand, it is possible there is a temperature change during the experiment and/or between the experiments. Despite Li et al. (2019); Xiao et al. (2022) claims the temperature does not change based on the simulation results, the temperature on the chip actually differs by 2 °C based on thermocouple measurements while the thermocouple location and attachment method is not clearly documented. Also, the temperature measurement raw data is not disclosed in the SI to justify this claim. Furthermore, the simulation only consists of one membrane on the chip while in reality, there are 50 membranes and two millimeter-scale wa-

ter reservoir on the chip that acts like heat sink (i.e. the simulation model does not represent the actual device). Thus, it is hardly convincing to me that the temperature of the chip will not change during the experiment. On top of these issues, another question arises when researchers attach thermocouples to the chip: would the device alter the evaporation dynamics?

In sum, given the fact that the current nanochannel-nanopore measurement technique failed to provide a direct heat flux measurement, failed to monitor the temperature of the nanopores without thermocouples, failed to provide consistent data among different devices and most importantly, failed to be a repeatable measurement even for a same sample, it is necessary to develop a robust platform to measure the temperature and heat flux for single nanopore evaporation experiment. Experiments based on this platform can tell us whether the temperature would lead to a fluctuated data or provide indirect proof that the contamination is the dominating mechanism.

## A.2 DEVICE DESIGN AND MEASUREMENT THEORY

### A.2.1 Overall strategy

Fig.A.1 shows the schematic of the designed structure to tackle the challenges listed above. This design is an innovation based on previous researches in measuring one-dimensional nanostructures (nanotubes, nanowires, and nanobelts) Shi et al..

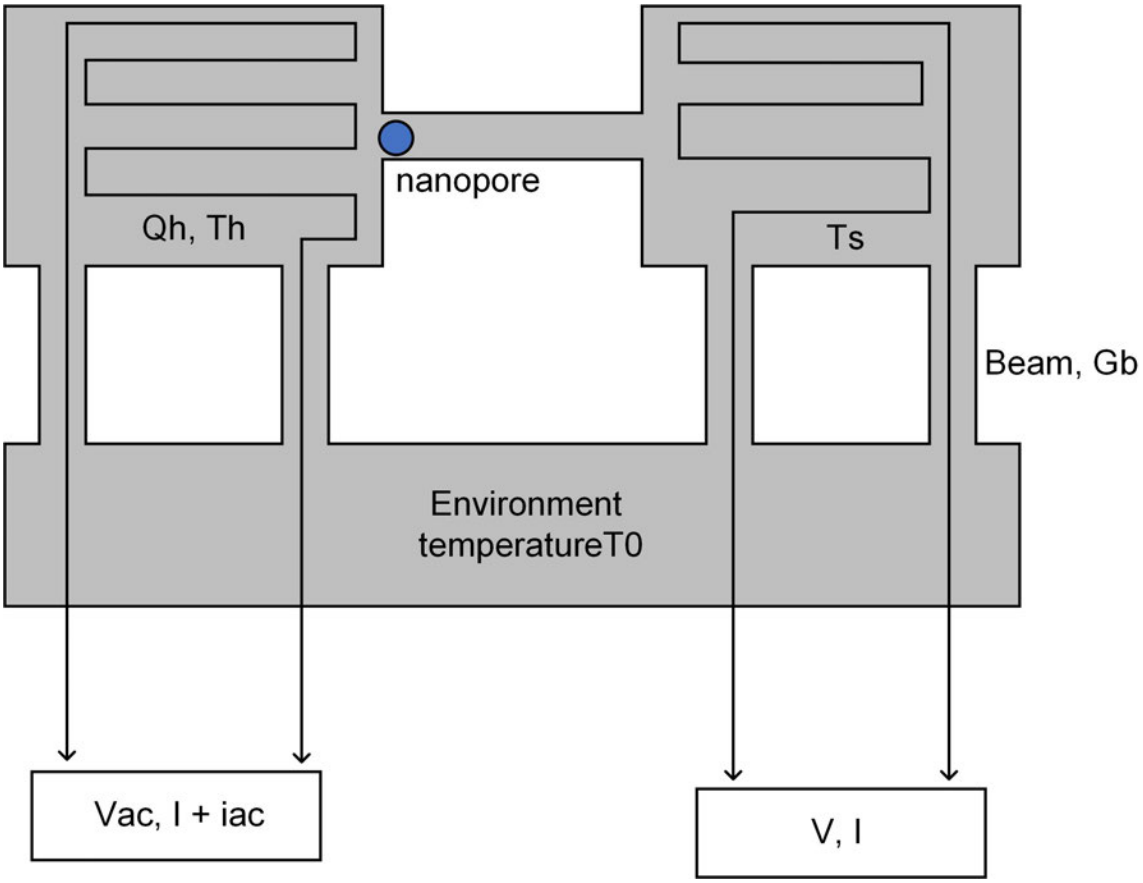


**Figure A.1:** Schematic of the designed experimental setup.

The device will be placed in a vacuum chamber with 200 Pa. The two suspended membrane are denoted as the heating membrane (left in fig.A.1) and the sensing membrane (right in fig.A.1), respectively. Current of magnitude ($I$) flows to the heating side wire having a resistance of $R_h$ and a joule heat of $Q_h = I^2 R_h$ is generated and the temperature of the heating membrane is raised to a uniform $T_h$. A portion of the heat generated is passed through the bridging channel to the sensing membrane ($Q_s$), raising it to a temperature of $T_s$. Part of $Q_s$ is dissipated by evaporation from the nanopores ($Q_e$) and the rest flows to the sensing membrane and then being dissipated to the environment via the beam ($Q_2$). Heat would also flow from the heating membrane to the environment via the beam ($Q_1$). Therefore,

we can obtain $Q_e$ by simply:

$$Q_e = (Q_h - Q_{loss}) - (Q_1 + Q_2), \tag{A.1}$$

where $Q_{loss}$ is the measurement error and will be discussed later. We find $Q_1$ and $Q_2$ by:

$$Q_1 = G_b(T_h - T_0) \equiv G_b \Delta T_h \tag{A.2}$$

$$Q_2 = G_b(T_s - T_0) \equiv G_b \Delta T_s, \tag{A.3}$$

where $G_b$ is the thermal conductance of the beam. To measure $G_b$ experimentally, we can use a device without nanopores and $Q_e$ becomes 0. Ignore the heat loss term for simplicity, Eq.A.1 becomes:

$$Q_h = Q_1 + Q_2 = G_b(\Delta T_h + \Delta T_s) \tag{A.4}$$

Thus,

$$G_b = \frac{Q_h}{\Delta T_h + \Delta T_s} \tag{A.5}$$

Hence, by measuring the temperature of the heating membrane ($T_h$) and sensing membrane ($T_s$), we can obtain $G_b$, $Q_1$, and $Q_2$. The temperature rise is monitored by the resistance change of the wires on both membranes (as a RTD) with two lock-in amplifiers. The detailed method is shown in the uncertainty analysis section. As for now, the important design goal is to make sure that in the operating temperature range of the heating membrane from 20 - 100°C, $Q_h$ is much larger than $Q_{loss} + Q_1 + Q_2$ to make a meaningful measurement. Otherwise, if $Q_h \sim Q_{loss} + Q_1 + Q_2$, then from eq.A.1, $Q_e$ might be smaller than the measurement sensitivity and all we got is system noise.

A thermal resistance network along with the beam cross-section is plotted in fig.A.2 to model the performance of the device.

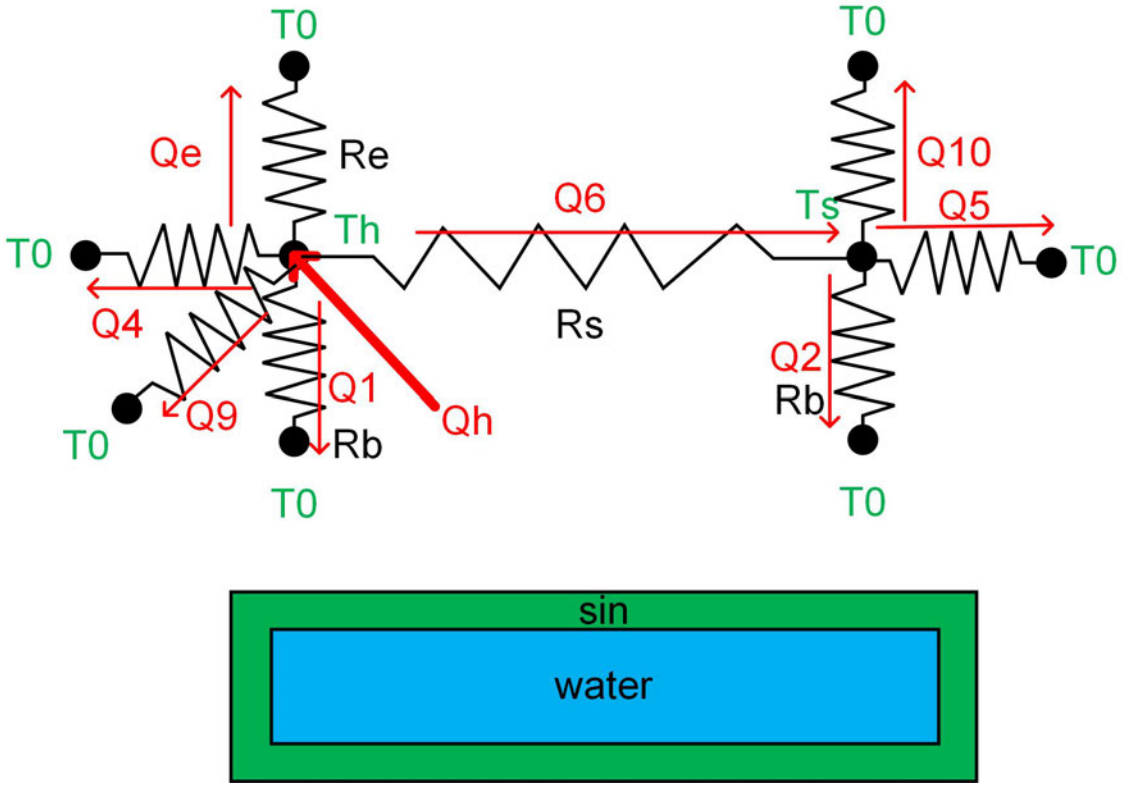


**Figure A.2:** Schematic of the thermal network and the cross-sectional view of the beam.

The nanopore is assumed to be at the same temperature as $T_h$ because the location is chosen to be right next to the heating membrane and the temperature gradient is assumed to be negligible. $R_e$ is the evaporation resistance:

$$R_e = \frac{1}{h_i A_p}, \tag{A.6}$$

where $A_p$ is the total area of the nanopore area,

$$h_i = \frac{2\sigma}{2-\sigma}\frac{h_{fg}^2}{T_h v_{lv}}\sqrt{\frac{M}{2\pi R T_h}}, \tag{A.7}$$

where $\sigma$ is the evaporation coefficient, $h_{fg}$ is the latent heat of evaporation, $v_{lv}$ is the specific volume of water, $M$ is the molar weight of water, $R$ is the gas constant.

The energy conservation at node $T_h$ is:

$$Q_h = Q_1 + Q_e + Q_4 + Q_6 + Q_9, \tag{A.8}$$

where $Q_4$ is the heat loss due to radiation from the heating membrane:

$$Q_4 = \sigma_r A_h \epsilon (T_h^4 - T_0^4), \tag{A.9}$$

$Q_9$ is the convective heat loss from the heating membrane:

$$Q_9 = h_v A_h (T_h - T_0), \tag{A.10}$$

where $h_v$ is the upper limit of heat transfer coefficient in a vacuum chamber at 1000 Pa and 100°C. $Q_6$ is the amount of heat conducted through the bridging beam. By energy conservation at the $T_s$ node:

$$Q_6 = Q_2 + Q_5 + Q_{10} = \frac{T_h - T_s}{R_s}, \tag{A.11}$$

where $R_s$ is the thermal resistance of the bridging beam:

$$R_s = (\frac{[(1-\phi)k_{sin} + \phi k_l]A_b}{L_s})^{-1}, \tag{A.12}$$

where $\phi = A_{liquid}/A_{solid}$, $L_s$ is the length of the beam, $k_{sin}$ is the thermal conductivity of silicon nitride, $k_l$ is the thermal conductivity of liquid. Here, convection is neglected because conduction is the dominating heat transfer mode in microfluidic

devices.

$Q_5$ is the heat loss due to radiation from the sensing membrane:

$$Q_5 = \sigma_r A_s \epsilon (T_s^4 - T_0^4), \tag{A.13}$$

$Q_{10}$ is the convective heat loss from the sensing membrane:

$$Q_{10} = h_v A_s (T_s - T_0), \tag{A.14}$$

Finally, the beam conductance $G_b$ can be modeled as:

$$G_b = N_b \frac{[(1-\phi)k_{sin} + \phi k_l]A_b}{L_b}, \tag{A.15}$$

where $N_b$ is the number of beams and $L_b$ is the length of the beam. Note that $Q_{loss} = Q_4 + Q_5 + Q_9 + Q_{10}$ and the measurement error can be quantified as:

$$Q_{e,actual} = Q_e \tag{A.16}$$

$$Q_{e,measured} = Q_h - (Q_1 + Q_2) = Q_e + Q_{loss} \tag{A.17}$$

The system error can be found by:

$$Error = |\frac{Q_{e,measured} - Q_{e,actual}}{Q_{e,actual}}|^*100\% \tag{A.18}$$

The result of the modeling is shown in fig.A.3 where the designed channel cross-sectional area is $10^*2$ $\mu m^2$, the ambient pressure is 200 Pa, the beam length is 600 $\mu m$, the bridging beam length is 500 $\mu m$, the pore radius is 50 $nm$, and the number of pores is 10.

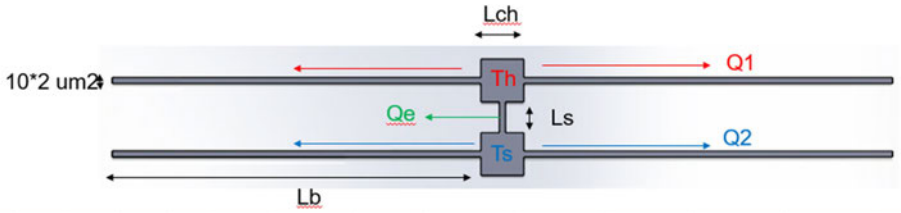


| P0 (Pa) | Lb (um) | Ls (um) | Lch (um) | Pore radius (nm) | # of pores | power (W) | Th (degC) | Ts (degC) | Q1 (W) | Q2 (W) | Qe measured (W) | Qe actual (W) | Error = (Q3m-Q3a)/Q3a*100 % | sum of uncertainties (%) | temperature uncertainty (%) |
|---|---|---|---|---|---|---|---|---|---|---|---|---|---|---|---|
| 200 | 600 | 500 | 60 | 50 | 10 | 9.00E-06 | 28.3015 | 23.1297 | 4.28E-06 | 1.61E-06 | 3.10E-06 | 2.49E-06 | 24.74 | 1.87 | 1.12 |
| | | | | | | 3.60E-05 | 54.2452 | 32.9018 | 1.77E-05 | 6.65E-06 | 1.17E-05 | 9.07E-06 | 28.82 | 0.56 | 0.27 |
| | | | | | | 6.40E-05 | 82.5788 | 43.5585 | 3.23E-05 | 1.22E-05 | 1.96E-05 | 1.46E-05 | 33.77 | 0.36 | 0.15 |
| | | | | | | 1.00E-04 | 120.6625 | 57.8554 | 5.19E-05 | 1.95E-05 | 2.86E-05 | 2.02E-05 | 41.34 | 0.26 | 0.09 |

**Figure A.3:** Result of the thermal network analysis.

The temperature response of the heating membrane ranges between 28 to 120°C when varying the power input from 9 to 100 $\mu W$. Meanwhile, the maximum system error is 41% and I believe that this design can manage to measure a minute heat flux down to 3 $\mu W$ with a relatively low system error. As of now, I have proposed a feasible way to directly measure the heat flux and monitor the pore temperature without thermocouples. The last thing to prove is that the measurement uncertainty is low to prevent huge scattering.

### *A.2.1.1 Measurement uncertainty*

We start by rewriting eq.A.1 to:

$$Q_e = (\bar{Q}_h - Q_{loss}) - (\bar{Q}_1 + \bar{Q}_2) \pm (\delta Q_h + \delta Q_1 + \delta Q_2), \tag{A.19}$$

where the bar indicates the mean value of the physical quantity while $\delta$ indicates the random fluctuation due to noise. Lets find out the relative uncertainty for $\bar{Q}_h$,

$\bar{Q}_1$, and $\bar{Q}_2$. Below I dropped the bar symbol for simplicity.

$$Q_h = Q_m + Q_b = I_{dc}^2 R_{rtd} + I_{dc}^2 R_b, \tag{A.20}$$

where $Q_m$ is the heat generated by the RTD on the heating membrane, $Q_b$ is the heat generated by the wires on the beam. Thus, the relative uncertainty of $Q_h$ can be expressed as:

$$(\frac{\delta Q_h}{Q_h})^2 = (\frac{1}{Q_h}\frac{\partial Q_h}{\partial I_{dc}}\delta I_{dc})^2 + (\frac{1}{Q_h}\frac{\partial Q_h}{\partial R_{rtd}}\delta R_{rtd})^2 + (\frac{1}{Q_h}\frac{\partial Q_h}{\partial R_b}\delta R_b)^2, \tag{A.21}$$

where

$$\frac{\partial Q_h}{\partial I_{dc}} = 2I_{dc}(R_{rtd} + R_b) \tag{A.22}$$

$$\frac{\partial Q_h}{\partial R_{rtd}} = \frac{\partial Q_h}{\partial R_b} = I_{dc}^2 \tag{A.23}$$

Substituting eq.A.22,A.23 back to eq.A.21:

$$(\frac{\delta Q_h}{Q_h})^2 = (\frac{2\delta I_{dc}}{I_{dc}})^2 + (\frac{R_{rtd}}{R_{rtd}+R_b}\frac{\delta R_{rtd}}{R_{rtd}})^2 + (\frac{R_b}{R_{rtd}+R_b}\frac{\delta R_b}{R_b})^2 \tag{A.24}$$

Next, we find:

$$(\frac{2\delta I_{dc}}{I_{dc}})^2 = (\frac{\delta V_{dc}}{V_{dc}})^2 + (\frac{\delta R_{dc}}{R_{dc}})^2 \tag{A.25}$$

A typical lock-in amplifier (SR830) has a built-in voltage uncertainty of 1 mV and $R_0$ is a 10 M$\Omega$ resistance of a 10 ppm/K precision resistor. $\delta R_{dc} = R' - R_0 = R_0(1 + \Delta T(PPM/K) - R_0 = 10^6(1 + 10^{-5} - 1) = 10$. With a typical voltage of 5 V, the dominating uncertainty is the first term in eq.A.25.

Then, we find:

$$(\frac{\delta R_{rtd}}{R_{rtd}})^2 = (\frac{\delta v_j}{V_{rtd}})^2 + (\frac{\delta i}{i_{rtd}})^2, \tag{A.26}$$

where $v_j = 2.5\ nV/\sqrt{Hz}$ @ 1 kHz denotes the Johnson noise. With $V_{rtd} \sim 10mV$, the first term is $79.05 \times 10^{-9}$. $\delta i$ is the noise in the current source $i = v_{out}/R$. Hence,

$$(\frac{\delta i}{i_{rtd}})^2 = (\frac{\delta v_{out}}{v_{out}})^2 + (\frac{\delta R}{R})^2 \tag{A.27}$$

The relative noise in the ac voltage output is about $4 \times 10^{-5}$ Shi et al. (2003) and the resistance fluctuation has been derived above. Thus, $\delta i/i_{rtd} \sim 4 \times 10^{-5}$ and $\delta R_{rtd}/R_{rtd} \sim 4 \times 10^{-5}$. Finally, since the wire on the beam should behave similarly as the RTD on the membrane, we assume $\delta R_b/R_b = \delta R_{rtd}/R_{rtd}$ and we complete our analysis for $Q_h$.

From eq.A.2, the relative uncertainty for $Q_1$ can be written as:

$$(\frac{\partial Q_1}{Q_1})^2 = (\frac{1}{Q_1}\frac{\partial Q_1}{\partial G_b}\delta G_b)^2 + (\frac{1}{Q_1}\frac{\partial Q_1}{\partial \delta \Delta T_h}\delta \Delta T_h)^2 \tag{A.28}$$

with some manipulation,

$$(\frac{\partial Q_1}{Q_1})^2 = (\frac{\delta G_b}{G_b})^2 + (\frac{\delta \Delta T_h}{\Delta T_h})^2 \tag{A.29}$$

From eq.A.5:

$$(\frac{\partial G_b}{G_b})^2 = (\frac{\delta Q_h}{Q_h})^2 + (\frac{\Delta T_h}{\Delta T_h + \Delta T_s}\frac{\delta \Delta T_h}{\Delta T_h})^2 + (\frac{\Delta T_s}{\Delta T_h + \Delta T_s}\frac{\delta \Delta T_s}{\Delta T_s})^2 \tag{A.30}$$

$\delta Q_h/Q_h$ had been derived in eq.A.24. Since the measurement method for both $\Delta T_h$ and $\Delta T_s$ is the same, the relative uncertainty for both measurement should be the same. Thus,

$$(\frac{\delta \Delta T_h}{\Delta T_h})^2 = (\frac{\delta \Delta T_s}{\Delta T_s})^2 = (\frac{NET}{\Delta T_s})^2, \tag{A.31}$$

where $NET$ is the noise-equivalent temperature rise of the membrane and can be expressed as:

$$NET = \frac{NER/R_{rtd}}{TCR}, \tag{A.32}$$

where $NER$ is the noise-equivalent resistance in the $R_{rtd}$ measurement, $TCR$ is the temperature coefficient of resistance $TCR \equiv (dR/dT)/R$. $TCR$ of the RTD is typically $2.7 \times 10^{-3}\ K^{-1}$ at 300 K. $NER/R_{rtd}$ is actually the same as eq.A.26. Finally, by applying the same analogy for $\delta Q_2/Q_2$, we find that it should equal $\delta Q_1/Q_1$, which completed the measurement uncertainty analysis.

The result of the heat flux measurement uncertainty and the temperature measurement uncertainty are also documented in fig.A.3. We can see that as the temperature of the membrane becomes lower, the relative uncertainty becomes larger. This is expected because the relative uncertainty depends inversely as the temperature difference between the membrane and the ambient temperature. A small temperature difference at a lower membrane temperature would lead to a larger relative uncertainty. However, based on this analysis, the maximum relative uncertainty is about 2% and I believe this measurement method could solve the scattering issue due to temperature fluctuation.

### A.2.2 Fabrication

Fig.A.4 documents the designed fabrication process to make the device. We start with a (100) silicon wafer and etch down with RIE. Then, we can deposit a layer of conformal LPCVD low stress silicon nitride on top of the silicon substrate to form the bottom part of the microchannel. The next step is to deposit a layer of poly-silicon as a sacrificial layer and lift off to remove excess material. A chemical-mechanical planarization step is needed to flatten the poly-silicon layer with the

sin layer. Another LPCVD low stress sin is deposited to form the upper part of the microchannel. Gold wire is patterned by using lift-off lithography and e-beam deposition. Next, we etch away some sin to open a hole to expose the poly-silicon layer and to etch into the silicon substrate by using KOH. Finally, FIB will be used to drill the pore.

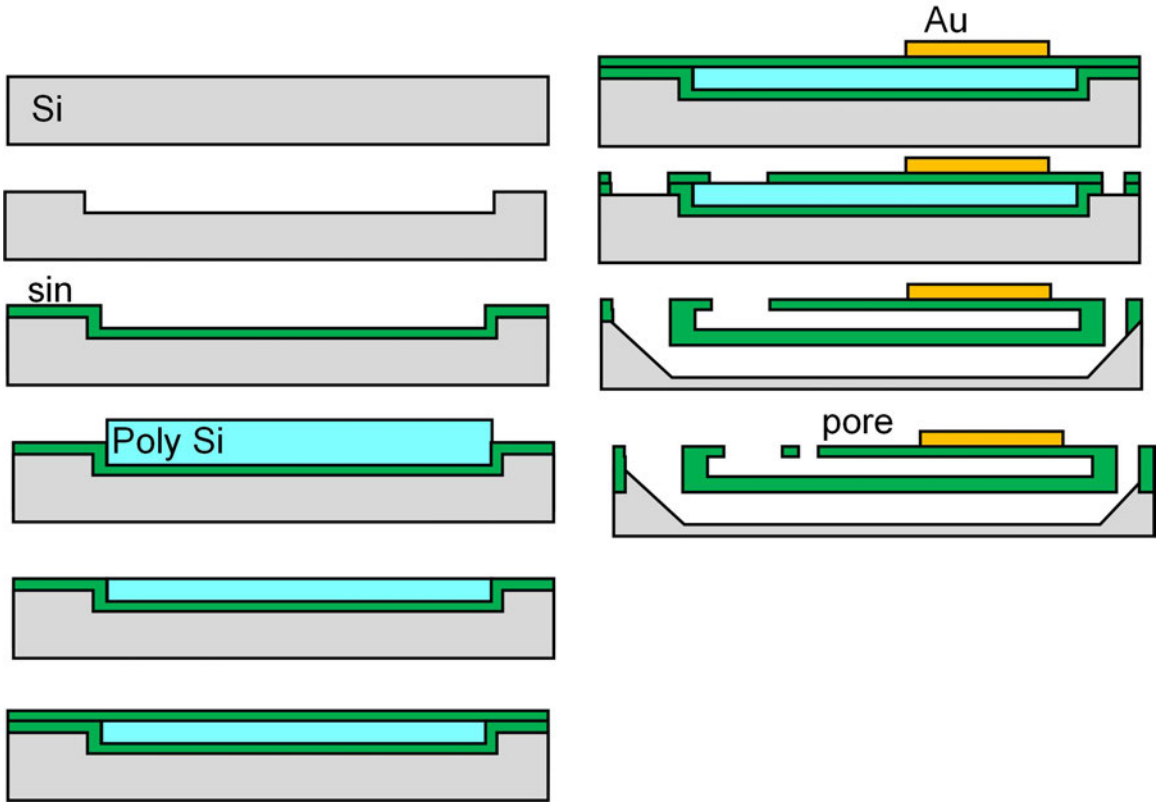


**Figure A.4:** Designed fabrication process for the device. Read from left to right, top to down.

## BIBLIOGRAPHY

Adera, S., Antao, D., Raj, R., & Wang, E. N. (2016). Design of micropillar wicks for thin-film evaporation. *International Journal of Heat and Mass Transfer*, *101*, 280–294.

Adera, S., Raj, R., & Wang, E. N. (2013). Capillary-limited evaporation from well-defined microstructured surfaces. In *International Conference on Micro/Nanoscale Heat Transfer*, vol. 36154, (p. V001T11A006). American Society of Mechanical Engineers.

Aly, N. H., & El-Figi, A. K. (2003). Mechanical vapor compression desalination systemsa case study. *Desalination*, *158*(1-3), 143–150.

Bagnall, K. R. (2013). *Device-level thermal analysis of GaN-based electronics*. Ph.D. thesis, Massachusetts Institute of Technology.

Behrens, S. H., & Grier, D. G. (2001). The charge of glass and silica surfaces. *The Journal of Chemical Physics*, *115*(14), 6716–6721.

Belyaeva, L. A., & Schneider, G. F. (2020). Wettability of graphene. *Surface Science Reports*, *75*(2), 100482.

Buffone, C., & Sefiane, K. (2004). Investigation of thermocapillary convective patterns and their role in the enhancement of evaporation from pores. *International Journal of Multiphase Flow*, *30*(9), 1071–1091.

Buffone, C., Sefiane, K., & Christy, J. (2004). Experimental investigation of the hydrodynamics and stability of an evaporating wetting film placed in a temperature gradient. *Applied thermal engineering*, *24*(8-9), 1157–1170.

Bulut, M., Kandlikar, S. G., & Sozbir, N. (2019). A review of vapor chambers. *Heat Transfer Engineering*, *40*(19), 1551–1573.

Carey, V. P. (2020). *Liquid-vapor phase-change phenomena: an introduction to the thermophysics of vaporization and condensation processes in heat transfer equipment*. CRC Press.

Chen, C., Kuang, Y., & Hu, L. (2019). Challenges and opportunities for solar evaporation. *Joule*, *3*(3), 683–718.

Chen, J., & Li, L. (2020). Effect of oxidation degree on the thermal properties of graphene oxide. *Journal of Materials Research and Technology*, *9*(6), 13740–13748.

Dai, X., Yang, F., Yang, R., Lee, Y.-C., & Li, C. (2013). Micromembrane-enhanced capillary evaporation. *International Journal of Heat and Mass Transfer*, *64*, 1101–1108.

DasGupta, S., Schonberg, J., & Wayner Jr, P. (1993). Investigation of an evaporating extended meniscus based on the augmented young–laplace equation. *Journal of Heat Transfer*, *115*(1), 201–208.

Derjaguin, B., & Churaev, N. (1974). Structural component of disjoining pressure. *Journal of Colloid and Interface Science*, *49*(2), 249–255.

Deshmukh, A., Boo, C., Karanikola, V., Lin, S., Straub, A. P., Tong, T., Warsinger, D. M., & Elimelech, M. (2018). Membrane distillation at the water-energy nexus: limits, opportunities, and challenges. *Energy & Environmental Science*, *11*(5), 1177–1196.

Dongare, P. D., Alabastri, A., Neumann, O., Nordlander, P., & Halas, N. J. (2019). Solar thermal desalination as a nonlinear optical process. *Proceedings of the National Academy of Sciences*, *116*(27), 13182–13187.

Dongare, P. D., Alabastri, A., Pedersen, S., Zodrow, K. R., Hogan, N. J., Neumann, O., Wu, J., Wang, T., Deshmukh, A., Elimelech, M., et al. (2017). Nanophotonics-enabled solar membrane distillation for off-grid water purification. *Proceedings of the National Academy of Sciences*, *114*(27), 6936–6941.

Dudchenko, A. V., Chen, C., Cardenas, A., Rolf, J., & Jassby, D. (2017). Frequency-dependent stability of cnt joule heaters in ionizable media and desalination processes. *Nature nanotechnology*, *12*(6), 557–563.

Dwivedi, R., & Singh, P. K. (2022). Thin film evaporation: New insights with nanofluid inclusion and component of the electrostatic interactions. *Physics of Fluids*, *34*(10).

Eijkel, J. C., Dan, B., Reemeijer, H., Hermes, D., Bomer, J. G., & van den Berg, A. (2005). Strongly accelerated and humidity-independent drying of nanochannels induced by sharp corners. *Physical review letters*, *95*(25), 256107.

Gennes, P. d., et al. (1985). Wetting: statics and dynamics. *Review of Modern Physics*, *57*(3), 827–863.

Ghasemi, H., Ni, G., Marconnet, A. M., Loomis, J., Yerci, S., Miljkovic, N., & Chen, G. (2014). Solar steam generation by heat localization. *Nature communications*, *5*, 4449.

Hanks, D. F., Lu, Z., Sircar, J., Kinefuchi, I., Bagnall, K. R., Salamon, T. R., Antao, D. S., Barabadi, B., & Wang, E. N. (2020). High heat flux evaporation of low surface tension liquids from nanoporous membranes. *ACS applied materials & interfaces*, *12*(6), 7232–7238.

Hanks, D. F., Lu, Z., Sircar, J., Salamon, T. R., Antao, D. S., Bagnall, K. R., Barabadi, B., & Wang, E. N. (2018). Nanoporous membrane device for ultra high heat flux thermal management. *Microsystems & nanoengineering*, *4*(1), 1–10.

Himanshu, M. (2013). *Proton Transfers at the Air-Water Interface*. Ph.D. thesis, California Institute of Technology.

Israelachvili, J. N. (2011). *Intermolecular and surface forces*. Academic press.

John, B., Gibelli, L., Enright, R., Sprittles, J. E., Lockerby, D. A., & Emerson, D. R. (2021). Evaporation from arbitrary nanoporous membrane configurations: An effective evaporation coefficient approach. *Physics of Fluids*, *33*(3), 032022.

Khayet, M. (2011). Membranes and theoretical modeling of membrane distillation: A review. *Advances in colloid and interface science*, *164*(1-2), 56–88.

Langmuir, I. (1938). Repulsive forces between charged surfaces in water, and the cause of the jones-ray effect. *Science*, *88*(2288), 430–432.

Lee, J., & Karnik, R. (2010). Desalination of water by vapor-phase transport through hydrophobic nanopores. *Journal of Applied Physics*, *108*(4), 044315.

Lee, J., Laoui, T., & Karnik, R. (2014). Nanofluidic transport governed by the liquid/vapour interface. *Nature nanotechnology*, *9*(4), 317–323.

Lee, W.-C., Ronghe, A., Villalobos, L. F., Huang, S., Dakhchoune, M., Mensi, M., Hsu, K.-J., Ayappa, K. G., & Agrawal, K. V. (2022). Enhanced water evaporation from å-scale graphene nanopores. *ACS nano*, *16*(9), 15382–15396.

Li, Y., Alibakhshi, M. A., Zhao, Y., & Duan, C. (2017). Exploring ultimate water capillary evaporation in nanoscale conduits. *Nano Letters*, *17*(8), 4813–4819.

Li, Y., Chen, H., Xiao, S., Alibakhshi, M. A., Lo, C.-W., Lu, M.-C., & Duan, C. (2019). Ultrafast diameter-dependent water evaporation from nanopores. *ACS nano*, *13*(3), 3363–3372.

Liu, K.-K., Jiang, Q., Tadepalli, S., Raliya, R., Biswas, P., Naik, R. R., & Singamaneni, S. (2017). Wood–graphene oxide composite for highly efficient solar steam generation and desalination. *ACS applied materials & interfaces*, *9*(8), 7675–7681.

Liu, Y., Xu, H., Dai, W., Li, H., & Wang, W. (2018). 2.5-dimensional parylene c micropore array with a large area and a high porosity for high-throughput particle and cell separation. *Microsystems & nanoengineering*, *4*(1), 1–12.

Lu, Q., Shi, W., Yang, H., & Wang, X. (2020). Nanoconfined water-molecule channels for high-yield solar vapor generation under weaker sunlight. *Advanced Materials*, *32*(42), 2001544.

Lu, Z., Kinefuchi, I., Wilke, K. L., Vaartstra, G., & Wang, E. N. (2019). A unified relationship for evaporation kinetics at low mach numbers. *Nature communications*, *10*(1), 1–8.

Lu, Z., Narayanan, S., & Wang, E. N. (2015). Modeling of evaporation from nanopores with nonequilibrium and nonlocal effects. *Langmuir*, *31*(36), 9817–9824.

Lu, Z., Salamon, T. R., Narayanan, S., Bagnall, K. R., Hanks, D. F., Antao, D. S., Barabadi, B., Sircar, J., Simon, M. E., & Wang, E. N. (2016). Design and modeling of membrane-based evaporative cooling devices for thermal management of high heat fluxes. *IEEE transactions on components, packaging and manufacturing technology*, *6*(7), 1056–1065.

Lu, Z., Wilke, K. L., Preston, D. J., Kinefuchi, I., Chang-Davidson, E., & Wang, E. N. (2017). An ultrathin nanoporous membrane evaporator. *Nano letters*, *17*(10), 6217–6220.

Narayanan, S., Fedorov, A. G., & Joshi, Y. K. (2011). Interfacial transport of evaporating water confined in nanopores. *Langmuir*, *27*(17), 10666–10676.

Narayanan, S., Fedorov, A. G., & Joshi, Y. K. (2013). Heat and mass transfer during evaporation of thin liquid films confined by nanoporous membranes subjected to air jet impingement. *International Journal of Heat and Mass Transfer*, *58*(1-2), 300–311.

Nayar, K. G., Sharqawy, M. H., Banchik, L. D., et al. (2016). Thermophysical properties of seawater: A review and new correlations that include pressure dependence. *Desalination*, *390*, 1–24.

Pálinkás, G., Bopp, P., Jancsó, G., & Heinzinger, K. (1984). The effect of pressure on the hydrogen bond structure of liquid water. *Zeitschrift fuer Naturforschung A*, *39*(2), 179–185.

Pati, S., Som, S., & Chakraborty, S. (2013). Combined influences of electrostatic component of disjoining pressure and interfacial slip on thin film evaporation in nanopores. *International Journal of Heat and Mass Transfer*, *64*, 304–312.

Philip, J. (1977). Unitary approach to capillary condensation and adsorption. *The Journal of Chemical Physics*, *66*(11), 5069–5075.

Poli, E., Jong, K. H., & Hassanali, A. (2020). Charge transfer as a ubiquitous mechanism in determining the negative charge at hydrophobic interfaces. *Nature communications*, *11*(1), 1–13.

Politano, A., Di Profio, G., Fontananova, E., Sanna, V., Cupolillo, A., & Curcio, E. (2019). Overcoming temperature polarization in membrane distillation by thermoplasmonic effects activated by ag nanofillers in polymeric membranes. *Desalination*, *451*, 192–199.

Prydatko, A. V., Belyaeva, L. A., Jiang, L., Lima, L., & Schneider, G. F. (2018). Contact angle measurement of free-standing square-millimeter single-layer graphene. *Nature communications*, *9*(1), 1–7.

R Core Team (2017). R: A Language and Environment for Statistical Computing. https://www.r-project.org/.

Rana, B., Fairhurst, D. J., & Jena, K. C. (2022). Investigation of water evaporation process at air/water interface using hofmeister ions. *Journal of the American Chemical Society*, *144*(39), 17832–17840.

Schrage, R. W. (1953). *A theoretical study of interphase mass transfer*. Columbia University Press.

Seyfi, A., Afzalzadeh, R., & Hajnorouzi, A. (2017). Increase in water evaporation rate with increase in static magnetic field perpendicular to water-air interface. *Chemical Engineering and Processing-Process Intensification*, *120*, 195–200.

Shafieian, A., & Khiadani, M. (2019). A novel solar-driven direct contact membrane-based water desalination system. *Energy Conversion and Management*, *199*, 112055.

Sharpsteen, C., & Bracken, C. (2016). *tikzDevice: R Graphics Output in LaTeX Format*. https://cran.r-project.org/package=tikzDevice.

Shi, L., Li, D., Yu, C., Jang, W., Kim, D., Yao, Z., Kim, P., & Majumdar, A. (2003). Measuring thermal and thermoelectric properties of one-dimensional nanostructures using a microfabricated device. *Journal of Heat Transfer*, *125*(5), 881–888.

Sievert, C., Parmer, C., Hocking, T., Chamberlain, S., Ram, K., Corvellec, M., & Despouy, P. (2017). *plotly: Create Interactive Web Graphics via 'plotly.js'*. https://cran.r-project.org/package=plotly.

Somasundaram, S., Zhu, Y., Lu, Z., Adera, S., Bin, H., Mengyao, W., Tan, C. S., & Wang, E. N. (2018). Thermal design optimization of evaporator micropillar wicks. *International Journal of Thermal Sciences*, *134*, 179–187.

Straub, A. P., Bergsman, D. S., Getachew, B. A., Leahy, L. M., Patil, J. J., Ferralis, N., & Grossman, J. C. (2021). Highly conductive and permeable nanocomposite ultrafiltration membranes using laser-reduced graphene oxide. *Nano Letters*, *21*(6), 2429–2435.

Swanson, L., & Herdt, G. (1992). Model of the evaporating meniscus in a capillary tube. *Journal of Heat Transfer*, *114*(2), 434–441.

Tang, J., Zheng, T., Song, Z., Shao, Y., Li, N., Jia, K., Tian, Y., Song, Q., Liu, H., & Xue, G. (2020). Realization of low latent heat of a solar evaporator via regulating the water state in wood channels. *ACS applied materials & interfaces*, *12*(16), 18504–18511.

Tao, P., Ni, G., Song, C., Shang, W., Wu, J., Zhu, J., Chen, G., & Deng, T. (2018). Solar-driven interfacial evaporation. *Nature energy*, *3*(12), 1031–1041.

University of Florida (2000). Useful Pharmacokinetic Equations. http://pharmacy.ufl.edu/files/2013/01/5127-28-equations.pdf (Accessed:2017-01-25).

Wan, C. F., & Chung, T.-S. (2018). Techno-economic evaluation of various ro+ pro and ro+ fo integrated processes. *Applied energy*, *212*, 1038–1050.

Wang, H., Murthy, J. Y., & Garimella, S. V. (2008). Transport from a volatile meniscus inside an open microtube. *International Journal of Heat and Mass Transfer*, *51*(11-12), 3007–3017.

Wayner Jr, P. (1979). Effect of thin film heat transfer on meniscus profile and capillary pressure. *AIAA Journal*, *17*(7), 772–776.

Wayner Jr, P., Kao, Y., & LaCroix, L. (1976). The interline heat-transfer coefficient of an evaporating wetting film. *International Journal of Heat and Mass Transfer*, *19*(5), 487–492.

Wee, S.-K., Kihm, K. D., & Hallinan, K. P. (2005). Effects of the liquid polarity and the wall slip on the heat and mass transport characteristics of the micro-scale evaporating transition film. *International journal of heat and mass transfer*, *48*(2), 265–278.

Wickham, H. (2007). Reshaping data with the reshape package. *J Stat Softw*, *21*(12).

Wilke, K. L., Barabadi, B., Zhang, T., & Wang, E. N. (2016). Controlled wetting in nanoporous membranes for thin film evaporation. *Journal of Heat Transfer*, *138*(8).

Xiao, S., Meng, K., Xie, Q., Zhai, L., Xu, Z., Wang, H., & Duan, C. (2022). Edge-enhanced ultrafast water evaporation from graphene nanopores. *Cell Reports Physical Science*, (p. 100900).

Xue, G., Xu, Y., Ding, T., Li, J., Yin, J., Fei, W., Cao, Y., Yu, J., Yuan, L., Gong, L., et al. (2017). Water-evaporation-induced electricity with nanostructured carbon materials. *Nature nanotechnology*, *12*(4), 317–321.

Yaroshchuk, A. (2022). Evaporation-driven electrokinetic energy conversion: Critical review, parametric analysis and perspectives. *Advances in Colloid and Interface Science*, (p. 102708).

Zhou, S., Xiong, Z., Liu, F., Lin, H., Wang, J., Li, T., Han, Q., & Fang, Q. (2019). Novel janus membrane with unprecedented osmosis transport performance. *Journal of Materials Chemistry A*, *7*(2), 632–638.

Zou, A., Poudel, S., Gupta, M., & Maroo, S. C. (2021). Disjoining pressure of water in nanochannels. *Nano letters*, *21*(18), 7769–7774.

Zuo, K., Wang, W., Deshmukh, A., Jia, S., Guo, H., Xin, R., Elimelech, M., Ajayan, P. M., Lou, J., & Li, Q. (2020). Multifunctional nanocoated membranes for high-rate electrothermal desalination of hypersaline waters. *Nature Nanotechnology*, *15*(12), 1025–1032.

**CURRICULUM VITAE**